Nonlinear Dynamic Model and Simulation of a High Pressure Monotube Shock Absorber Using the Bond Graph Method

by

Rosario Mollica

M.S., Engineering
University of Michigan, 1986

B.S., Mechanical Engineering
Worcester Polytechnic Institute, 1985

Submitted to the Department of Mechanical Engineering

in Partial Fulfillment of the Requirements for the degree of

Master of Science in Mechanical Engineering

at the

Massachusetts Institute of Technology

February 1997

Signature of Author _____

Department of Mechanical Engineering
February 5, 1997

Certified by _____

Dr. Kamal Youcef-Toumi
Associate Professor
Thesis Supervisor

Accepted by _____

Dr. Ain A. Sonin
Chairman, Department Committee on Graduate Students

Nonlinear Dynamic Model and Simulation of a High Pressure Monotube Shock Absorber Using the Bond Graph Method

by

Rosario Mollica

Submitted to the Department of Mechanical Engineering
on January 17, 1997 in Partial Fulfillment of the
Requirements for the Degree of Master of Science in
Mechanical Engineering

Abstract

A physics-based model for a high pressure monotube shock absorber is proposed by which the nonlinear dynamic behavior of these dampers can be analyzed. The bond graph technique is used to model these shock absorbers accurately over a wide range of stroking frequencies and to identify the interaction between mechanical, fluid, and thermodynamic elements. Various phenomena are modelled such as fluid inertia effects, laminar orifice flow, air entrained in the hydraulic fluid, and cavitation.

Simulation results demonstrate good model accuracy when compared to test data for similar hydraulic dampers. Parametric studies involving various elements of the system including gas pressurization, the amount of entrained air, and stiction are conducted in order to demonstrate the affects of these parameters on system performance. Results indicate the fundamental characteristics of shock absorbers are produced by the interaction of resistive and capacitive elements inherent in these systems.

Capacitive elements combine with resistive elements resulting in hysteresis in the force-velocity characteristic and less energy dissipation at higher frequencies for constant maximum stroking velocities. The effects of fluid inertia and laminar flow are found to be negligible for the range of frequencies investigated (1 to 20Hz) in the monotube design of this study. Modifications to the model are proposed to reduce the state order for use in automotive suspension system models.

Thesis Supervisor: Dr. Kamal Youcef-Toumi

Title: Associate Professor of Mechanical Engineering

Acknowledgements

I would like to express my thanks to the many people who have supported me while I obtained my degree. First I wish to thank my advisor, Professor Kamal Youcef-Toumi, for his insightful counsel, suggestions, and aid in writing this thesis. My thanks to my management at GE Aircraft Engines for their support -including Ted Oldakowski, Sheldon Carpenter, Dan Gilmore, and Anne Schwartz. I am grateful to Monroe Automotive, expecially the late Dave MacLennan, for a variety of information regarding automotive shock absorbers. Most of all, my thanks to my wife, Ann C. Mollica, for her engineering advise, encouragement, and patience over the last several years.

Contents

List of Figures

List of Tables

Nomenclature

A = area

Ac = fluid acceleration number

A_c = area of vena contracta

A_d = blow-off valve effective area

A_{fp} = floating piston area

A_{gx} = annulus area between piston and tube

A_h = piston area on the headside

A_o = orifice area

A_r = piston area on the rodside

A_{rod} = piston rod area

A_{wp} = piston area contacting fluid in gap between piston and tube

a = acceleration

C = bond graph generalized compliance

C_{aa} = blow-off valve compliance at/due to seat constraint

C_{ao} = blow-off valve compliance at gap due to hydraulic load

C_{bo} = effective blow-off valve compliance for open valve

C_{bc} = effective blow-off valve compliance for closed valve

C_c = contraction coefficient

C_{cs} = coil spring compliance

C_d = discharge coefficient or effective compliance of blow-off valve disk

C_h = headside compliance fluid capacitor

C_{oa} = blow-off valve compliance at hydraulic load application due to seat constraint

C_{oo} = blow-off valve compliance at/due to hydraulic load

C_p = specific heat at constant pressure

C_r = rodside fluid capacitor compliance

C_s = automotive suspension compliance

C_v = specific heat at constant volume

C_{vg} = nitrogen gas specific heat at constant volume

c = isothermal compressibility

D_{hb} = blow-off restriction hydraulic diameter

D_{hk} = bleed restriction hydraulic diameter

D_{hp} = port restriction hydraulic diameter

D_i = tube inside diameter

D_o = tube outside diameter

E = Young's modulus

E_g = internal energy of nitrogen gas

e = Euler's number

F_a = blow-off valve seat constraint force

F_{csp} = coil spring preload

F_E = force of bond graph effort source

F_f = friction force

F_{ffp} = friction force acting on floating piston

F_{gx} = force due to pressure gradient in gap between piston and tube

F_o = hydraulic force required to open blow-off valve

F_{obo} = effective force imposed by blow-off valve

F_P = net pressure force acting on floating piston

$F_{\tau p}$ = fluid shear force acting on piston

$F_{\tau t}$ = fluid shear force acting on tube

f = coefficient of friction

f_d = dynamic coefficient of friction

f_{fp} = coefficient of friction between floating piston seal and tube

f_o = static coefficient of friction

g_p = gap between piston and tube

h = specific enthalpy

I = bond graph generalized inertia

I_{sc} = compression port restriction fluid inertia

I_{sr} = rebound port restriction fluid inertia

K = static pressure loss coefficient

K_o = orifice static pressure loss coefficient

L = length

L_p = piston length

l = length along piston

m = mass

$\dot{m}$ = mass flow

m_{fp} = floating piston mass

m_g = nitrogen gas mass

m_p = piston mass (may include portion of automobile)

N = normal force

N_{pc} = number of compression port restrictions

N_{pr} = number of rebound port restrictions

P = pressure

P_{ao} = pressure of air at some initial condition

P_{atm} = atmospheric pressure

P_{bo} = blow-off valve preload pressure

P_g = pressure of nitrogen gas

P_h = headside capacitor pressure

P_I = pressure loss due to fluid inertia

P_{kc} = pressure loss across compression bleed restriction

P_{kr} = pressure loss across rebound bleed restriction

P_o = pressure at linearized condition or across blow-off orifice

P_R = pressure loss due to fluid resistance

P_r = rodside capacitor pressure

P_{setc} = compression check value pressure preload

P_{setr} = rebound check value pressure preload

P_{sic} = pressure drop across compression port restriction

P_{sir} = pressure drop across rebound port restriction

P_t^{norm} = normalized transistional pressure loss across restriction

P_v = hydraulic fluid vapor pressure

p = fluid momentum

Q = flow

$\dot{Q}$ = flow acceleration

Q_b = blow-off restriction flow

Q_{gp} = leakage flow due to the pressure across the piston

Q_{gx} = leakage flow due to the piston shearing motion

Q_h = flow into headside fluid capacitor due to compressibility

Q_{hp} = equivalent headside flow due to the piston motion

Q_{kc} = compression bleed restriction flow

Q_{kr} = rebound bleed restriction flow

Q_{pc} = compression port restriction flow

Q_{pk} = total leakage flow between piston and tube

Q_{pr} = rebound port restriction flow

Q_r = flow into rodside fluid capacitor due to compressibility

Q_{rp} = equivalent rodside flow due to piston motion

Q_{rt} = equivalent rodside flow due to tube motion

R = bond graph generalized resistance

R_b = resistance of blow-off restriction

Re = Reynolds number

Re_t = laminar-to-turbulent transitional Reynolds number

Re_x = length Reynolds number

R_g = gas constant

R_{gp} = resistance of fluid in gap between piston and tube in shear

R_{gx} = shear resistance of fluid in gap between piston and tube

R_{kc} = compression bleed restriction resistance

R_{kr} = rebound bleed restriction resistance

R_{pc} = compression port restriction resistance

R_{pr} = rebound port restriction resistance

S = entropy

S_E = generalized bond graph effort source

S_F = generalized bond graph flow source

T = temperature

T_g = nitrogen gas temperature

T_o = temperature at linearized condition

t = time

U = flow velocity

V = volume

$\dot{V}$ = equivalent flow due to volume change

$\overline{V}$ = mean fluid velocity

V_a = volume of air

V_{ao} = volume of air at some initial condition

V_c = pressurized cylinder volume

V_d = volume of fluid upstream of blow-off valve

V_g = nitrogen gas volume

V_h = headside volume of fluid

V_l = liquid hydraulic fluid volume

V_p = piston swept volume

V_r = rodside volume of fluid

v = velocity or specific volume

v_{fp} = floating piston velocity relative to tube

W = weight

W_{fp} = floating piston weight

W_p = piston weight (may include portion of automobile)

x = displacement or length

x_p = piston displacement

$\dot{x}_p$ = piston velocity

$x_{p/t}$ = piston displacement relative to tube

x_t = tube displacement

$\dot{x}_t$ = tube velocity

y = radial dimension across gap from piston to tube

y_a = blow-off valve displacement independent of seat constraint

y_{ap} = blow-off valve preload gap

y_b = blow-off valve gap

y_o = blow-off valve deflection under hydraulic load

z = displacement relative to reference datum

α = volume expansivity (cubical expansion coefficient)

α' = kinetic energy correction factor at cross section

α'' = momentum correction at cross section

β = bulk modulus

β_a = bulk modulus of air

β_c = pressurized container effective bulk modulus

β_{isen} = isentropic bulk modulus

δ = laminar flow coefficient

$\gamma \equiv \frac{C_p}{C_v}$, ratio of specific heats

ν = Poisson's ratio

ρ = fluid density

ρ_o = fluid density at linearized condition

τ = fluid shear stress

Chapter 1
Introduction

1.1 Motivation

An automotive monotube shock absorber, unlike a linear dashpot model, generates a force which is not simply a function of the velocity of its ends. Accurate physics-based models of shock absorbers are important to simulations of existing systems. These models also have a role in predicting behavior during the design phase of a system.

Past researchers have developed models to simulate the nonlinear and hysteretic behavior of shock absorbers. Most of these models were intended to be part of larger automotive simulations. For example, Karadayi and Masada [8] used describing function techniques to reduce the order of complexity and relied on the shock absorber behavior to be known a priori. Reybrouck [20] developed a parametric model for single tube (monotube) shock absorber in which the parameters were derived from physical concepts and calculated using test results.

The most often cited physics-based model is that of Lang [15] and Segal and Lang [22]. These researchers developed a nonlinear higher order physics-based model to simulate low pressure twin tube shock absorbers at high stroking frequencies. Segal and Lang concluded the nonlinear effects were the result the compressibility of the fluid, the elasticity of the absorber tube, and the formation and collapse of either a gas or vapor phase in the hydraulic fluid.

This thesis proposes a nonlinear higher order model of a monotube shock absorber used in high performance automobiles. The bond graph analysis technique is used to

develop dynamic modeling criteria. These criteria determine the physical elements required for accurate dynamic modeling of these damper systems at high frequencies. Laminar, as well as turbulent flow in the cross piston channels will be modeled, expanding on the work of Segal and Lang for low velocity accuracy. More complex friction and cavitation models and their effect on hysteresis will be examined. Results will be compared to test data to determine model acceptability as a design tool.

1.2 System Description

A typical high pressure monotube shock absorber is shown in Figure 1.1. The base of the shock tube attaches to the automobile wheel suspension or axle (unsprung mass) and the top end composed of the rod and piston attaches to the frame (sprung mass). The side of the piston attached to the rod is referred to as the "rod side volume" or "rebound volume" and the side with the larger area is the "head side volume" or "compression volume." Oil occupies the tube volume on either side of the piston. A high pressure monotube has a "floating piston" within the tube volume across from the head side of the piston. The floating piston separates the oil from a volume of nitrogen gas under high pressure (approximately 20 bar). The floating piston is intended to positively separate the nitrogen gas from the oil. Consequently, the shock absorber can be mounted "upside down" in order to reduce the unsprung mass.

When the shock is compressed during the compression (or "jounce") stroke, the hydraulic fluid from the head side volume is forced through an arrangement of valves and orifices across the piston and into the rodside volume. First the oil enters any of several port restrictions when pressure differential across a check valve exceeds a set value. The fluid then enters a small junction volume within the piston before passing to the other side of the piston through a set of orifices referred to as the bleed (or

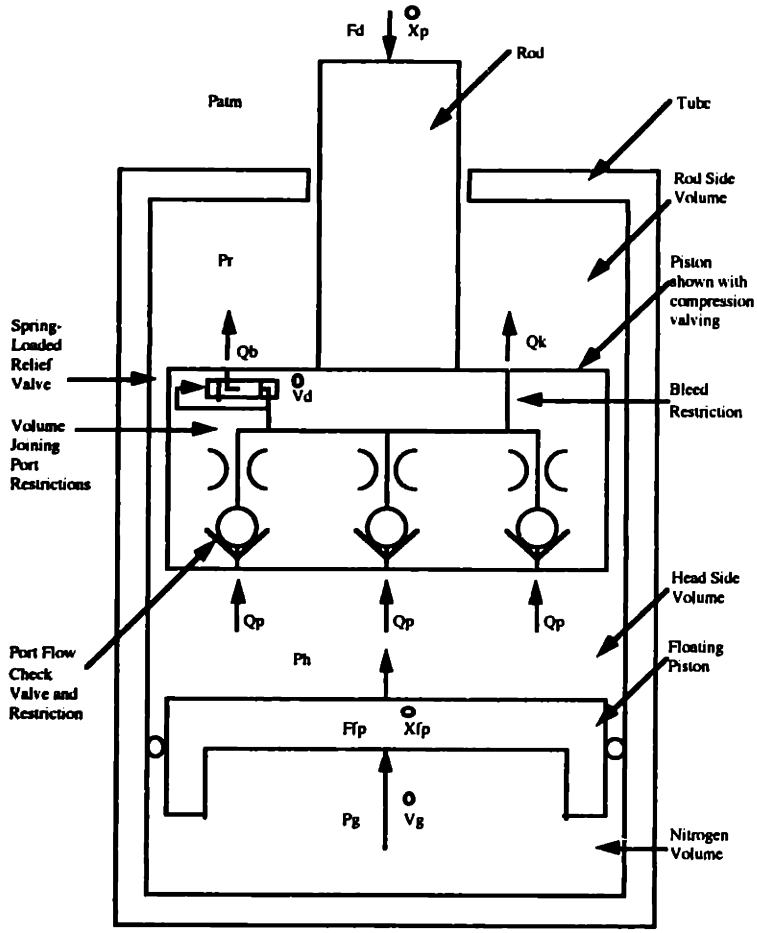

Figure 1.1: Monotube shock absorber (shown with compression valving only)

leak) restrictions. A second conduit opens from the junction volume to the other side of the piston via a pressure relief (or "blow-off") valve when the pressure differential exceeds a preset value. Oil will also leak around the gap between the piston seal and the tube inner diameter. The relative incompressibility of oil and the fact that the displaced volume on the head side is larger than that of the rod side results in a reduction in the volume of nitrogen gas to account for the additional volume of fluid on the head side which could not be forced to the rod side. When the shock extends, the rebound stroke takes place. The fluid on the rod side increases in pressure relative to the head side and oil flows across the piston to the head side through a separate set of ports and orifices (not shown in Figure 1.1) than those active on the compression

stroke. The compression ports are closed-off by a system of check valves during the rebound stroke and vice versa. As opposed to the compression stroke, however, the nitrogen gas volume returns a compensating "flow."

1.3 Thesis Overview

A model of a monotube shock absorber is developed in the following chapters from the bond graph technique, simulated using the MATLAB program to integrate the nonlinear state equations, and compared to test data from an actual system. Conclusions are drawn regarding the accuracy of the model simulation, the dynamics of automotive shock absorbers, in general, and the role of physics-based models in the design synthesis process.

Chapter 2
Model Development

2.1 Introduction

This chapter discusses the modelling of each element of a monotube shock absorber in detail. The overall interaction of the components is outlined in order to identify the elements which provide the system with states. The model is developed from the bond graph technique employing the physical principles describing the dynamics of the state elements. Finally, the elements are integrated to develop the force output relationship based on the system states and input velocity for the shock absorber model in either a laboratory test configuration or as part of an automobile suspension system.

2.2 Model Overview

The displacement of the tube base and the forward motion of the automobile produce an input velocity to the shock absorber. The fluid compresses resulting in the storage of potential energy that converts to heat as fluid pressure is lost by viscous turbulence when the fluid flows through the piston ports and orifices. The output of the shock absorber is the force generated by the relative motion of the shock absorber ends.

A static analysis for a constant stroke speed will result in a good approximation of the output force if one assumes turbulent flow and that the entire pressure differential across the piston occurs across the bleed orifices and the relief valve. A single nonlinear equation, where the only unknown is the pressure difference across the restrictions,

results from flow continuity and the orifice flow equation. However, modelling the nonlinear characteristics of actual shock absorbers as simulated in the figures of Sect. 3.2, requires more detailed modelling which considers the energy storage elements of the shock.

2.3 Bond Graph Model

Analysis of the high pressure monotube shock absorber system has produced an 8 state model capable of dynamic simulation of monotube shock absorbers. The model includes all of the elements required to characterize the dynamic behavior of these shock absorber systems. The fluid volumes, the valve springs, and the gas reservoir are the kinetic energy storage devices which in terms of bond graph notation are known as generalized capacitors. The masses of the piston, floating piston, and tube, as well as the fluidic inertias of the cross piston flow, are the potential energy storage devices. The ports and orifices in and around the piston and the interfaces between rubbing surfaces are the resistors which dissipate energy during motion. The cross piston and leakage flows are calculated based on Reynolds number dependent loss coefficients in order to consider laminar, as well as turbulent, flow regimes. The resulting state equations integrate the fluid, mechanical, and thermodynamic elements required to produce the nonlinear behavior characterized by frequency dependent hysteresis loops when observed on the force-velocity plane or force-displacement plane. The bond graph model described below identifies how the elements interact to produce this nonlinear behavior. Figure 2.1 is a word bond graph model where each of the major elements of the model are represented. More detailed models of the individual components are given in the sections which follow.

(i) Shock Tube:

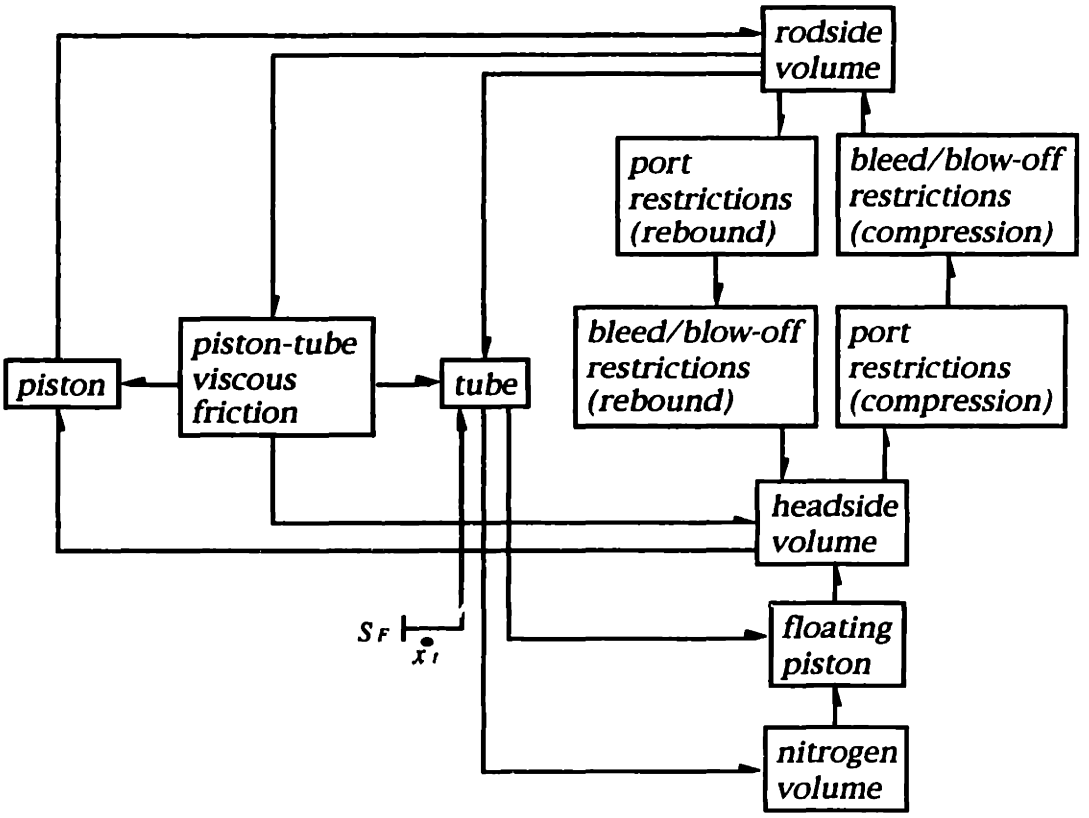

Figure 2.1: Monotube shock absorber word bond graph model

The ground displacement in combination with the forward velocity of the automobile results in a single flow source to the system. The weight of tube, the inertia of the tube and wheel (assuming negligible compliance and damping of the wheel), the difference of the forces resulting from the pressure on the rod and headside chambers, and the frictional load from the piston and floating piston all impose efforts.

(ii) Piston-Tube Friction:

The relative motion between the tube and piston produces friction. The resulting resistance element is in resistive causality because the tube and piston bonds impose flow.

(iii) Piston:

The car suspension compliance, the weight of the piston and portion of the automobile, and the forces on either side of the piston due to fluid pressure apply the efforts on the piston. The mass of the piston and a portion of the automobile creates an inertia element which defines the flow.

(iv) Nitrogen Gas, Rod, and Headside Volumes:

The nitrogen gas volume, as well as the volumes of fluid on either side of the piston produce states of the problem if one considers (1) the compliance of the fluid (including the tube mechanical compliance and that of any trapped air) and (2) the capacitance of the thermodynamic accumulator defined by the gas volume below the floating piston. The inertia of the floating piston is also allowed to produce a state of the system.

(iv) Piston Flow Passages:

Fluid flow between the rod and headside volumes passes through the port, bleed, and blow-off restrictions within the piston. The inertia of the fluid in the port restriction and the blow-off valve compliances also produce states of the system.

2.4 Fluidic Capacitor States

The fluid volume within the shock absorber cylinder on either side of the piston is compressible to some extent under stress. The loads of the piston are sufficient under normal operating conditions to produce significant equivalent flows due to this compressibility. The compliance of the fluid and shock tube will be investigated in the sections below, and a dynamic state equation representing the fluid volumes will be derived.

2.4.1 Fluid Equation of State

A relationship between the density of a substance and its state (in terms of pressure and temperature, for example) is commonly called a state equation. The ideal gas law, as discussed in Sect. 2.8.2, is a state equation of this type. These state equations represent bond graph constitutive laws and are necessary in defining the dynamic state equation of generalized capacitive elements representing potential energy storage devices such as the fluid volumes on both sides of the piston.

For a contained liquid, density changes as a function of pressure and temperature are generally small. Approximating the density variation by a truncated Taylor series up to the linear terms results in

$$\rho = \rho_o + \left(\frac{\partial \rho}{\partial P}\right)_T (P - P_o) + \left(\frac{\partial \rho}{\partial T}\right)_P (T - T_o) \tag{2.1}$$

$$= \rho_o + \rho_o c(P - P_o) - \rho_o \alpha (T - T_o). \tag{2.2}$$

The parameters c and α are defined as the isothermal compressibility and volume expansivity, respectively.

$$c \equiv \frac{1}{\rho_o}\left(\frac{\partial \rho}{\partial P}\right)_T \tag{2.3}$$

$$\alpha \equiv -\frac{1}{\rho_o}\left(\frac{\partial \rho}{\partial T}\right)_P \tag{2.4}$$

Because the specific volume, v, is the inverse of density, then

$$\left(\frac{\partial \rho}{\partial P}\right)_T = \left(\frac{\partial}{\partial P}\left(\frac{1}{v}\right)\right)_T = -\frac{1}{v^2}\left(\frac{\partial v}{\partial P}\right)_T. \tag{2.5}$$

The Taylor series is taken about a condition in a system which conserves mass. Therefore, the isothermal compressiblity may be written from Eqns. (2.3) and (2.5) as

$$c = -\frac{1}{v_o}\left(\frac{\partial v}{\partial P}\right)_T = -\frac{1}{V_o}\left(\frac{\partial V}{\partial P}\right)_T. \tag{2.6}$$

Compressibility is then also the fractional change in volume divided by the change in pressure required to compress the fluid. It is always positive in magnitude because for any liquid the isothermal change in volume with increasing pressure is negative.

Equation (2.6) may be inverted for continuous and smooth partial derivatives. What results defines the isothermal bulk modulus (or simply bulk modulus) of a fluid.

$$\beta = \frac{1}{c} = -V_o \left(\frac{\partial P}{\partial V}\right)_T \tag{2.7}$$

The bulk modulus, in turn, defines the fluid stiffness because it is the increase in pressure for a fractional change in fluid volume. Therefore, it is a property which will have a significant impact on the dynamic performance of a system [17]. Leroy and Leslie referred to this definition as a "static" bulk modulus "applied to a system that changes pressure and volume very slowly allowing heat to flow in or out of the fluid as the PV relationship changes" [16]. They refer to the isentropic or adiabatic bulk modulus, defined for a constant entropy process by

$$\beta_{isen} = -V_o \left(\frac{\partial P}{\partial V}\right)_S \tag{2.8}$$

as a "dynamic" bulk modulus. A constant entropy process is generally more appropriate to a shock absorber application. However, Merritt mentions that the adiabatic and isothermal bulk moduli are related by

$$\beta_{isen} = \frac{C_p}{C_v}\beta \tag{2.9}$$

and because the ratio of specific heats is approximately unity for liquids ($\frac{C_p}{C_v} \simeq 1.04$ for petroleum-based fluids), the distinction is "difficult to justify ... in applications where entrained air and mechanical compliance are significant" [17]. As a result, the isothermal bulk modulus will be used in this study.

A liquid's effective bulk modulus is reduced by a container's elasticity and undissolved gas entrained in the liquid or the liquid changing state due to cavitation. The

term β will be considered to be an effective bulk modulus for now. An accounting of the individual effects of the fluid and container will be made when the compliance of the fluid volume is evaluated in the following section.

The derivative of density with respect to pressure at constant temperature linearized about an operating condition is from Eqns. (2.3) and (2.7)

$$\left(\frac{\partial \rho}{\partial P}\right)_T = \frac{\rho_o}{\beta}. \tag{2.10}$$

Volume expansivity (or cubical expansion coefficient) may be written as

$$\alpha = \frac{1}{V_o}\left(\frac{\partial V}{\partial T}\right)_P \tag{2.11}$$

assuming mass is conserved and smooth partial derivatives in analogy to the bulk modulus derivation. Fluid volume changes due to temperature are typically negligible for most applications due to fluid expansivities which are very low. Merritt [17] cites examples of petroleum-based fluids where the change in volume is about 5% for each 100F of temperature increase. In addition, the nitrogen gas chamber of a monotube shock absorber accounts for fluid volume changes due to temperature during use. As a result, the effect of temperature changes on fluid density or volume will be ignored in this study. The state equation for a fluid may then be written from Eqns. (2.1) and (2.10).

$$\rho = \rho_o \left[1 + \frac{1}{\beta}(P - P_o)\right] \tag{2.12}$$

Conventionally, the operating point for ρ_o considered is the fluid density at zero pressure [2, 17]. In this case, it is written as

$$\rho = \rho_o \left[1 + \frac{1}{\beta}P\right]. \tag{2.13}$$

A time dependent state equation for a fluid may be written by differentiating Eqn. (2.13) with respect to time.

$$\frac{d\rho}{dt} = \frac{\rho_o}{\beta}\frac{dP}{dt}. \tag{2.14}$$

2.4.2 Fluid Capacitor State Equation

The dynamic state equation for the fluid volumes on either side of the piston must be time dependent by definition. The fluid compliance must connect to the flow junction because flow enters and exits the volume from the channels across the piston. The fluid volume is a control volume with the following expression for conservation of mass.

$$\Sigma \dot{m}_{in} - \Sigma \dot{m}_{out} = \frac{dm}{dt} = \frac{d}{dt}(\rho V) = \rho \frac{dV}{dt} + V \frac{d\rho}{dt} \tag{2.15}$$

The density, ρ, is constant throughout the control volume assuming a lumped parameter model of the fluid in the volume. Then Eqn. (2.15) may be written as a flow continuity expression.

$$\Sigma Q_{in} - \Sigma Q_{out} = \frac{dV}{dt} + \frac{V}{\rho}\frac{d\rho}{dt}. \tag{2.16}$$

Substituting Eqns. (2.13) and (2.14), into Eqn. (2.16) produces a continuity expression in bond graph power variables.

$$\Sigma Q_{in} - \Sigma Q_{out} = \frac{dV}{dt} + \frac{V}{1 + \frac{P}{\beta}}\frac{1}{\beta}\frac{dP}{dt} \tag{2.17}$$

However, the bulk modulus of petroleum-based liquids is on the order of $1.4 \times 10^9 - 1.5 \times 10^9$Pa ($\simeq$ 220,000psi) [7, 17]. As a result, Eqn. (2.17) can be simplified to

$$\Sigma Q_{in} - \Sigma Q_{out} = \frac{dV}{dt} + \frac{V}{\beta}\frac{dP}{dt}. \tag{2.18}$$

for applications where the operating pressures are much smaller in magnitude than the bulk modulus (i.e. $\beta \gg P$). The first term of Eqn. (2.18) on the right side represents the incompressible flow change due to the control volume expanding or contracting when, for example, the piston moves relative to the tube. The second term on the right side is the compressible flow change due to pressure variation in the volume [17].

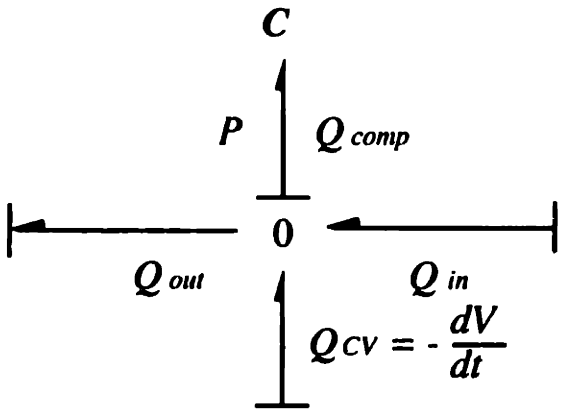

Figure 2.2: Bond graph for a compressible fluid in a control volume

In bond graph notation, the second term of Eqn. (2.18) defines a fluid capacitor which is integrably causal due to imposed flows. In order to see this, Eqn. (2.18) is rewritten as

$$\dot{P} = \frac{\Sigma Q_{in} - \Sigma Q_{out} - \frac{dV}{dt}}{C} \tag{2.19}$$

where, the compliance is

$$C = \frac{V}{\beta}. \tag{2.20}$$

The three terms in the numerator are (1) the fluid flow into the capacitor (or control volume), (2) the fluid flow out of the capacitor, and (3) the effective flow due to the boundaries of the capacitor moving. The net "flow" defines both flow lost due to the compressibility of the fluid and the change in pressure due to this effect. Therefore, a system state results when compressibility effects are considered. A general bond graph for a compressible fluid capacitor is shown in Figure 2.2. Flow into the capacitor reducing the size of the control volume, thereby increasing the pressure of the fluid inside the volume, is considered positive work by the sign convention of this bond graph. In the following sections, the compliance of each component of the capacitor will be examined.

Bulk Modulus of a Compressible Liquid

The bulk modulus of a compressible liquid is defined by Eqn. (2.7). It is typically on the order of $1.4 \times 10^9 - 1.5 \times 10^9$Pa ($\simeq$ 220,000 psi) for petroleum-based liquids at zero pressure as discussed previously. The bulk modulus is fairly constant over the range of typical operating conditions and, as a result, is handled as a handbook property.

Bulk Modulus of a Cylindrical Container

The bulk modulus for a cylindrical container is defined by "reflecting" the stiffness of the container into the fluid domain such that its effects can be computed using the power variables of the fluid domain (i.e. P, V). The diametral compliance of a pressurized cylinder with capped ends in the mechanical domain may be expressed as [29]

$$\frac{\Delta D_i}{\Delta P} = \frac{D_i}{E}\left[\frac{(1+\nu)D_o^2 + (1-2\nu)D_i^2}{D_o^2 - D_i^2}\right] \tag{2.21}$$

The change in container volume due to the change in diameter is

$$\Delta V_c = \frac{\pi}{4} L\left[D_i^2 - (D_i + \Delta D)^2 L\right] \simeq \frac{\pi}{2} L D_i \Delta D \tag{2.22}$$

neglecting higher order terms and the axial deflection of the cylinder. Combining Eqns. (2.21) and (2.22) with the expression defining bulk modulus (Eqn. (2.7)) produces an equivalent bulk modulus for a cylindrical container linearized about the undeflected volume, $V_c = V_o$.

$$\beta_c = \frac{E}{2}\left[\frac{D_o^2 - D_i^2}{(1+\nu)D_o^2 + (1-2\nu)D_i^2}\right] \tag{2.23}$$

Equation (2.23) is the bulk modulus due to the reflection of the container mechanical compliance into the fluid domain. Note, Eqns. (2.23) has a different sign than 2.7 because increasing pressure results in increasing container volume, and the compliance

due to axial deflection of the cylinder has been neglected. In Appendix A, it is shown that the change in volume due to circumferential strain is much larger than that due to axial strain for realistic shock absorber dimensions and materials. The axial change in volume due to the piston motion within the tube is generally orders of magnitude larger than the axial elastic deflections. As a result, compliance effects due to circumferential elastic strains and longitudinal changes in volume due to piston motion are considered in this analysis, while the effects of elastic strains are neglected.

Cavitation Model and the Bulk Modulus of an Entrapped Gas

The pressure within a cylinder volume can drop well below atmospheric pressure under normal operating conditions. Some pure liquids can sustain tensile stresses hundreds of times greater in magnitude than atmospheric pressure without rupturing. When a liquid does rupture under the influence of tensile stresses, the rupture of the fluid manifests itself as a number of very small cavities in the liquid. The process of cavitation is quite complex and depends, among other considerations, on the purity of the liquid and the rate at which the liquid is stressed. See Trevena [27] and Plesset and Prosperetti [19] for excellent reviews of research involving cavitation and bubble dynamics.

Lamb [14] discusses how contaminates in fluids outside of a laboratory environment will contain microscopic amounts of air and fluid vapor. These bubbles act as cavity nucleation sites and reduce the rupture strength of a liquid in practical terms to the fluid vapor pressure (for rapid rupture) or the gas saturation pressure (for slow rupture). He describes three forms of cavitation:

(i) Vaporous cavitation is the process where cavities of the liquid's own vapor are formed when the pressure drops below the vapor pressure of the liquid. Vaporous cavitation involves a change of fluid state and occurs rapidly. The time for a cavity

to grow from a microscopic nucleus to a 0.2mm sphere is on the order of 10^{-6}s.
(ii) Gaseous cavitation is the process where a non-condensible gas (usually air) dissolved in the fluid comes out of solution when the pressure drops below the saturation pressure of the liquid. Therefore, this form of cavitation involves mass transfer across the cavity wall and occurs slowly by comparison to vaporous cavitation. The time for this type of cavity to grow from a microscopic nucleus to a 0.2mm sphere is on the order of 1 to 10s. Faster rates are possible in a highly agitated liquid.
(iii) Pseudo cavitation, as the name suggests, is not really cavitation at all but the process by which non-condensible gas bubbles, such as entrained air, grow within a liquid in response to reducing pressure. No mass transfer occurs. Lamb does not discuss the rate of this bubble growth.

Lamb goes on to say that gaseous and pseudo cavitation occur when the pressure drops below the saturation pressure but above the fluid vapor pressure. All three forms of cavitation occur if the pressure drops below the vapor pressure [14]. The unrealistic result of large negative cylinder pressures will occur for normal shock operating conditions if one does not account for one or more forms of cavitation.

For all forms of cavitation, there is a reverse process which has not been discussed as yet where the cavities collapse when the pressure increases. The problem in this shock absorber problem is how to calculate how much of any one type of cavitation is occuring at a given instant and at what rate. This process begins by calculating an equivalent oscillation frequency for both the vapor and gaseous cavitation spheres described above. The oscillation frequency of the vapor cavitation sphere would be well beyond the range of frequencies for which the shock absorber model in this study would be of any use. Gaseous cavitation would only have an opportunity to occur at low frequencies (0.1 to 1Hz). Pseudo cavitation will occur under most conditions assuming some amount of air bubbles are present which do not dissolve or come out

of solution.

The cavitation model in this study is based on the following assumptions:
(i) The potential frequency of vaporous cavitation exceeds the frequency range under study by orders of magnitude, and sufficient nucleation sites in the form of air bubbles exist within the cylinder volumes such that the vapor pressure of the fluid is the limiting lower bound on the pressure of the fluid capacitors.
(ii) Gaseous cavitation will not have time to occur in any significant amount at the frequencies considered.
(iii) Pseudo cavitation occurs instantaneously and is governed by the ideal gas law.
The resulting simplified bubble model considers the growth and contraction of both air and vapor bubbles. This model will be compared to the one Lang [15] used for his model of a dualtube shock absorber.

Lang suspected that the lower pressure limit in the rebound and compression chambers was most likely a result of the entrapped air rather than vaporization of oil. He found the vapor pressure of the oil used in his dual tube shock absorber was less than 0.2psi based on his inability to boil the fluid by pumping a flask containing the liquid down to that pressure. However, he estimated the lower pressure limit to be 9 to 10psi in the compression chamber and 0 to 1psi in the rebound chamber. From these observations of actual shock absorber data he concluded that it was not "the generation of vapor (at the vapor pressure of the fluid) that accounts for the lower pressure limit in the chambers, but rather expansion of gas entrapped in the liquid as the pressure approaches zero absolute" [15]. Therefore, Lang suspected pseudo cavitation rather than vaporous cavitation as the determining factor of the lower pressure limit in the shock absorber chambers.

A low pressure dualtube shock absorber of the type Lang used in his study has a third chamber called a reserve chamber which serves the same purpose as the nitrogen

chamber of a monotube. During the compression stroke of a dual tube shock, the oil displaced by the difference in piston areas flows into a reserve chamber. Air at approximately atmospheric pressure can mix freely with the liquid entering the reserve chamber. Oil containing entrained air bubbles can then pass into the compression chamber of the shock absorber on the rebound stroke. These bubbles in the compression chamber must collaspe on the subsequent compression stroke before the pressure in this chamber rises significantly again. This effect is called "compression lag" and is a consequence of the liquid-air interface in the reserve chamber of dualtube shock absorbers.

Lang explained the lower pressure limit of the rebound chamber was a result of the fact that less entrapped gas made it into the rebound chamber because there is no direct path between the reserve and rebound chambers. However, he did believe it was possible that vaporous cavitation might take place in the rebound chamber with the bubbles as nucleation sites.

Lang got around the problem of large negative pressures by generating an equivalent flow simulating the formation of a gas which would prevent the pressure from dropping below 6psi. This limiting pressure was intended to account for any gas phase (pseudo or vaporous) in the fluid. The role of gaseous cavitation was not discussed in Lang's work potentially due to the fact he was concerned with damper characteristics at high frequency.

The following can be summarized when the cavitation/bubble model derived in this study for a monotube shock absorber is compared to the model used by Lang. Lang established a single pressure limit intended to represent both gaseous and pseudo cavitation phenomena. In this study, the growth of bubbles due to pseudo cavitation is based on the ideal gas law and an assumption of the initial amount of entrained air in the oil. The limiting lower pressure is established by an estimate of the oil

vapor pressure and considers the role of vapor cavitation. Both methods neglect the role of gaseous cavitation. From a bond graph perspective, the process of cavitation may be viewed as a nonlinear effect due to the compliance of the fluid capacitor. The compliance effectively becomes infinite when the pressure drops to the vapor pressure of the fluid.

The phenomena of pseudo cavitation reduces the effective bulk modulus of the fluid. Ruling out any substantial air pockets, the air will take the form of air dissolved in the liquid working fluid or entrained as bubbles. Air dissolved in the fluid typically has a negligible effect on bulk modulus. Air in the form of bubbles has a significant effect on the dynamic response of systems [2, 14, 17] because air is 10,000 times more compressible than oil, and estimates of entrained air in some hydraulic systems run as high as 20% at atmospheric conditions [17].

Assuming the pressure changes are so rapid that there is negligible heat transfer between the bubbles and the fluid for our lumped parameter model and that only small changes in bubble volume occur. The bulk modulus for air entrained as bubbles in the petroleum-based liquid working fluid is defined from the ideal gas state equation assuming the process is adiabatic and reversible (i.e. an isentropic process).

$$PV_a^\gamma = const. \tag{2.24}$$

The bulk modulus is found by differentiating the gas state equation

$$\Delta P V_a^\gamma + P\gamma V_a^{\gamma-1}\Delta V_a = 0 \tag{2.25}$$

then the bulk modulus from Eqns. (2.7) and (2.25) produces an equivalent bulk modulus for the entrained air.

$$\beta_a = \gamma P \tag{2.26}$$

Not only does the bulk modulus decrease as the pressure decreases, but the bubbles in which the air is trapped also grow. The bubble growth produces an effective flow

as the air takes up more space in proportion to the fluid at lower pressures. The volume of air entrained as bubbles based on the assumption of an isentropic process is

$$V_a = V_{ao}\left(\frac{P_{ao}}{P}\right)^{\frac{1}{\gamma}}. \tag{2.27}$$

Decreasing pressure in the volume will result in additional flow from the air dissolved in the oil coming out of solution due to gaseous cavitation. The amount of air dissolved in mineral oil at 1 atmosphere is about 9% [16]. Other researchers have examined this problem and empirically derived a coefficient to account for the air bubble volume variation due to the variation of the ratio of entrained-to-dissolved air content in the oil [30]. Gaseous cavitation effects are not modelled in this study due to the slow rate of this form of cavitation.

Effective Compliance of Fluid Volume

The effective compliance of the fluid volume is a result of all the compliant elements within the system. Assuming the fluid completely fills the container at any given instant, the total volume of the container is

$$V = V_l + V_a. \tag{2.28}$$

A pressure increase is exerted on the mixture by piston motion. This motion over a period of time sweeps out a volume,

$$\Delta V_p = -\Delta V_l - \Delta V_a + \Delta V_c. \tag{2.29}$$

The first two terms are negative because a flow into the volume (positive bond graph convention) from the piston reduces the volume of the liquid and air increasing the pressure, and the third term is positive because the container volume increases when the pressure in the container rises.

The pressure within the volume is the same for all elements. Therefore, the stiffnesses of the components are additive like springs in series. Combining Eqn. (2.7) for the total volume and Eqn. (2.29) produces an equation for the effective bulk modulus of the system relative to the flow source (the piston) upon which the effort is exerted.

$$\frac{1}{\beta} = \frac{-\Delta V_l - \Delta V_a + \Delta V_c}{V \Delta P} \tag{2.30}$$

$$= \frac{V_l}{V}\left(\frac{-\Delta V_l}{V_l \Delta P}\right) + \frac{V_a}{V}\left(\frac{-\Delta V_a}{V_a \Delta P}\right) + \frac{V_c}{V \Delta P} \tag{2.31}$$

$$= \frac{V_l}{V}\left(\frac{1}{\beta_l}\right) + \frac{V_a}{V}\left(\frac{1}{\beta_a}\right) + \frac{1}{\beta_c} \tag{2.32}$$

The effective compliance expressed in terms of the individual bulk moduli of the system components is from Eqns. (2.20), (2.28), and (2.32)

$$C = \frac{V - V_a}{\beta_l} + \frac{V_a}{\beta_a} + \frac{V}{\beta_c} \tag{2.33}$$

where the volume of the chamber is given by

$$V = V_o + \Delta V_c + \int_0^{t'} Q_{rp}(t) dt \tag{2.34}$$

where V_o is the initial volume, ΔV_c is given by Eqn. (2.22), and Q_{rp} is determined by the flow from the piston. Note that the effective compliance is a nonlinear function of the chamber pressure and volume, container material properties and geometry, and liquid and gas properties. Also, the effective compliance is infinite when the pressure drops to the vapor pressure of the fluid.

2.4.3 Piston Leakage Flow

The piston leakage flow between the rod and headside capacitances occurs due to the very narrow gap between the piston and shock tube. The flow is laminar due to dominant viscous effects. The flow through this annulus is approximated by modelling

the flow in a narrow gap between two plates. The fluid velocity for flow between two plates is given by

$$U = \frac{1}{2\mu}\frac{dP}{dl}y^2 + \frac{A}{\mu}y + B \tag{2.35}$$

where, U is the flow velocity relative to the plates, and A and B are constants of integration depending on the boundary conditions [26]. The following is assumed about the annulus flow.

(i) The pressure gradient, $\frac{dP}{dl}$, in the annulus is constant along its length.

(ii) The gap is small enough that the flow is always laminar.

(iii) The piston and tube are concentric.

(iv) The gap is small relative to the radius of the piston and constant along the length of the annulus.

(v) A no slip condition exists between the fluid and the walls defined by the piston and tube.

The expression in Eqn. (2.35) may be used for the annulus flow problem resulting in the expression,

$$U = \frac{1}{2\mu}\frac{\Delta P}{L_p}(y^2 - g_p y) + \frac{\dot{x}_p - \dot{x}_t}{g_p}y. \tag{2.36}$$

Integrating to get flowrate for the annulus yields an expression in terms of states and the input, yields

$$Q_{pk} = \pi D_i \left[\frac{1}{12\mu}\frac{g_p^3}{L_p}(P_r - P_h) + \frac{1}{2}g_p(\dot{x}_p - \dot{x}_t)\right]. \tag{2.37}$$

Note that the gap is generally a function of the pressures within the tube because of the tube compliance. Also, eccentric annuli have lower effective resistances. Dransfield [6] comments that the fully eccentric case, where the piston touches the tube, has a resistance 0.4 times that of the concentric case. The flow increase for this case would be 2.5 times that of the concentric case for the same pressure gradient.

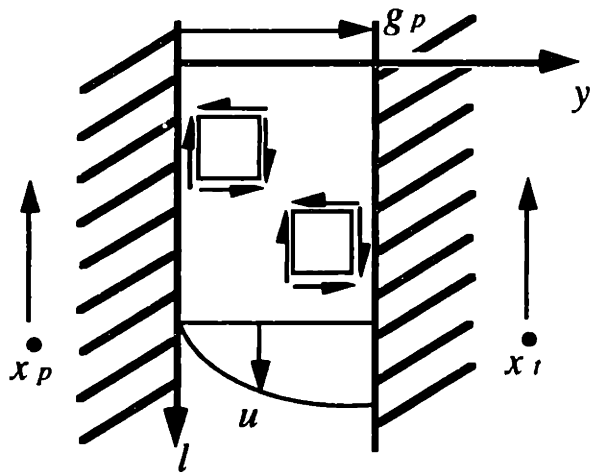

Figure 2.3: Leakage flow model in gap between piston and tube

2.4.4 Tube-Piston Viscous Friction

The viscous friction force on the piston is required to calculate the state related to the piston when the shock is installed in an automobile and the damping load. Deriving an expression for the viscous friction at the interface between the piston and tube requires building on the expression for the leakage flow in the annulus derived above. The fluid between the piston and tube is sheared and produces a damping force. The assumptions made for this problem will be the same as those made for the leakage flow.

The shear stresses of the fluid are expressed by Newton's law of viscosity in one dimension.

$$\tau = \mu \frac{dU}{dy} \tag{2.38}$$

Frictional shear force is then

$$F_\tau = A_{wp} \mu \frac{dU}{dy} \tag{2.39}$$

where

$$A_{wp} = \pi D_i L_p. \tag{2.40}$$

Differentiating Eqn. (2.36) yields

$$\frac{dU}{dy} = \frac{1}{2\mu}\frac{\Delta P}{L_p}(2y - g_p) + \frac{\dot{x}_p - \dot{x}_t}{g_p} \tag{2.41}$$

where

$$\Delta P = P_h - P_r. \tag{2.42}$$

Substitution of Eqns. (2.41) and (2.42) into (2.39) produces the general shear force expression within the laminae.

$$F_\tau = A_{wp}\left[\frac{y - \frac{1}{2}g_p}{L_p}(P_h - P_r) + \frac{\mu}{g_p}(\dot{x}_p - \dot{x}_t)\right] \tag{2.43}$$

This is the shear force within the fluid. Figure 2.3 indicates a positive shear stress convention for a shear force in the fluid. Hence, the shear force on the fluid at the piston interface is for $y = 0$

$$F_\tau(0) = A_{wp}\left[\frac{g_p}{2L_p}(P_r - P_h) + \frac{\mu}{g_p}(\dot{x}_p - \dot{x}_t)\right]. \tag{2.44}$$

The force on the piston at the interface is equal and opposite to that on the fluid.

$$F_{\tau p}(0) = -F_\tau(0) = -A_{gx}(P_r - P_h) - R_{gx}(\dot{x}_p - \dot{x}_t) \tag{2.45}$$

where

$$A_{gx} = \frac{\pi}{2}D_i g_p \tag{2.46}$$

$$R_{gx} = \frac{\mu}{g_p}A_{wp}. \tag{2.47}$$

The sign convention was selected such that a positive friction force would be in the opposite direction to a positive piston velocity, thereby, representing a resistive element. The force on the tube at $y = g_p$ is

$$F_{\tau t}(g_p) = -F_\tau(g_p) = -A_{gx}(P_r - P_h) + R_{gx}(\dot{x}_p - \dot{x}_t). \tag{2.48}$$

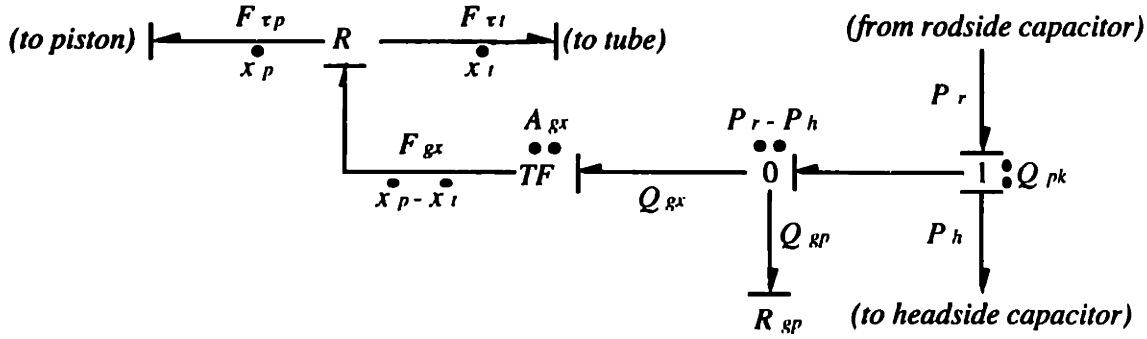

Figure 2.4: Piston-tube viscous friction interface bond graph model

A positive friction force on the tube is opposite to a positive displacement of the tube. As one would expect, the viscous forces are equal and opposite on the piston and tube in the absence of any significant pressure gradient. The pressure gradient will exert the same shear force on either member because we have ignored the curvature in the problem.

The entire system can be described in the bond graph in Figure 2.4 with an R-field and a transformer element to bridge the gap between the fluid and mechanical domains. The boundary conditions are defined by sources representing states and the input.

The flow-junction compatibility equation is

$$Q_{pk} = Q_{gp} + Q_{gx} \tag{2.49}$$

where Q_{pk} is the total leakage flow from one side of the piston to the other through the gap, Q_{gp} is the flow due to the pressure difference across the piston, and Q_{gx} is the flow due to the piston shearing motion (compare to Eqn. (2.4.3)).

The constitutive relationships for the elements are given below.

(i) The constitutive equation for the resistor in the fluid domain representing the

piston blockage is

$$Q_{gp} = \frac{P_r - P_h}{R_{gp}} \tag{2.50}$$

where

$$R_{gp} = \frac{12\mu L_p}{\pi D_i g_p^3} \tag{2.51}$$

by Eqn. (2.4.3).

(ii) The transformer between domains is defined by

$$Q_{gx} = A_{gx}(\dot{x}_p - \dot{x}_t) \tag{2.52}$$

$$F_{gx} = A_{gx}(P_r - P_h). \tag{2.53}$$

(iii) The output forces of the explicit R-field in the mechanical domain are defined by Eqns. (2.45) and (2.48). The third output of the R-field is the relative velocity of the piston and tube which is determined by a system state and the input to the system.

2.4.5 Rodside and Headside State Equations

All the expressions required to write the dynamic state equations for the rod and headside fluid capacitors have been derived. However, a summary is in order after all the derivations. A state equation for a capacitor representing a fluid volume under pressure was given by Eqn. (2.19). Where the net flow into the capacitor represents the volume lost (or gained) due to small fluid density changes. The compliance is defined for the volume by the Eqn. (2.33) and is due to the fluid, any vapor phase or entrained gas, and the compliance of the tube reflected into the fluid domain. A bond graph of the rodside volume is shown in Figure 2.5 for illustrative purposes.

The net flow into the rod and headside volumes may be written in terms of the states of the problem and the input from the bond graph flow junctions in Figures 2.5 and 2.15

$$Q_r = Q_{rp} - Q_{rt} - N_{pr}Q_{pr} + N_{pc}Q_{pc} - Q_{pk} \tag{2.54}$$

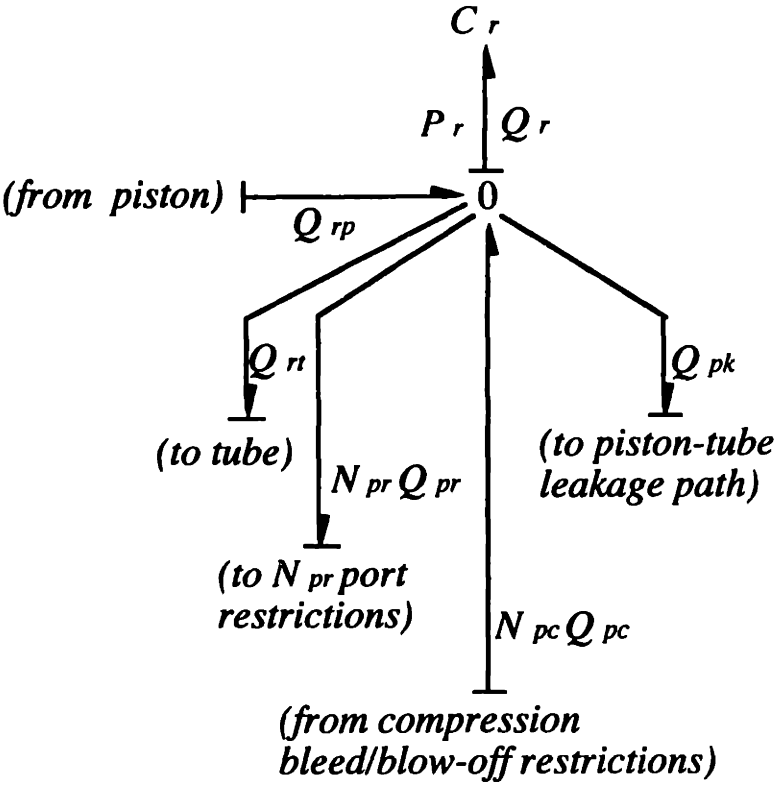

Figure 2.5: Rodside fluid capacitor

$$Q_h = -Q_{hp} + \dot{V}_g + N_{pr}Q_{pr} - N_{pc}Q_{pc} + Q_{pk} \tag{2.55}$$

where the flows due to the piston, tube, and floating piston motion are

$$Q_{rp} = A_r\dot{x}_p \tag{2.56}$$

$$Q_{rt} = A_r\dot{x}_t \tag{2.57}$$

$$Q_{hp} = A_h\dot{x}_p \tag{2.58}$$

$$Q_{gt} = A_h\dot{x}_t \tag{2.59}$$

and $\dot{V}_g$ will be given by Eqn. (2.154). The orifice flows across the piston from the rebound and compression chambers (i.e. $N_{pr}Q_{pr}$ and $N_{pc}Q_{pc}$) are given by state equations, Eqns. (2.86) and (2.87), respectively. The leakage flow is defined in terms of states and the input by Eqn. (2.49).

The state equations for the fluid volumes are then

$$\dot{P}_r = \begin{cases} \frac{Q_r}{C_r} & \text{for } P_r > P_v \\ 0 & \text{for } P_r = P_v \end{cases} \tag{2.60}$$

$$\dot{P}_h = \begin{cases} \frac{Q_h}{C_h} & \text{for } P_h > P_v \\ 0 & \text{for } P_h = P_v \end{cases} \tag{2.61}$$

Limits must be included on the integration process of the state equations such that the pressure will not drop below the oil vapor pressure in order to consider the effects of vaporous cavitation as discussed in Sect. 2.4.2. This is the implementation used to consider the effects of cavitation rather than setting the compliances to infinity when the pressure drops to the vapor pressure. The vapor pressure of petroleum oil is 0.001mm of mercury ($\simeq$ 0.1Pa) at 120F [16] and will be approximated by zero in this study. This is consistent with the observations of Lang in his study to obtain the vapor pressure of the fluid in his shock absorber (see Sect. 2.4.2).

2.5 Port Flow States and Cross Piston Duct Models

The fluid inertia for flow in ducts or pipes can become a significant effect on system performance, particularly if the duct is long or the flow has a large oscillatory component (i.e. frequency). Piston restrictions are typically short in length but the input frequency to the piston can be high. In the following sections, the effect of the fluid resistance and inertia are investigated, and the state equations resulting from the integral causality of piston restrictions are derived.

2.5.1 Fluid Inertia of Port Restriction

The inertia of the fluid in the port restriction has a preference toward integral causality assuming the volumes of fluid (rod and headside capacitors) on either side of the

piston are integrably causal. The actual inertial pressure loss, however, is small when compared to the pressure drop across the piston.

2.5.2 Fluid Resistor Analysis of Port Restriction

This thesis models the port restriction as a short tube with a check valve in line which prevents flow until the pressure difference across the restriction exceeds the set value of the valve. The inertia of the fluid is considered as is the reversible and irreversible pressure losses due to fluid flow.

Viscous Loss Coefficient

Frictional losses in fluid flow result from fluid viscosity which is not considered in the Bernoulli equation. In an energy formulation, the work of viscous forces enters via the internal energy term. This term can be expressed as an irreversible conversion of kinetic energy into internal energy (heat) due to viscous shearing. The loss coefficient, K, accounts for both irreversible static pressure losses, as well as for reversible kinetic energy conversions, as will be discussed.

$$\Delta P = \frac{\rho}{2}\frac{K}{A^2}Q^2 \tag{2.62}$$

The loss coefficient is intended to account for wall friction losses over a long length of pipe, known as major losses, or turbulent mixing losses from sudden flow area changes over a short length of pipe, known as minor losses. Major losses occur in fully developed flow which does not occur in the short ducts of shock absorbers and is, therefore, outside the scope of this thesis. However, abrupt changes in flow area do occur in shock absorbers. The loss coefficient can also be used to account for reversible conversions from static pressure (potential energy) to dynamic pressure (kinetic energy), as in the case of gently changing flow areas.

The loss coefficient is instrumental in defining a fluid resistor constitutive law in bond graph notation. Several constitutive formulations are investigated in the following sections for typical turbulent losses.

Exit Losses

We will begin the analysis of the static pressure losses by first accounting for the losses at the discharge of the pipe (see Figure 2.6). Kays [12] developed the loss coefficient for a sudden expansion in a pipe based in part on the experimental work of Nusselt [18]. The following assumptions are necessary.

(i) Negligible wall friction over the section of the pipe.

(ii) Static pressures constant over a cross section.

(iii) Subsonic flow where the static pressure on the downstream face after a sudden expansion is equal to the static pressure in the stream just prior to the expansion.

(iv) Square-edged discharge.

Assumptions (ii) and (iii) above are from Nusselt's observations. The total loss coefficient due to sudden area changes for flow with a known velocity profile, from the application of conservation of momentum, is shown to be

$$K_{exit}^{net} = 2\frac{A_3}{A_4}\left[\alpha_4''\frac{A_3}{A_4} - \alpha_3''\right] \tag{2.63}$$

where α'' is a momentum correction at each cross section and is defined by

$$\alpha'' = \frac{\int_0^A v^2 dA}{A\overline{V}^2}. \tag{2.64}$$

The momentum correction terms arises from the fact that the 1-D approximation for the square of the average flow velocity, $\overline{V}$, times the flow area is not the same as the 2-D reality of the square of the flow velocity integrated over the area. The resulting loss expression assumes the flow profile before and after the expansion is known. The momentum correction term is approximately unity for turbulent flow due to a

nearly uniform velocity profile. Therefore, the ideal (reversible) loss coefficient for fully turbulent flow due to area changes is

$$K_{exit}^{ideal} = \left(\frac{A_3}{A_4}\right)^2 - 1. \tag{2.65}$$

The irreversible loss coefficient for any flow regime relative to fully turbulent flow ideal losses is found by comparing Eqn. (2.65), for ideal turbulent flow exit static pressure increases, with Eqn. (2.63), for total losses for any flow regime.

$$K_{exit}^{irrev} = 1 - 2\alpha_3'' \frac{A_3}{A_4} + (2\alpha_4'' - 1)\left(\frac{A_3}{A_4}\right)^2 \tag{2.66}$$

The irreversible loss coefficient for turbulent flow reduces to

$$K_{exit}^{irrev} = \left(1 - \frac{A_3}{A_4}\right)^2 \tag{2.67}$$

which is known as the Borda-Carnot relation.

If the discharge area is much larger than the inlet area ($A_4 \gg A_3$) , then the irreversible loss coefficient is unity and the ideal loss coefficient is -1. The net loss coefficient is zero which represents complete kinetic energy dissipation as heat during the turbulent mixing of fluid in the expansion. Note, that this is true whether the flow was initially turbulent or laminar in the duct.

Entrance Losses

Kays [12] also accounted for the entrance static pressure loss leading to the inlet of the tube and additional re-expansion losses beyond the inlet. An abrupt contraction can occur between a section upstream of the inlet and the flow in the pipe. The minimum jet area is known as the vena contracta and is formed approximately $\frac{1}{2}$ pipe diameters downstream of the inlet, where a sudden contraction occurs and the flow is turbulent.

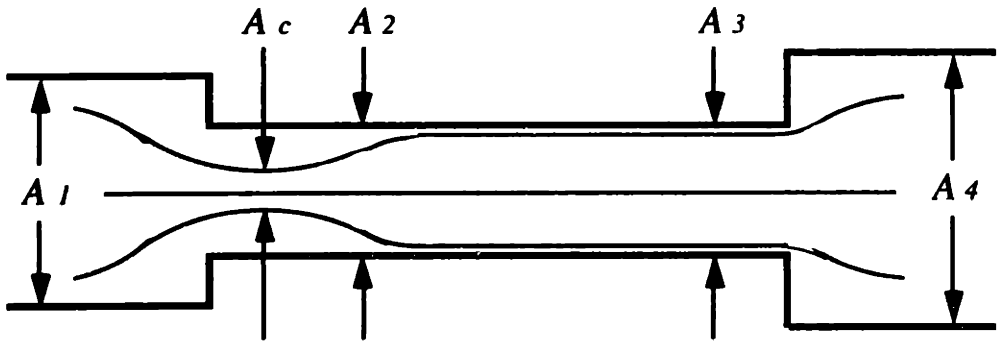

Figure 2.6: Minor losses due to abrupt flow area changes

The conversion of pressure energy to kinetic energy from the inlet to the vena contracta is very efficient. However, the expansion from the vena contracta is not. This re-expansion is where most of the irreversible viscous entrance losses occur. Well-rounded entrances mitigate these losses, whereas sharp-edged entrances amplify them. The contraction coefficient for a pipe entrance is defined as

$$C_c = \frac{A_c}{A_1} \tag{2.68}$$

and is a function of $\frac{A_2}{A_1}$ and inlet geometry.

Irreversible losses due to re-expansion can be determined by an analysis similar to that of the abrupt expansion. The velocity distribution at the throat of the vena contracta is essentially uniform due to a nozzle-like behavior. However, the upstream flow region may be non-uniform requiring a kinetic energy correction factor similar to the momentum correction factor described in the section on exit losses. The ideal (reversible) and irreversible loss coefficients, as well as the kinetic energy correction

factor, for entrance losses are given below.

$$K_{entrance}^{ideal} = 1 - \left(\frac{A_2}{A_1}\right)^2 \tag{2.69}$$

$$K_{vena}^{irrev} = \frac{C_c^2\left(2\alpha_2' - \alpha_1'\left(\frac{A_2}{A_1}\right)^2\right) - 2C_c + 1}{C_c^2} \tag{2.70}$$

$$\alpha' = \frac{\int_0^A v^3 dA}{A\overline{V}^3} \tag{2.71}$$

As before, a simpler form arises for turbulent flow where $A_1 \gg A_2$.

$$K_{vena}^{irrev} = \frac{C_c^2 - 2C_c + 1}{C_c^2} \tag{2.72}$$

The contraction coefficient has been cataloged by Rouse and Howe [21] versus area ratio $\frac{A_2}{A_1}$. An approximation for sharp-edged entrances where $A_1 \gg A_2$ are given by Merritt [17], Blevins [3], and others as $K_{vena}^{irrev} = \frac{1}{2}$. The vena contracta effect is minimized in well-rounded orifices and these same references give losses as low as $K_{vena}^{irrev} = 0.05$.

The question becomes, what is the total loss coefficient for the flow across a short pipe for all *Re* for either sharp or well-rounded inlets? Laminar flow at the inlet produces very low inlet losses because the vena contracta re-expansion losses tend to be negligible. Instead the laminar boundary layer at the inlet produces higher wall friction losses than turbulent losses. These effects are investigated in the following section.

Entrance Length Effects

Various researchers have investigated the entrance losses due to the laminar boundary layer formed in the entry of pipes even at high Reynolds numbers where the fully developed flow is turbulent. Shah [23] gives an excellent summary of this research while proposing a single closed form equation for the friction factor in flow through

circular tubes, parallel plates, equilateral triangular cross sections, and concentric annular ducts.

Shapiro and Smith [25] showed the boundary layer increases in thickness along the length of the pipe until it reaches a length Reynolds number of

$$Re_x = \frac{\rho L \overline{V}}{\mu} = 5 \times 10^5 \tag{2.73}$$

where the transition to a turbulent boundary layer occurs. Shapiro, Siegel, and Kline [24] experimentally determined that near the inlet where the boundary layer is small compared with the pipe radius, only 39% of the pressure loss is due to wall friction. The remaining 61% is caused by momentum flux to accelerate the fluid outside the boundary layer. Their expression for the inlet region pressure loss when the fully -developed flow was turbulent has been converted to an equivalent irreversible loss coefficient in Eqn. (2.74)

$$K_{bl}^{irrev} = 13.74\sqrt{\frac{\left(\frac{L}{D}\right)}{Re}} \quad \text{for well-rounded inlet with } \frac{\left(\frac{L}{D}\right)}{Re} < 10^{-3} \tag{2.74}$$

where the Reynolds number can be expressed in terms of bond graph flow variables.

$$Re = \frac{\rho D \overline{V}}{\mu} = \frac{\rho D \left(\frac{Q}{A}\right)}{\mu} \tag{2.75}$$

The incremental pressure drop is the difference between the total pressure drop from the inlet plane and the pressure drop which would have existed if the flow were fully developed from the inlet plane. The incremental pressure drop in the entrance length up to a region of fully developed laminar flow was theoretically derived by Bender [1]. Bender included the incremental loss with the loss for a fully developed flow profile over the entire length into a single expression for the total viscous losses in the tube.

$$K_{bl}^{irrev} = 1.25 + 64\frac{\left(\frac{L}{D}\right)}{Re} \quad \text{for well-rounded inlet with } \frac{\left(\frac{L}{D}\right)}{Re} > 0.06 \tag{2.76}$$

The first term is the incremental pressure loss, and the reader may recognize $\frac{64}{Re}$ as the friction factor for laminar flow in smooth pipes. (Chen [5] experimentally determined the incremental pressure drop and arrived at $1.20 + \frac{38}{Re} + 64\frac{\left(\frac{L}{D}\right)}{Re}$.) Bender combined his results with those of Shapiro, Siegel, and Kline producing the following expression to cover all $\frac{\left(\frac{L}{D}\right)}{Re}$ regimes for tubes with well-rounded inlets.

$$K_{bl}^{irrev} = 13.74\sqrt{\frac{\left(\frac{L}{D}\right)}{Re}} + \frac{1.25 + 64\frac{\left(\frac{L}{D}\right)}{Re} - 13.74\sqrt{\frac{\left(\frac{L}{D}\right)}{Re}}}{1 + 0.00018\left[\frac{\left(\frac{L}{D}\right)}{Re}\right]^{-2}} \tag{2.77}$$

Port Resistor Short Tube Model

In this thesis, a short tube model for the port resistor is used to consider the reversible and irreversible inlet and exit losses. The reversible static pressure losses as the fluid approaches the inlet region of the port resistors is determined by noting the diameter of the shock absorber tube is very large when compared to the port restriction. This is comparable to saying the fluid in the region entering the port restrictions is effectively static, which is consistent with our fluid capacitor model of the rod and headside volumes. The reversible loss coefficient is then unity by Eqn. (2.69) representing ideal conversion of static pressure energy to kinetic energy. The irreversible pipe losses are given by Bender's interpolation function, Eqn. (2.77), for all flow regimes and pipe length combinations. The net (reversible and irreversible) exit loss coefficient is $K_{exit}^{net} = 0$ regardless of whether the flow is laminar or turbulent assuming the discharge area is significantly larger than the duct (Eqns. (2.63)). This implies that all the kinetic energy is dissipated by turbulent mixing at the discharge.

A modified version of the Bender interpolation function is used to calculate the resistive static pressure losses across the "short" port restriction by combining the effects of (1) the reversible static pressure loss as the fluid approaches the inlet region, (2) the static pressure loss at the discharge, and (3) the irreversible losses in the pipe

due to the laminar inlet boundary layer occurring when the fully developed flow would be either turbulent or laminar and from the wall friction effects for laminar flow.

$$K_{tube}^{net} = 1 + 13.74\sqrt{\frac{\left(\frac{L}{D}\right)}{Re}} + \frac{1.25 + 64\frac{\left(\frac{L}{D}\right)}{Re} - 13.74\sqrt{\frac{\left(\frac{L}{D}\right)}{Re}}}{1 + 0.00018\left[\frac{\left(\frac{L}{D}\right)}{Re}\right]^{-2}} \tag{2.78}$$

Again, this expression is for well-rounded inlets and all $\frac{\left(\frac{L}{D}\right)}{Re}$. The entire static pressure loss for a tube with a well rounded inlet is then conveniently expressed from one side to the other side of the port restriction.

The interpolation function can also be modified to include the additional re-expansion loss coefficient for turbulent flow into sharp-edged inlets due to separation downstream of the vena contracta as given by Rouse and Howe [21] and Merritt [17]. This coefficient was experimentally derived to be $\frac{1}{2}$ and can be added to the interpolation function such that the effects of turbulent mixing losses for sharp-edged inlets are included with the effects of the laminar boundary layer.

$$K_{tube}^{net} = 1.5 + 13.74\sqrt{\frac{\left(\frac{L}{D}\right)}{Re}} + \frac{0.75 + 64\frac{\left(\frac{L}{D}\right)}{Re} - 13.74\sqrt{\frac{\left(\frac{L}{D}\right)}{Re}}}{1 + 0.00018\left[\frac{\left(\frac{L}{D}\right)}{Re}\right]^{-2}} \tag{2.79}$$

Losses due to the turbulent boundary layer have not been mentioned because the port restriction lengths are so short that a turbulent boundary layer will not form.

It is convenient at this point to introduce the concept of the discharge coefficient, C_d, which will be defined in terms of the loss coefficient by Eqn. (2.62).

$$K = \frac{\Delta P}{\frac{\rho}{2}\left(\frac{Q}{A}\right)^2} = \frac{1}{C_d^2} \tag{2.80}$$

The discharge coefficient is typically used in place of the loss coefficient for orifices (i.e. very short pipes). The static pressure loss will be expressed in terms of an equivalent discharge coefficient for a short tube in order to maintain consistency

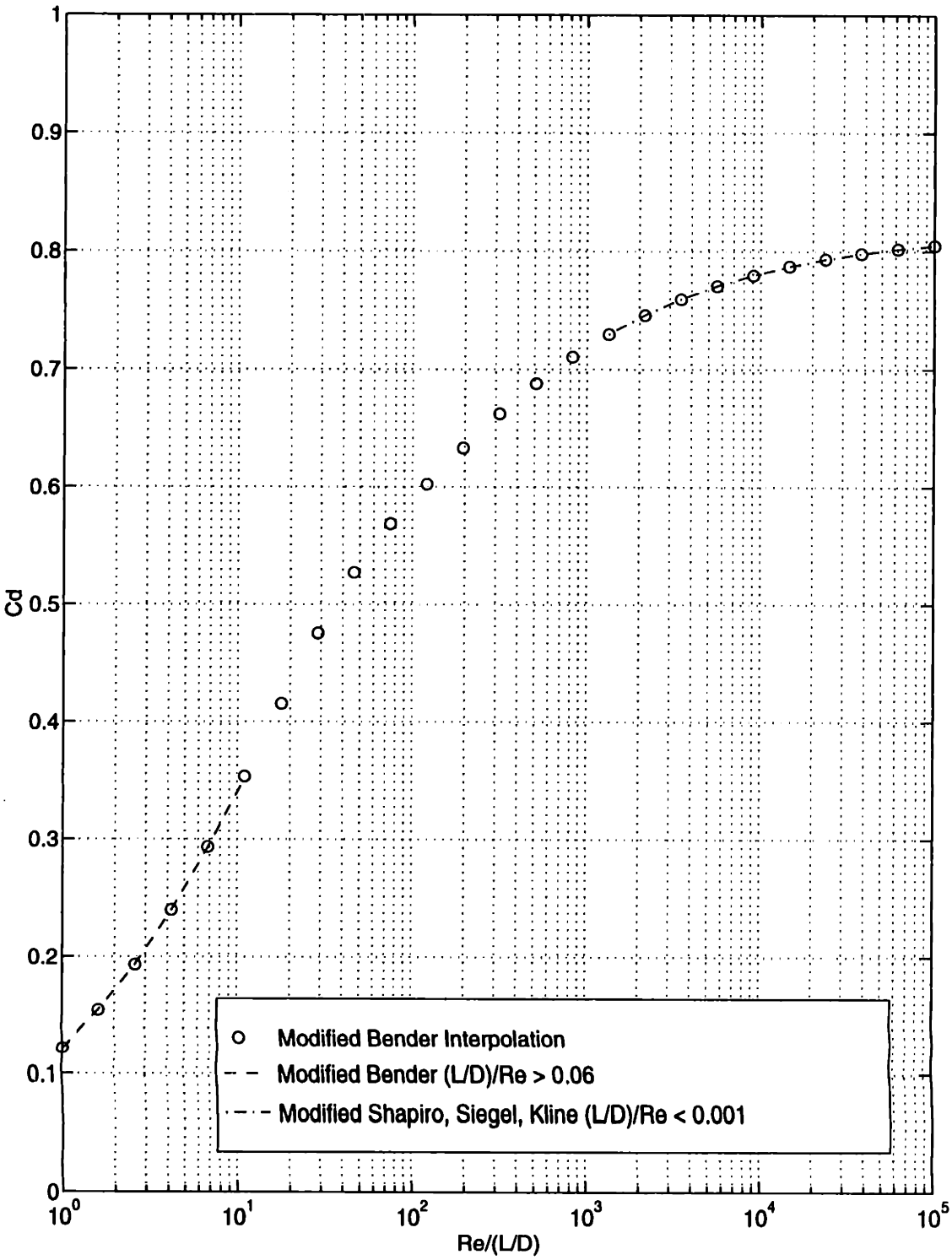

Figure 2.7: Equivalent discharge coefficient for sharp-edged circular restrictions

with the discharge coefficient of the bleed and relief valve orifices. Figure 2.7 plots the equivalent discharge coefficient for circular sharp-edged restrictions based on the modified Bender interpolation function for a wide range of $\frac{\left(\frac{L}{D}\right)}{Re}$.

2.5.3 Inertia vs. Resistance Pressure Losses

The static pressure loss for flow through a duct depends not only on the geometry and Reynolds number (i.e. velocity) but also the acceleration of the flow. Lang attempted to introduce the effects of accelerating flow through the use of an unsteady discharge coefficient which he attempted to measure in the orifices of the dualtube shock absorber he studied [15]. Lang tried to correlate a dynamic disharge coefficient to the acceleration of the fluid which he characterized using the acceleration number of the flow (see Sect. 2.6.1, Eqn. (2.95)).

The acceleration of the fluid is considered in this study through the inertial force due to the fluid momentum which Karnopp characterized for a bond graph model of a fluid-filled line [9].

$$p = IQ = \frac{\rho L}{A} Q \tag{2.81}$$

The inertia of the fluid in the line is $\frac{\rho L}{A}$. The inertia of the fluid becomes more significant as the duct becomes longer and smaller in cross sectional area. The port restrictions of a shock absorber are short, however. Because the fluid accelerations are potentially high, this effect becomes more significant when the fluid flow is lowest.

The pressure at the inlet and discharge of the restriction are prescribed by the state resulting from the volume of fluid on either side of the piston and the blow-off valve. It is then preferred from a modelling standpoint to make an independent state due to the inertia of the fluid. The resulting effort junction is written in integral

causality form, expressing the conservation of linear momentum,

$$I\dot{Q} = -R(Q)Q^2 + P \tag{2.82}$$

where $P = P_{in} - P_{out}$, or the pressure difference applied across the restriction.

Deciding whether the inertia pressure losses (or gains) due to fluid accelerations are significant as compared to the resistive pressure losses is difficult to know a priori, although intuitively one would think the inertia effects are small as compared to the resistive losses in the orifices of a shock absorber. In this thesis, both effects are considered in the port restriction model. A non-dimensional parameter based on bond graph notation is defined to compare the effects. The inertia pressure ratio is simply the instantaneous ratio of the inertia and resistive pressure losses.

$$\frac{P_I}{P_R} = \frac{I\dot{Q}}{R(Q)Q^2} = \frac{AL\dot{Q}}{\frac{Q^2}{2Cd^2}} \tag{2.83}$$

Another physical meaning to this parameter is the ratio of inertia pressure to the kinematic pressure dissipated. The results of this parameter are obtained during analysis of the shock absorber model to understand the relative importance of the inertia on the flow.

2.5.4 Port Flow State Equation

A portion of the system bond graph from Figure 2.1 is shown in Figure 2.8. This bond graph shows more detail in the region of the rebound port restriction. The state equation for the port flow can be written in terms of other states of the system. The compression port restriction equations are written by analogy.

$$P_{sir} = \begin{cases} P_r - P_h - P_{kr} - R_{pr}Q_{pr}^2 - P_{setr} & \text{for } Q_{pr} > 0 \\ P_r - P_h - P_{kr} - P_{setr} & \text{for } Q_{pr} \leq 0 \end{cases} \tag{2.84}$$

$$P_{sic} = \begin{cases} P_h - P_r - P_{kc} - R_{pc}Q_{pc}^2 - P_{setc} & \text{for } Q_{pc} > 0 \\ P_h - P_r - P_{kc} - P_{setc} & \text{for } Q_{pc} \leq 0 \end{cases} \tag{2.85}$$

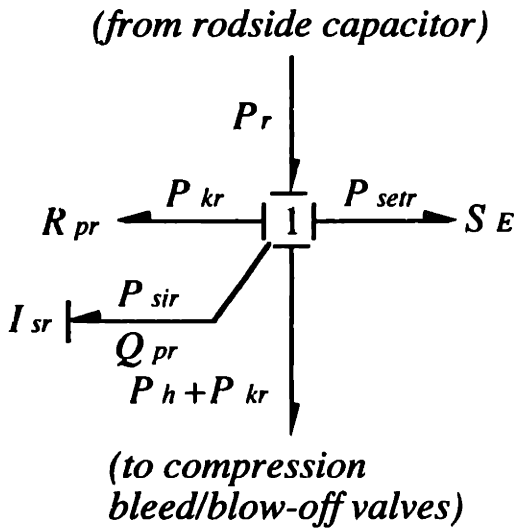

Figure 2.8: Rebound port flow state bond graph

$$\dot{Q}_{pr} = \begin{cases} \frac{P_{air}}{I_{sr}} & \text{for } Q_{pr} > 0 \\ 0 & \text{for } Q_{pr} \leq 0 \end{cases} \tag{2.86}$$

$$\dot{Q}_{pc} = \begin{cases} \frac{P_{aic}}{I_{sc}} & \text{for } Q_{pc} > 0 \\ 0 & \text{for } Q_{pc} \leq 0 \end{cases} \tag{2.87}$$

Limits must be included on the integration process to implement the function of the check valve closure ensuring the flow will not reverse in a channel.

2.6 Valve Equations of State

The pressure relief or blow-off valve is in parallel with the bleed restriction. The flow from the port restriction enters the volume at the end of the restriction which will be referred to as the Y-junction. The bleed orifices are often slots in the blow-off valve seat on the piston. As a result, a closed blow-off valve defines part of the bleed orifice edges, and an open valve defines the contour of the blow-off orifice which also includes the area of the bleed orifices. From the Y-junction, the flow enters either the bleed orifices and/or the blow-off valve restriction if the pressure is high enough.

The region downstream of the port restriction consisting of the Y-junction and

bleed and blow-off restrictions consists of generalized resistors and compliances. The passages are too short to consider inertia effects. The resistive effects are significant due to considerable pressure losses in the fluid flow. A question becomes whether the compliance of the fluid in the Y-junction and the mechanical stiffness of the disk valves and coil springs are important enough to warrant modelling them. The resistive and compliance effects are investigated in the following sections.

2.6.1 Fluid Resistor Analysis of Bleed and Relief Valve Orifices

The bleed and relief valve passages are orifices. An orifice is a sudden restriction of very short length. Orifice flow tends to be turbulent because the transitional Reynolds number for flow through an orifice is extremely low as will be demonstrated. (For example, the transitional Reynolds number for a round orifice is about 9.)

Flow for both the circular and slit orifice cross sections found in shock absorbers will be discussed. Turbulent flow through an orifice will be discussed first because of it is typically more significant for a shock absorber. Howver, laminar flow is important at very slow stroke speeds.

Turbulent Flow

The Reynolds number is usually in the turbulent regime for flow through an orifice. There is very little turbulent mixing upstream of the orifice. Downstream of the orifice the flow expands inefficiently losing kinetic energy due to viscous mixing [17]. Experience shows that the fluid is accelerated in a total distance of about one orifice diameter from a plane upstream of the orifice to the plane where the minimum jet area occurs, known as the vena contracta. The location of the vena contracta is a function of the orifice geometry. The vena contracta for round orifices is approximately one-

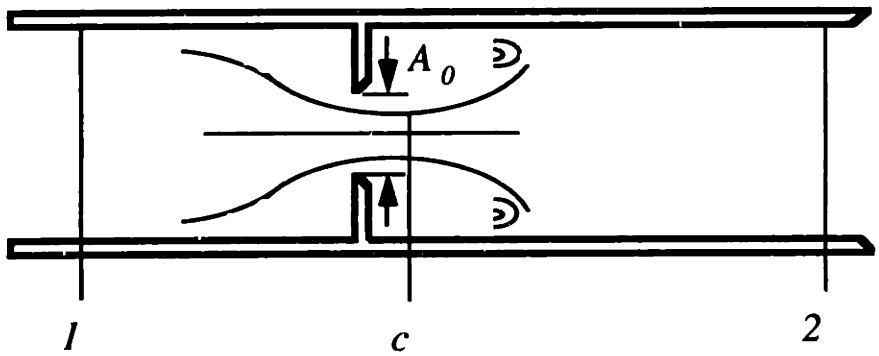

Figure 2.9: Turbulent orifice flow

half orifice diameter downstream of the orifice. An orifice is shorter than this, hence, the analysis and results used for short pipes is invalid for orifices. The contraction coefficient for an orifice is defined as the ratio of the vena contracta area to that of the orifice.

$$C_c = \frac{A_c}{A_o} \tag{2.88}$$

Authors of fluid mechanics texts have by tradition applied Bernoulli's equation and continuity between a plane in the pipe upstream of the orifice and the orifice plane in order to derive the discharge coefficient (or loss coefficient) for an orifice and arrived at the results below.

$$K_o = \frac{\Delta P}{\frac{\rho}{2}\left(\frac{Q}{A_o}\right)^2} = \frac{1}{C_d^2} \tag{2.89}$$

$$C_d = \frac{C_v C_c}{\sqrt{1 - C_c^2\left(\frac{A_o}{A_1}\right)^2}} \tag{2.90}$$

This assumes steady flow (unsteady flow will be discussed later). Application of Bernoulli's equation is justified because the flow upstream of the orifice is very nearly potential flow. Because viscous friction will produce a jet velocity slightly less than given by strict application of Bernoulli's equation, an empirical factor called the

velocity coefficient, for this discrepancy. Most fluid mechanics texts place the velocity coefficent at about 0.98 which would make it negligible for many applications. Note that the velocity coefficient is another way to account for the actual 2-D profile of the flow in a 1-D context similar to the momentum and kinetic energy corrections discussed earlier.

The discharge coefficient, C_d, thus defined is very nearly equal to the contraction coefficient for the case where the upstream area is much larger than the orifice area and turbulent flow, such that, $C_v \simeq 0.98$ and is often approximated by unity. Theoretical and experimental results agree that sharp-edged orifices of any geometry with $A_1 \gg A_o$ have contraction coefficients of approximately 0.611 [17]. Discharge coefficients of $0.60 - 0.65$ are generally accepted for steady, turbulent, liquid flow through sharp-edged orifices of any geometry where the inlet pipe leading to the orifice is large compared to the orifice. As a result, Eqn. (2.89) is typically written in a form similar to Eqn. (2.91) below and referred to as the orifice equation.

$$C_d = \sqrt{\frac{\frac{\rho}{2}\left(\frac{Q}{A_o}\right)^2}{\Delta P}} = 0.611 \tag{2.91}$$

Discharge coefficients for other than sharp-edged inlets are in the range of 0.8 to 0.9 [2].

Laminar Flow

The Reynolds number can become sufficiently low that the flow through an orifice is laminar. This situation is possible for very low pressure drops across the orifice, small orifice openings, or if the temperature is low such that viscosity effects are dominant. Under these circumstances, Eqn. (2.91) is not valid. Attempts to extend the equation to low Reynolds numbers have been made. For example, some researchers found C_d directly proportional to the square root of the Reynolds number at low Reynolds

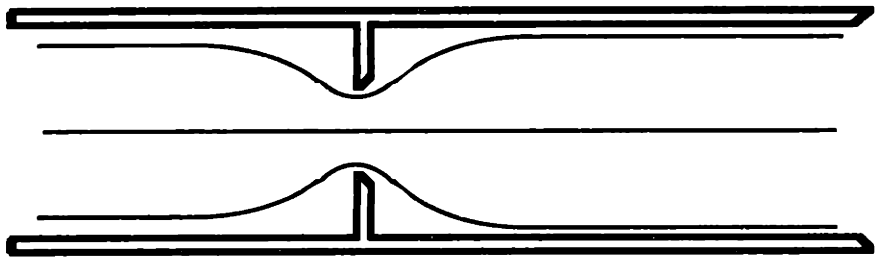

Figure 2.10: Laminar orifice flow

number. The constant of proportionality was referred to as the laminar flow coefficient and is a function of the orifice geometry.

$$C_d^{laminar} = \delta\sqrt{Re} \tag{2.92}$$

where δ is referred to as the laminar flow coefficient.

Merritt [17] cites Wuest, who theoretically determined laminar flow through sharp-edged orifices, and Viersma, who made asymptotic approximations for the discharge coefficient to join the laminar and turbulent regimes. Merritt obtained laminar flow coefficients by comparing Wuest's results with the simplified model of Eqn. (2.92).

$$\delta = \begin{cases} 0.2 & \text{for sharp-edged round orifices} \\ 0.157 & \text{for sharp-edged slit orifices} \end{cases} \tag{2.93}$$

The Reynolds number for slit orifices is calculated using the hydraulic diameter, $D_h = \frac{4A}{P_w}$, where P_w is the wetted parameter, that is, the length of wall in contact with the flowing fluid [7].

Viersma made asymptotic approximations for the discharge coefficient based on Eqn. (2.92) for the laminar flow regime and a constant C_d in the turbulent regime. The constant discharge coefficient in the turbulent regime is often referred to as the ultimate discharge coefficient C_d^{ult}. The transitional Reynolds number would be defined

by the intersection of the two asymptotes. Assuming $C_d^{ult} = 0.611$ and combining the results from Eqn. (2.93) into Eqn. (2.92) yields the following transitional Reynolds numbers,

$$Re_t = \begin{cases} 9.3 & \text{for sharp-edged round orifices} \\ 15.1 & \text{for sharp-edged slit orifices.} \end{cases} \tag{2.94}$$

Unsteady Flow

The analysis of flow through orifices presented thus far does not consider unsteady flow. A generalization of these concepts is required because the flow through shock absorbers is rarely steady. Lang [15] examined this problem by attempting to experimentally correlate unsteady flow discharge coefficients to non-dimensional flow parameters. He proposed using the acceleration number defined in Eqn. (2.95) to characterize the intensity and wave shape of the unsteady flow through shock absorber orifices.

$$Ac = \frac{aL}{\overline{V}} \tag{2.95}$$

Lang's experimental results for triangular velocity inputs through orifices indicated that, although acceleration number had some impact on the unsteady discharge coefficient at very high acceleration numbers, the variation was mainly due to Reynolds number. He concluded the "most significant departure from assuming a constant value of C_d occurs during flow at a low Reynolds number, and this condition occurs only during a small fraction of a cycle." Consequently, Lang used a constant discharge coefficient of 0.7 (representing the ultimate discharge coefficient) in his simulations based on experimental results for flow through the particular orifices of his dualtube shock absorber model. The reason for the difference between the ultimate discharge coefficient which Lang used and the previously discussed values of $0.60 - 0.65$ was that the orifices in his shock absorber were not sharp-edged nor very short. In fact,

the orifices were chamfered with occasional burrs and length to diameter ranges from $0.427 - 0.761$.

The acceleration number was high in magnitude during portions of the cycle where the Reynolds number was low in Lang's testing. Lang did note a difference between the unsteady discharge coefficient for positive and negative acceleration numbers of the same magnitude. This difference was larger at high acceleration numbers, where the velocity was low, and negligible at low acceleration numbers, where the velocities are high.

This observation may not have had so much to do with acceleration number than with the fluid inertia effects. Note the relationship between acceleration number (Eqn. (2.95)) and the non-dimensional inertia pressure ratio (Eqn. (2.83)) defined in Sect. 2.5.3.

$$\frac{P_I}{P_R} = \frac{I\dot{Q}}{R(Q)Q^2} = 2C_d^2 Ac \tag{2.96}$$

The steady flow discharge coefficients will be used in this study assuming the asymptotic approximation of Viersma for low Re. The effect of inertia is included for the port restriction flow as discussed in Sect. 2.5.4 and neglected for the shorter bleed and blow-off restriction.

Orifice Resistor Models

In this study, the effect of laminar and turbulent viscous losses are introduced into the constitutive law for the orifice flow resistors through the asymptotic approximation of Viersma. This results in the following approximation for round orifices

$$C_d = \begin{cases} 0.2\sqrt{Re} & \text{for } Re < 9.3 \\ 0.611 & \text{for } Re \geq 9.3. \end{cases} \tag{2.97}$$

Slit orifices have the approximation,

$$C_d = \begin{cases} 0.157\sqrt{Re} & \text{for } Re < 14.6 \\ 0.611 & \text{for } Re \geq 14.6. \end{cases} \tag{2.98}$$

(Note, using a constant $C_d = C_d^{ult}$ for all orifices would be acceptable for most industrial applications because the flow would tend to be turbulent due to the low transitional Reynolds number.)

Bleed Orifices

The flow through an orifice in conductive causality is a function of the imposed pressure difference across the orifice. The imposed pressure difference for the bleed orifice is P_k. However, bleed orifice flow appears in the state equation of the relief valve. The state variable for the relief valve is the pressure drop across the valve, P_o, as will be demonstrated in Sect. 2.6.3. It is, therefore, preferable to express the bleed flow as a function of P_o ultimately, although it will be expressed in terms of P_k for the moment. Also, the discharge coefficient is a function of Reynolds number which must also be expressed in terms of P_k. A non-dimensional parameter from which C_d can be derived based on the pressure across an orifice is developed below in order to aid in the calculation of the bleed flow.

A non-dimensional pressure loss, which is only a function of Reynolds number, is derived based by combining by Eqns. (2.75) and (2.91).

$$P^{norm} = \frac{P}{\frac{1}{2\rho}\left(\frac{\mu}{D_h}\right)^2} = \left(\frac{Re}{C_d(Re)}\right)^2 \tag{2.99}$$

The value of the "transitional normalized pressure loss" from the expression above and Eqns. (2.97) and (2.98) can be calculated.

$$P_t^{norm} = \begin{cases} 232 & \text{for sharp-edged round orifices} \\ 614 & \text{for sharp-edged slit orifices} \end{cases} \tag{2.100}$$

The bleed discharge coefficient can be expressed in terms of the pressure drop across the orifice, P_k.

$$C_d(P_k^{norm}) = \begin{cases} \delta_k^2 |P_k^{norm}|^{\frac{1}{2}} & \text{for } P_k^{norm} < P_{tk}^{norm} \\ 0.611 & \text{for } P_k^{norm} \geq P_{tk}^{norm} \end{cases} \tag{2.101}$$

The bleed flow can then be written in terms of the imposed pressure differential across the orifice by the constitutive equation for a resistor in conductive causality.

$$Q_k(P_k) = sign(P_k)\left(\frac{|P_k|}{R_k}\right)^{\frac{1}{2}} \tag{2.102}$$

where the resistance value, R_k, for an orifice is by the orifice equation (Eqn. (2.91)),

$$R = \frac{\rho}{2}\frac{1}{A^2}\frac{1}{C_d^2}. \tag{2.103}$$

The sign function in Eqn. (2.102) is required for conductive causality of this resistor because, in theory, the flow can reverse through certain bleed orifices due to the absense of a check valve in the bleed restriction. The amount of the flow which can potentially reverse direction is considered negligible due to the closure of the check valve in the port restriction when the pressure differential drops in the port duct combined with the low compliance of the fluid in the reservoir between the port and bleed restrictions.

The bleed flow can be determined from Eqns. (2.102) and (2.103) by determining (1) whether the flow was laminar or turbulent based on Eqns. (2.99), as compared to Eqn. (2.100), and (2) calculating the appropriate discharge coefficient from Eqns. (2.93) and (2.101) for either round or slit type bleed orifices.

Blow-off Valve Orifices

As in the case of bleed flow, blow-off restriction (orifice) flow appears in the state equation of the relief valve. The pressure difference across the blow-off restriction is simply the pressure drop across the blow-off valve, P_o, which will be used as the state variable. The constitutive equation for the blow-off orifice is, by analogy to that of the bleed orifice,

$$Q_b(P_o) = sign(P_o)\left(\frac{|P_o|}{R_b}\right)^{\frac{1}{2}} \tag{2.104}$$

where R_b is defined by Eqn. (2.103) expressed for the blow-off valve. The "sign" function in this expression is put there for consistency with respect to the bleed flow expression and is really academic because the blow-off valve will close before the flow can reverse direction.

A slit type orifice is assumed for the valve because the opening of the blow-off valve produces an orifice which viewed in the direction of the flow appears as a continuous strip. The flow area of the valve from the circumference, $2\pi a$, and valve deflection, y_b, is

$$A_b = 2\pi a y_b. \tag{2.105}$$

The hydraulic diameter is

$$D_{hb} = \frac{4A_b}{P_{wb}}. \tag{2.106}$$

The additional complication with the blow-off orifice is that the pressure difference across the valve determines the displacement of the valve, which determines the flow area, which in turn effects the pressure difference. The displacement of the valve will be stated in terms of the differential pressure, and the resulting expression for the blow-off valve flow is shown below.

$$Q_b(P_o) = \begin{cases} sign(P_o)\left(\frac{|P_o|}{\frac{\rho}{2}\frac{1}{A_b^2}\frac{1}{C_d^2}}\right)^{\frac{1}{2}} & \text{for } P_o > P_{bo} \\ 0 & \text{for } P_o \leq P_{bo} \end{cases} \tag{2.107}$$

where P_{bo} is the pressure required to open the valve. Note the procedure to calculate the laminar or turbulent flow discharge coefficient is similar to that of the bleed flow.

2.6.2 Compliance Comparisons

A comparison of the complicances may be useful at this point in order to decide what level of analysis is required. These compliances will be compared to compliances which are known to be significant to this problem. The compliances of (1) the fluid in the

Y-junction and (2) the blow-off valve assembly will be compared to the compliances of (3) the fluid on either side of the piston and (4) that of the shock tube cylinder. Because the compliances are from the fluid and mechanical domains, the mechanical compliances are reflected into the fluid domain for comparison purposes in Appendix B.

The resulting comparison indicates that the fluid of the rod and headside volumes and the reflected compliance of the cylinder are largest. The flows into these capacitors are difficult to derive a priori because it depends on the compliance of the other elements as well as that of the element itself. It is assumed that the low compliance of the fluid in the Y-junction makes it the least effective potential energy storage device which eliminates the need for this element.

2.6.3 Integrably Causal Valve Compliance

The blow-off valve compliance relieves the pressure build-up across the bleed orifices by opening the blow-off circuit. The question is whether it is in derivative or integral causality. The problem is handled by considering both alternatives and deciding which makes more physical sense.

Justification for Integral Causality

A simplified valve model is shown in Figure 2.11. The fluid mechanical model consists of a fluid flow source and a volume containing a mass, spring, and three ports. In the simplified valve model, (1) the valve stop, mass, and spring preload are not considered, (2) all the bleed and port flows are lumped together, and (3) the flow is only in one direction. These assumptions are made with no loss of generality to the actual problem. The flow source and pressure sink boundary conditions represent the port flow and rodside (or headside) volume capacitances. Flow enters the top

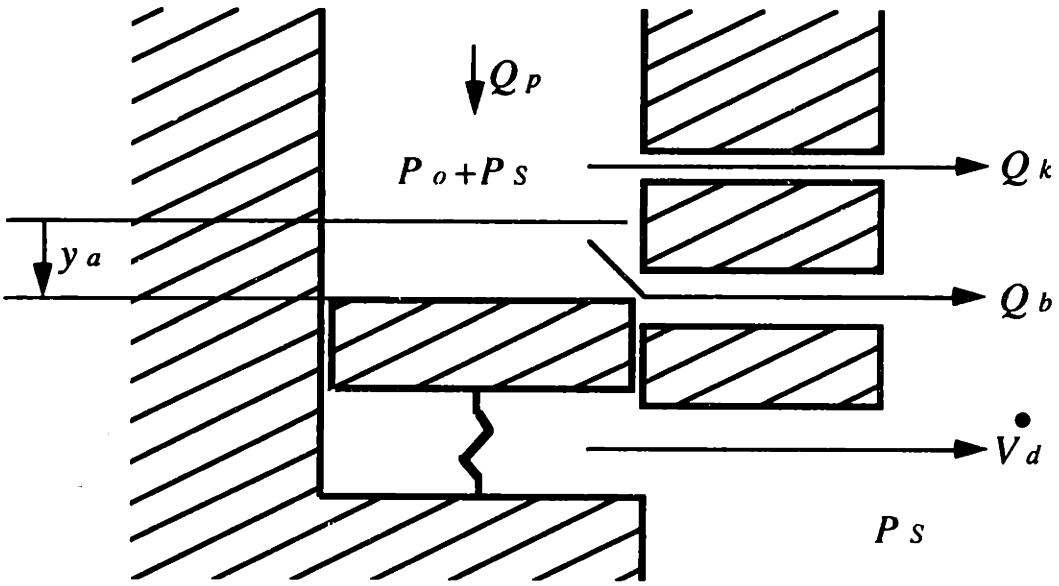

Figure 2.11: Simplified blow-off valve model

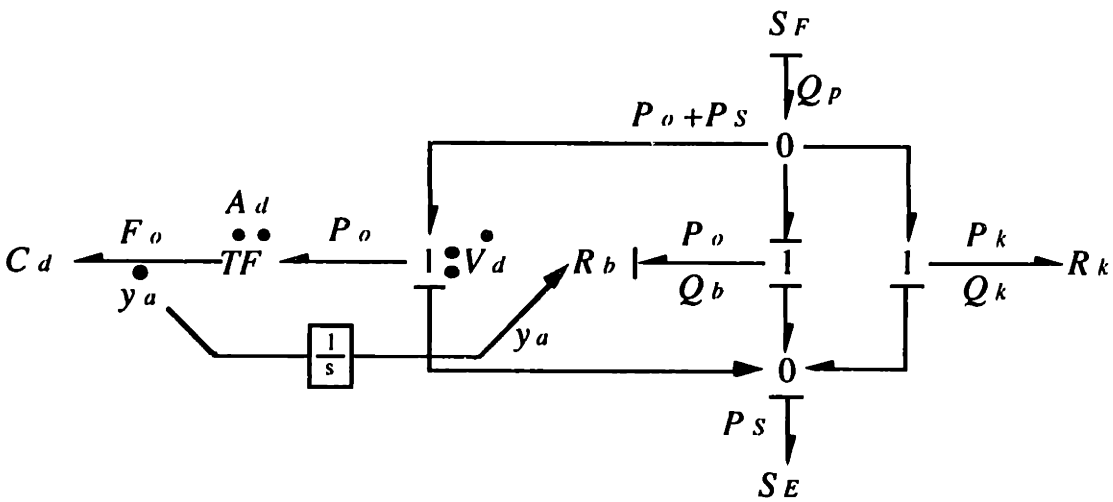

Figure 2.12: Simplified blow-off valve bond graph (incomplete causality)

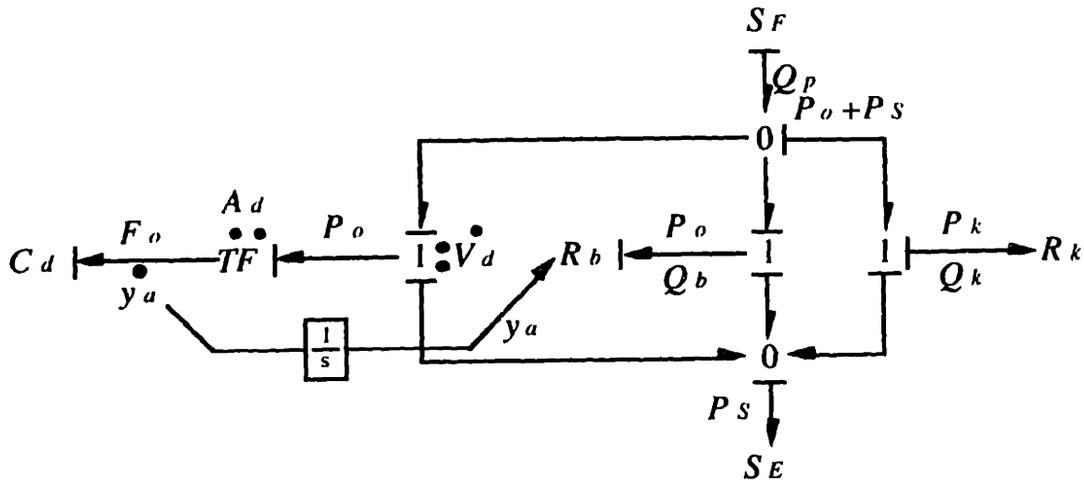

Figure 2.13: Valve capacitor in derivative causality

from the flow source and exits through a smaller port. An undeflected valve closes a second exit port analogous to the blow-off valve. A sufficient increase in the pressure difference across the valve will open the relief port and, in addition, displace the fluid under the valve to the pressure sink.

A bond graph for this simplified model is shown in Figure 2.12 where the causality is carried as far as it can be defined by the flow source and pressure sink boundary conditions and the restriction that a relief valve responds with flow based on the pressure differential applied to it (i.e. Two potential options defining the remainder of the causality exist. Figure 2.13 has the valve compliance in derivative causality, and the Figure 2.14 has the valve in integral causality.

Option 1: Capacitor in Derivative Causality

The remaining causalities may be defined by assuming the valve compliance is in derivative causality. The equations necessary to derive the pressure drop across the valve for option 1 are written directly from the bond graph in terms of causalities.

$$Q_k = Q_p - Q_b - \dot{V}_d \tag{2.108}$$

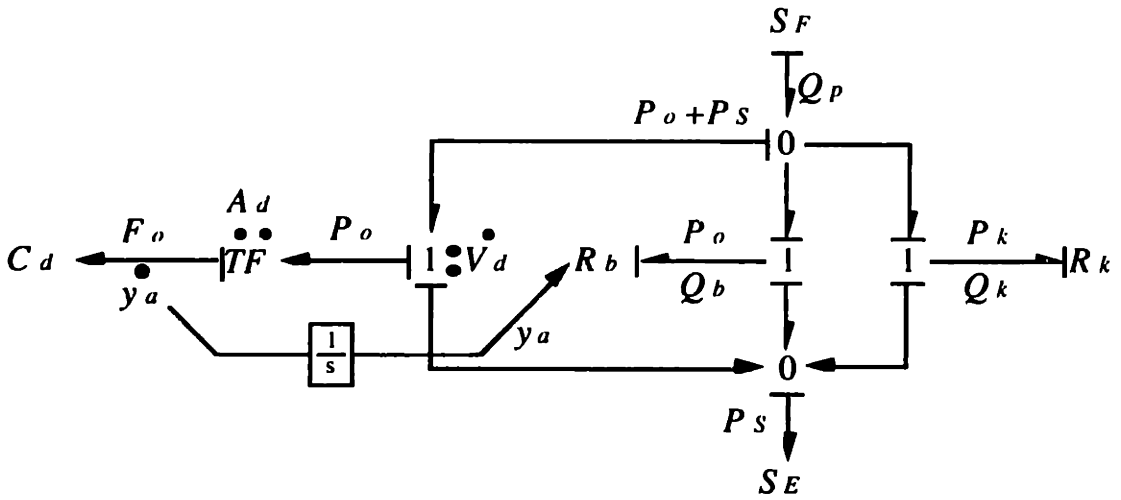

Figure 2.14: Valve capacitor in integral causality

$$P_k = P_o \tag{2.109}$$

$$P_k = R_k Q_k^2 \tag{2.110}$$

$$Q_b = \left(\frac{P_o}{R_b}\right)^{\frac{1}{2}} \tag{2.111}$$

$$\dot{V}_d = A_d \dot{y}_a \tag{2.112}$$

$$F_o = P_o A_d \tag{2.113}$$

$$y_a = C_d F_o \tag{2.114}$$

Combining these equations to get an expression for the pressure drop across the valve results in a non-linear differential equation due to the flow resulting from the displacement of the valve.

$$P_o = R_k \left(Q_p - \left(\frac{P_o}{R_b}\right)^{\frac{1}{2}} - A_d^2 C_d \dot{P}_o \right)^2 \tag{2.115}$$

Consequently, a state related to the valve compliance must exist if the dynamics of relief valve has an effect on flow as in this model.

Option 2: Capacitor in Integral Causality

Several equations with different causalities result assuming the valve compliance is in integral causality.

$$\dot{V}_d = Q_p - Q_b - Q_k \tag{2.116}$$

$$Q_k = \left(\frac{P_k}{R_k}\right)^{\frac{1}{2}} \tag{2.117}$$

$$P_o = \frac{F_o}{A_d} \tag{2.118}$$

$$F_o = \frac{y_a}{C_d} \tag{2.119}$$

Selecting P_o as the state results in the same non-linear differential equation as seen from option 1.

$$\dot{P}_o = \frac{1}{A_d^2 C_d}\left\{Q_p - P_o^{\frac{1}{2}}\left[\left(\frac{1}{R_k}\right)^{\frac{1}{2}} + \left(\frac{1}{R_b}\right)^{\frac{1}{2}}\right]\right\} \tag{2.120}$$

We conclude that if the compliance of the valve is to be considered at all then the capacitor must be in integral causality.

Disk Valve Compliance Model

Having established the necessity for a state arising from the valve compliance from a simplified model, the state equation for the actual system will now be developed. The valve mass and sliding friction between the disks is assumed negligible.

The bond graph for the valve portion of the cross piston fluid circuit is shown in Figure 2.15. The disk valve is preloaded at assembly by an intial deflection, y_{ap}, imposed at the outer valve seat and from a coil spring preload, F_{csp}. The combined preload must be overcome in order for the valve to open. The elastic compliance of the valve is considered even when it is closed, therefore, the boundary conditions change depending on whether the pressure loss across the valve is sufficient to open the valve. The resulting state equation must be piecewise continuous across the region where the valve opens.

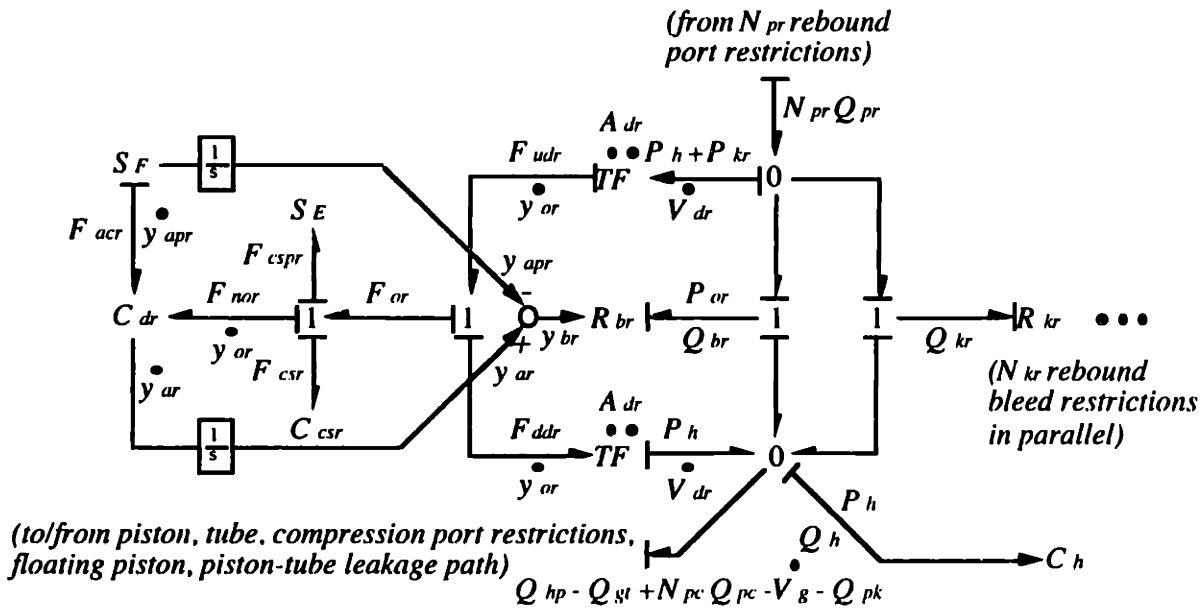

Figure 2.15: Detailed blow-off valve bond graph (including headside volume capacitor)

The compliance of the disk valve assembly is modelled in the bond graph as a C-field. The explicit C-field represents the disk spring stack. Neglected in the analysis is the friction between disks which can produce hysteresis effects in stacks of disk valves. However, the static friction coefficient for steel on steel lubricated with oil is not typically high (in the range of 0.1-0.15 [28]). Also, neglected is damping (resistance effects) on the valve due to fluid viscosity. The one-port capacitor represents the coil spring. The loads acting on the C-field are (1) the net hydraulic load on the valve and (2) the constraint load from the outer valve seat modelled as a flow source. The latter load is only active when the valve is closed. The dynamic model for the valve system is analyzed for both the open and closed positions below.

(i) Open Valve

The state variable for the disk valve capacitor used will be, as in the simplified ex-

ample above, the pressure difference across the valve generated by the valve assembly compliances in response to the port restriction flow input into the volume upstream of the bleed and blow-off restrictions. The pressure difference is given by Eqn. (2.118).

The constitutive equations for the C-field representing the entire valve are required in order to derive the state equation for the valve. Written in terms of their bond graph causality, the constitutive equations are for (1) the force the valve imposes and (2) the deflection of the end of the disk valves, including the initial preload deflection which acts to close the valve. (See Appendix C for the derivation of the disk valve compliance model from the disk stiffnesses.)

$$F_o = \left(\frac{1}{C_{oo}} + \frac{1}{C_{cs}}\right) y_o + F_{csp} \tag{2.121}$$

$$y_a = \left(\frac{C_{ao}}{C_{oo}}\right)\left(\frac{1}{C_{oo}} + \frac{1}{C_{cs}}\right)(F_o - F_{csp}) \tag{2.122}$$

Equation (2.121) will be used to develop the state equation, and Eqn. (2.122) will be used to calculate the valve opening which is needed to solve for the pressure difference across the valve. The actual valve opening, accounting for the preload deflection, y_{ap}, is really

$$y_b = y_a - y_{ap}. \tag{2.123}$$

Noting $P_k = P_o$, the equation for the force is put in terms of the states for the system by substitution of (1) the constitutive equation of the valve transformer between the fluid and mechanical domains, (2) the flow junction (continuity) equation for the y-junction volume, and (3, 4) the constitutive equations of the bleed and blow-off restriction resistors.

$$\dot{y}_o = \frac{\dot{V}_d}{A_d} \tag{2.124}$$

$$\dot{V}_d = N_p Q_p - Q_b - N_k Q_k \tag{2.125}$$

$$Q_k = \left(\frac{P_o}{R_k}\right)^{\frac{1}{2}} \tag{2.126}$$

$$Q_b = \left(\frac{P_o}{R_b(y_b)}\right)^{\frac{1}{2}} \tag{2.127}$$

The flows, Q_k and Q_b, have certain restrictions based on the pressure difference which for simplicity will be ignored until the final state equation is developed.

In the valve designs investigated in this study, the edge of the blow-off valve when it is closed is part of the edge of the bleed of restriction. Consequently, the bleed flow in effect becomes part of the blow-off flow when the blow-off valve opens.

(ii) Closed Valve

When the valve is closed, the deflection at the disk opening is equal to the preload deflection. The constitutive equations are calculated by superposition.

$$F_o = \left(\frac{C_{aa}}{C_{aa}C_{oo} - C_{ao}C_{oa}} + \frac{1}{C_{cs}}\right) y_o - \left(\frac{C_{oa}}{C_{aa}C_{oo} - C_{ao}C_{oa}}\right) y_{ap} + F_{csp} \tag{2.128}$$

$$F_a = \frac{-1}{C_{aa}C_{oo} - C_{ao}C_{oa}} (C_{ao}y_o - C_{oo}y_{ap}) \tag{2.129}$$

Note that the equation for the constraint load at the edge of the disk valve replaces the equation for the valve end deflection. This is a result of the causality (boundary condition) change. When the valve is closed, the end defection is imposed by the outer valve seat thereby imposing zero flow.

The load, F_o, must be piecewise continuous across the point where the valve opens. The end load, F_o, is zero at the "blow-off" condition. Setting $F_o = 0$ in Eqn. (2.128) and solving for y_o at the blow-off condition yields

$$y_{obo} = \frac{C_{oo}}{C_{ao}} y_{ap}. \tag{2.130}$$

Substituting Eqn. (2.130) into either Eqn. (2.121) or (2.128) results in the blow-off condition force.

$$F_{obo} = \left(\frac{1}{C_{oo}} + \frac{1}{C_{cs}}\right) \frac{C_{oo}}{C_{ao}} y_{ap} + F_{csp} \tag{2.131}$$

$$= \frac{1}{C_{cs}} \frac{C_{oo}}{C_{ao}} y_{ap} + F_{csp} + \frac{1}{C_{ao}} y_{ap} \tag{2.132}$$

In Eqn. (2.132) the first two terms represent the load at the hydraulic line of action (position "o") required to offset the spring preload. The third term is the additional load required to offset the "defection preload" and bring the valve to the blow-off condition.

2.6.4 Valve State Equation

All that remains is to produce a state equation in terms of the states and inputs of the system from the expressions derived in the preceding sections. The state variable selected to represent the compliance of the disk valve will be the pressure drop across the valve rather than resistive force of the valve. This choice is made because the pressure drop represents a more meaningful parameter and is consistent with the flow variables involved in the state equation.

2.6.5 Reflection into Fluid Domain

The state equation is then written by differentiation of the pressure difference across the valve (Eqn. (2.118)) and by substituting Eqn. (2.121) if the valve is open or Eqn. (2.128) if the valve is closed. As a result, Eqns. (2.122) – (2.127) are required if the valve is open. Equations (2.124), (2.125) (with $Q_b = 0$), and (2.126) are used if the valve is closed. The resulting state equation is Eqn. (2.133).

$$\dot{P}_o = \begin{cases} \frac{1}{C_{bo}A_d^2}\left[N_pQ_p - sign(P_o)|P_o|^{\frac{1}{2}}\left(N_k\left(\frac{1}{R_k}\right)^{\frac{1}{2}} + \left(\frac{1}{R_b(P_o)}\right)^{\frac{1}{2}}\right)\right] & \text{for } P_o > P_{bo} \\ \frac{1}{C_{bc}A_d^2}\left[N_pQ_p - sign(P_o)|P_o|^{\frac{1}{2}}N_k\left(\frac{1}{R_k}\right)^{\frac{1}{2}}\right] & \text{for } 0 < P_o \leq P_{bo} \end{cases} \tag{2.133}$$

Note, that if the bleed orifice edges are defined by the blow-off valve when it is closed, as for slot bleed restrictions cut in the blow-off valve seat, then the bleed flow is effectively zero when the valve is open and the area of the blow-off orifice includes that of the bleed restrictions. P_{bo} is referred to as the "blow-off" pressure, or the

pressure required to open the valve and is derived from Eqn. (2.131).

$$P_{obo} = \frac{1}{A_d}\left[\left(\frac{1}{C_{oo}} + \frac{1}{C_{cs}}\right)\frac{C_{oo}}{C_{ao}}y_{ap} + F_{csp}\right] \tag{2.134}$$

The effective compliances C_{bo} and C_{bc} for the valve in the open and closed configurations are written below.

$$C_{bo} = \frac{1}{C_{oo}} + \frac{1}{C_{cs}} \tag{2.135}$$

$$C_{bc} = \frac{C_{aa}}{C_{aa}C_{oo} - C_{ao}C_{oa}} + \frac{1}{C_{cs}} \tag{2.136}$$

The orifice resistances are calculated from Eqn. (2.103) and the methods outlined in the sections on the bleed and blow-off valve orifices.

The A_d^2 in Eqn. (2.133) is a result of the "reflection," in bond graph terminology, of the mechanical compliance of the disk valves and coil spring into the fluid domain Eqn. (2.118). The result is an equivalent fluid compliance due to the mechanical valve assembly stiffness. The equivalent compliance for a capacitor reflected across a tranformer from the mechanical to the fluid domain is of the form

$$C_{domain1} = C_{domain2}A^2. \tag{2.137}$$

2.7 Floating Piston State

The floating piston inertia may be considered to be in integral causality. The forces acting on the piston are the weight of the piston, the loads from the pressures in the nitrogen gas chamber and the headside capacitor, and the friction force at the interface between the floating piston and the cylinder. The model of the friction force is developed below and integrated into the overall subsystem of the floating piston.

2.7.1 Friction Models

Of the loads acting on the piston, the friction force is by far the most complex to model accurately. The friction characteristic is not purely viscous, as modelled at the interface between the shock piston and tube, nor is it dry (a.k.a. Coulomb) friction. The requirement to have a positive seal to prevent leakage flow results in high friction loads. Therefore, the seal will tend to prevent a significant build-up of an oil film at the interface. The fact that there will be some oil at the interface will mean that the friction coefficient should account for the added lubricity.

Many friction models are possible depending on the relative contribution of the viscous and dry friction phenomena. It is assumed that the seal is very at scraping the oil and prevents the type of oil film required for viscous damping. This assumption alone limits us to the hundreds of dry friction models developed by researchers over the past 500 years! The materials in contact and their surface state, the interface pressure, the contact time, and the rate of load application all effect the coefficient of friction. A summary of the coefficient of friction models proposed by reseachers was made by Kragelsky, Dobychin, and Kombalov including models proposed by these same authors [13]. A few of the laws cited in this reference will be discussed here.

Leonardo da Vinci in 1508 proposed the first law of surface friction.

$$F_f = fN \tag{2.138}$$

where the coefficient of friction, f, was assumed to be a constant value of 0.25. Hence, this defined the coefficient of sliding dry friction as the ratio of the resistive friction load to the normal load.

Coulomb in 1778 proposed an alternative law of surface friction given as

$$F_f = BN + A \tag{2.139}$$

where A and B are constants. By this law, the coefficient of sliding friction was a two term function where one term was dependent on the contact force.

$$f = \frac{A}{N} + B \tag{2.140}$$

The German scientist Franke working with empirical data from other researchers observed that the friction force was a function of velocity in 1882. He proposed

$$f = f_o e^{-cv} \tag{2.141}$$

where f_o is the coefficient of static friction, c is a constant, and v is the sliding speed.

Kragelsky, Dobychin, and Kombalov studied friction for sliding speeds of 0.0004 - 25 m/s and contact pressures of 8 - 17,000 Pa. The following two results were observed.

(i) The coefficient of friction passes through a maximum with increasing speed.

(ii) The maximum coefficient of friction occurs at lower sliding speeds as the interface pressure increases.

From these results, they proposed the following friction law

$$F_f = (a + bv)e^{-cv} + d \tag{2.142}$$

where a, b, c, and d are coefficients. The first term, as compared to the law proposed by Franke, provides additional degrees of freedom by which to match observations made from test data. The coefficient of friction by this method is then

$$f = \frac{(a + bv)e^{-cv} + d}{N}. \tag{2.143}$$

2.7.2 Seal Stiction-Dynamic Friction Model

Several assumptions must be made in order to obtain a model for the floating piston seal friction model without running many experiments. Assuming the load between

the contact surfaces is high enough that the maximum sliding friction occurs on the ver[illegible] of motion, then the maximum coefficient of sliding friction is equal to the static coefficient of friction. Further, assuming the coeffient of friction is fairl[illegible] constant at higher speeds produces the relationship derived from Eqn. (2.143)

$$f = (f_o - f_d)e^{-cv} + f_d \tag{2.144}$$

where f_d is the kinetic coefficient of friction for a given high velocity condition approached asymptotically. This is equivalent to asssuming

$$a = (f_o - f_d)N \tag{2.145}$$

$$b = 0 \tag{2.146}$$

$$d = f_d N \tag{2.147}$$

in the method of Kragelsky, Dobychin, and Kombalov. This leaves only one coefficient to derive. The method used in this thesis to derive the coefficient c is to assume that friction factor is within 1% of the dynamic friction coefficient at the velocity quoted for the dynamic coefficient. It is assumed the materials are oil wetted floating piston seal material on the tube material. It is assumed the O-ring is made of a rubberlike material and the tube material is typically steel. The static friction coefficient for rubber on steel is approximately $1 - 4$ [4]. The algothym is numerically more stable when the friction is large and the transition between static and dynamic friction factors is not steep. This will be discussed further in the results section.

2.7.3 Floating Piston Model

A simplified bond graph for the floating piston is shown in Figure 2.16. The weight of the floating piston and tube relative motion are ignored for the moment with no loss of generality. The bond graph is equivalent to that of a mass pushed on a flat

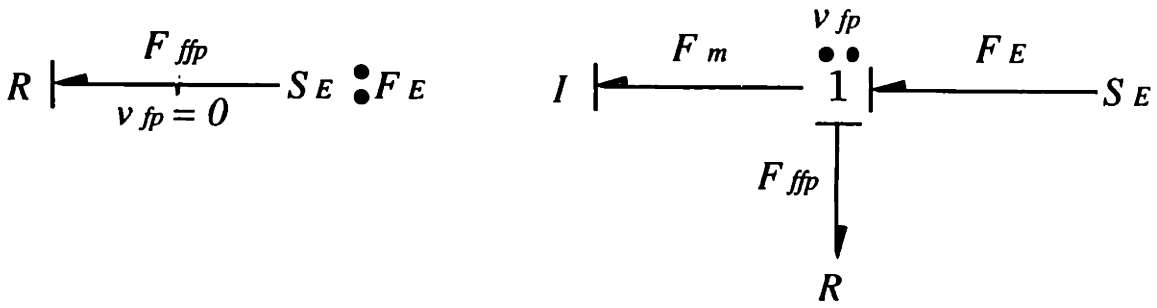

Figure 2.16: Simplified floating piston bond graph (1-port resistor)

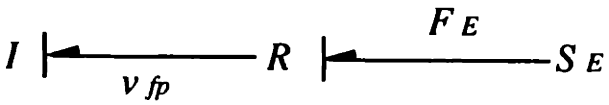

Figure 2.17: Simplified floating piston bond graph (R-field)

surface. The friction force is given by

$$F_{ffp} = \begin{cases} F_E \leq f_o N & \text{for } v_{fp} = 0 \\ f_{fp} N & \text{for } |v_{fp}| > 0 \end{cases} \tag{2.148}$$

The friction force on the mass depends on the applied loads up to the time the static friction force (stiction) is overcome. The input to the resistor is only the applied load from the nitrogen gas and headside compliances (represented by the effort source) while the piston has zero acceleration. When the applied load is sufficient to overcome the static friction, the piston begins to move and the input to the resistor is the velocity (flow) and the output is the effort for that flow.

A more appropriate representation of the bond graph is Figure 2.17. The stiction-dynamic friction resistor is modelled as an explicit R-field with the inputs as the flow of the inertia and the force of the effort source. The constitutive law of the resistor

is then

$$F_{fp}(v_{fp}, F_E) = \begin{cases} F_E \leq f_o N & \text{for } v_{fp} = 0 \\ sign(v_{fp}) f_{fp} N & \text{for } |v_{fp}| > 0 \end{cases} \tag{2.149}$$

where f_{fp} is given by a form of Eqn. (2.144) shown below.

$$f_{fp} = (f_o - f_d)e^{-c|v_{fp}|} + f_d \tag{2.150}$$

Friction models which include stiction are subject to numerical instabilitites because often the numerical algorithm used is not robust enough to handle the sudden jumps in force for small changes in velocity. Initial stiction models used in this study were not exceptions. The first stiction model used was one that employed a step change from the static friction coefficient to the significantly smaller kinetic friction coefficient at the instant of "breakaway." Although the MATLAB integration routine was robust enough to handle this discontinuity in a stand alone model, the routine went unstable when the stiction-dynamic friction model was integrated with the overall shock absorber model. This discontinuity in the multi-degree of freedom model propagated more discontinuities in the state equations than the algorithm could handle. The more complex friction model which models the actual interface more accurately has the added benefit of making the numerical simulation more stable.

2.7.4 Floating Piston State Equation

Figure 2.18 is a bond graph representation of the floating piston subsystem-based on an inertial frame of reference. The flow across the transformer in the fluid domain is the volume flowrate of the nitrogen chamber. This flowrate is due to the motion of the floating piston relative to the tube. It is more convenient to formulate the state equation in terms of the floating piston velocity relative to the piston tube because the relative velocity defines the friction at the interface. Therefore, the state variable

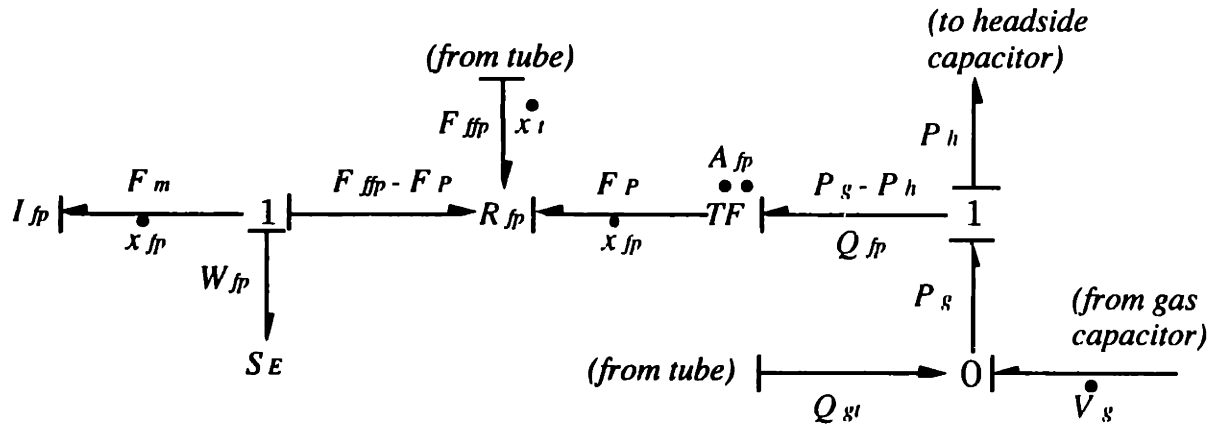

Figure 2.18: Floating piston bond graph based on Inertial frame

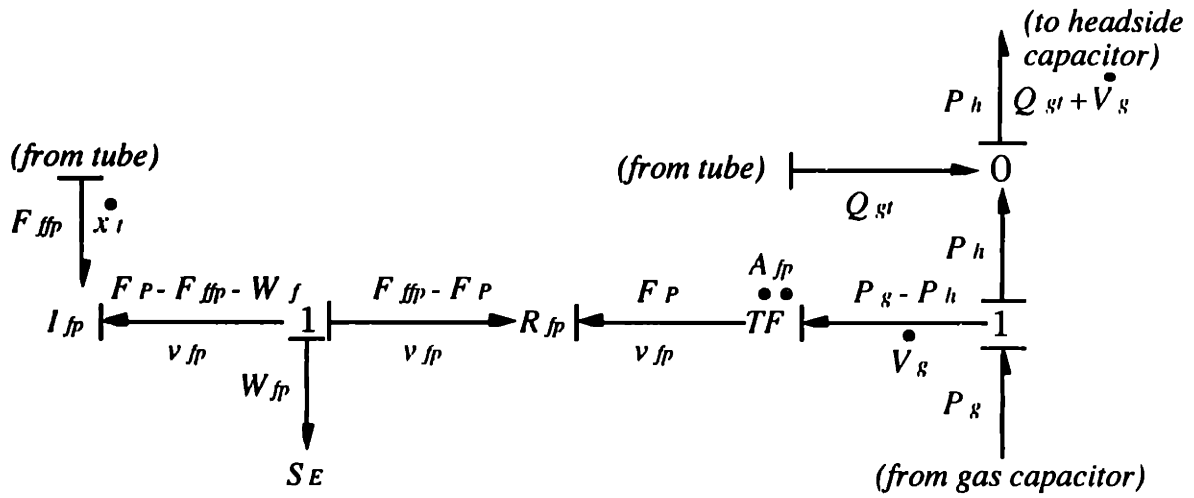

Figure 2.19: Floating piston bond graph based on relative frame

selected was this relative velocity so that it could be used directly for the resistive element constitutive law.

In Figure 2.19, the one port inertia is replaced by an inertia field with one port

in derivative causality and the other in integral causality. The state equation for the inertia in terms of the relative velocity and the friction force are

$$\dot{v}_{fp} = \frac{1}{m_{fp}}(F_P - F_{ffp} - W_{fp} - m_{fp}\ddot{x}_t) \tag{2.151}$$

$$F_{ffp} = \begin{cases} F_P - W_{fp} - m_{fp}(\ddot{x}_t + \dot{v}_{fp}) \leq f_o N & \text{for } v_{fp} = 0 \\ sign(v_{fp}) f_{fp} N & \text{for } |v_{fp}| > 0 \end{cases} \tag{2.152}$$

where f_{fp} is given by Eqn. (2.150) and F_P is given by the transformer constitutive equation.

$$F_P = A_{fp}(P_g - P_h) \tag{2.153}$$

2.8 Gas State

The nitrogen gas chamber produces a state of the system. Flow is defined by the floating piston, and the gas produces an effort acting on the floating piston. The methodology for the model of the nitrogen gas is developed in this section, as is the resulting dynamic state equation.

2.8.1 Thermodynamic Accumulator

Modelling of the nitrogen gas enclosed by the floating piston will be based on the thermodynamic accumulator [11] derived from a control volume formulation. The themodynamic accumulator is a three port C-field which handles the convective terms of the energy and momentum equations for compressible gas dynamics as derived from the Eulerian frame (control volume) of reference. This formulation will consider the ideal gas law which is a nonlinear temperature dependent equation of state between pressure and flow necessary to adequately represent the compressible nitrogen gas.

A bond graph of the thermodynamic accumulator is shown in Figure 2.20. One bond on the thermodynamic accumulator considers the power variables, pressure and flowrate, of fluid dynamic systems. The other two bonds are considered pseudo bonds

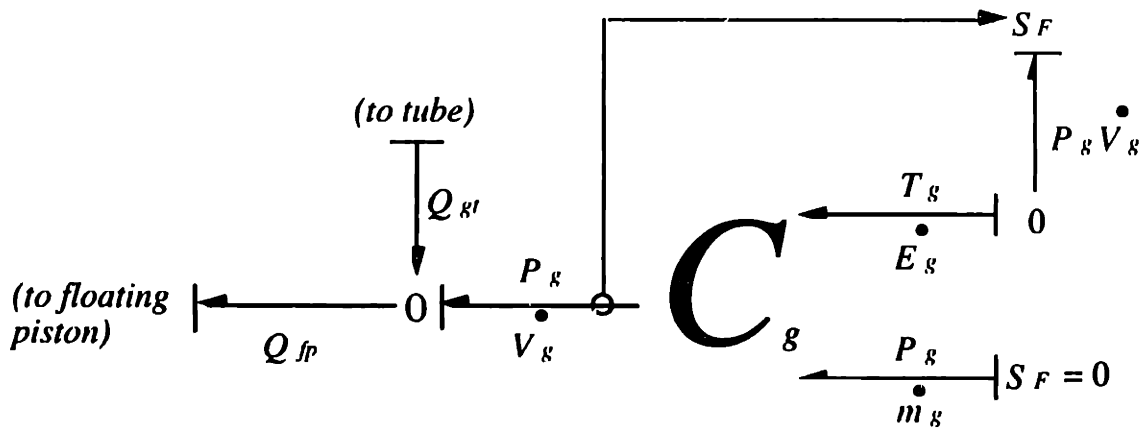

Figure 2.20: Thermodynamic accumulator bond graph

because the product of their effort and flow variables is not power. One of these pseudo bonds handles the energy flow considerations of the first law of thermodynamics for the control volume. The second pseudo bond represents mass flow to and from the accumulator.

Assuming the control volume is closed and that the heat transfer is negligible when compared to the work of the piston, the equations for the three bonds express (1) the constitutive law of the floating piston transformer, (2) continuity, and (3) the first law of thermodynamics.

$$\dot{V}_g = A_{fp} v_{fp} \tag{2.154}$$

$$\dot{m}_g = 0 \tag{2.155}$$

$$\dot{E}_g = -P_g \dot{V}_g \tag{2.156}$$

The constitutive equations for the C-field are derived from the definition of the internal energy of the control volume and the ideal gas law.

$$T_g = \frac{E_g}{C_{vg} m_g} \tag{2.157}$$

$$P_g = \frac{m_g R_g T_g}{V_g} \tag{2.158}$$

2.8.2 Gas State Equation

We note that the input to the C-field is defined by Eqn. (2.154). Differentiating Eqn. (2.157) and using Eqn. (2.156) and Eqn. (2.158) results in Eqn. (2.159) which is a dynamic state equation.

$$\dot{T}_g = \frac{-R_g}{C_{vg}} \frac{\dot{V}_g}{V_g} T_g \tag{2.159}$$

Equation (2.159) along with Eqn. (2.154) describing the prescribed input produces a system which can be intergrated numerically. However, an analytical solution for Eqn. (2.159) exists.

$$T_g V_g^{\frac{-R_g}{C_{vg}}} = const. \tag{2.160}$$

This solution can be written as

$$\frac{T_{g(i+1)}}{T_{g(i)}} = \left(\frac{V_{g(i)}}{V_{g(i+1)}} \right)^{\frac{-R_g}{C_{vg}}} . \tag{2.161}$$

Equation (2.158) and the relationships

$$R_g = C_p - C_v \tag{2.162}$$

$$\gamma \equiv \frac{C_p}{C_v} \tag{2.163}$$

are substituted into Eqn. (2.161) resulting in

$$\frac{P_{g(i+1)}}{P_{g(i)}} = \left(\frac{V_{g(i)}}{V_{g(i+1)}} \right)^{\gamma} \tag{2.164}$$

which is the relationship for an isentropic process.

The output of the thermodynamic accumulator is the pressure of the gas. This pressure which interacts with the rest of the system is given by Eqn. (2.164). Eqn. (2.164) is an expression for the ideal gas law assuming an isentropic process. The relationship responsible for the integral causality of the thermodynamic accumulator and, therefore, the dynamic state equation is Eqn. (2.154). Equation (2.154) is referred to here as an "auxiliary equation" which must be integrated before Eqn. (2.164) is used to calculate the actual pressure output of the accumulator.

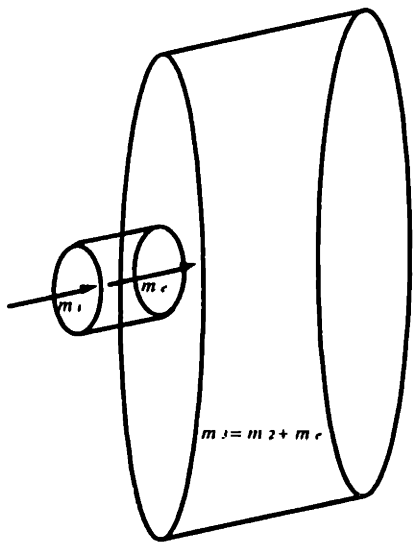

Figure 2.21: Thermodynamic control volume of cylinder capacitor

2.9 Temperature Effects

The temperature increase due to viscous losses is examined through an example. The example is made with the following assumptions for the shock absorber.

(i) Step input into shock of given velocity (i.e.: steady flow).

(ii) All fluid flow passes through bleed restrictions.

(iii) Equal flow area on either side of the orifices.

(iv) No heat transfer to or from fluid.

(v) Negligible potential energy change.

(vi) No work on the flow through the orifice.

(vii) State of fluid in cylinder varies with time but not spatially.

The first law for the flow through an orifice is

$$\Delta Q_{cvl} + m_i \left(h_i + \frac{z_i^2}{2} \right) = \Delta E_{cvl} + m_e \left(h_e + \frac{\overline{V}_e^2}{2} \right) + \Delta W_{cvl} \tag{2.165}$$

Based the first six assumptions above, the increase in temperature across the orifice

reduces to

$$\Delta T_{orifice} = \frac{1}{\rho C_p} \Delta P_{orifice}. \tag{2.166}$$

The equations for the first law and continuity applied to the second control volume (the cylinder volume) are

$$\Delta Q_{cv1} + m_e \left(h_e + \frac{\overline{V}_e^2}{2} \right) = \Delta E_{cv2} + \Delta W_{cv2} \tag{2.167}$$

$$m_3 = m_2 + m_e \tag{2.168}$$

based on assumptions 4, 5, and 7. The temperature increase of the flow into the volume is

$$\Delta T_{cv2} = \Delta T_2 + \frac{m_e}{m_2 + m_e} \frac{1}{C_p} \left[C_v \Delta T + \frac{P}{\rho} + \frac{1}{2} \left(\frac{Q_k}{A_k} \right)^2 - \frac{\Delta W_{cv2}}{m_e} \right]. \tag{2.169}$$

Assuming 7 bleed restrictions each with an area $7.22 \times 10^{-7} m^2$, an applied pressure of 2.8×10^6Pa, and the following parameters result in 0.05K increase in temperature of fluid in volume in 0.1s.

$$\begin{aligned} A_{piston} &= 0.001297 m^2 \\ v_{piston} &= 0.127 \frac{m}{s} \text{ for } 0.1 sec \\ V_{initial} &= 0.324 \times 10^{-3} m^3 \\ C_d &= 0.611 \\ C_p &= 2092 \frac{J}{kg - K} \\ C_v &= 2011 \frac{J}{kg - K} \\ \rho &= 870 \frac{kg}{m^3} \\ T_2 &= 301 K (28C) \end{aligned}$$

This does not account for conduction to the metal in the tube and convection from the shock body to outside atmosphere. Therefore, the heat energy generated over this

short instance is small compared to the work of the piston on the fluid. Consequently, the heat transfer over short durations has a negligible effect on the force output of the shock absorber. However, the effect of temperature on fluid viscosity is important, particularly at low Reynolds numbers were flow tends toward the laminar regime. It is, therefore, desirable to have most of the flow in shock absorbers to be turbulent in order to reduce the temperature dependency.

2.10 Force Output

The output relationship for the shock absorber is derived from the states of the shock absorber. The loads acting on the piston define the output (effort) of the shock absorber. The case where the shock absorber is installed in an automotive suspension is different than the case where the shock is installed in a vibration machine. Each case is considered separately below.

2.10.1 Input to Shock Absorber

The input to the shock absorber model is made through the tube for a conventionally mounted monotube shock absorber. Neglecting the compliance of the tire and the shock mounts, the input to the system is the flow from the combined effects of the rod surface displacement and the forward motion of the car. As a result, the inertia of the tube does not create a state (see Figure 2.22). The force on the piston end of the shock absorber will be considered as the output.

2.10.2 Piston State for Automotive Installed Case

The piston installed in an automotive suspension system creates two states. One state is due to the piston mass, and the second is due to the automotive suspension system. The input to the tube acts on the piston through the states of the shock

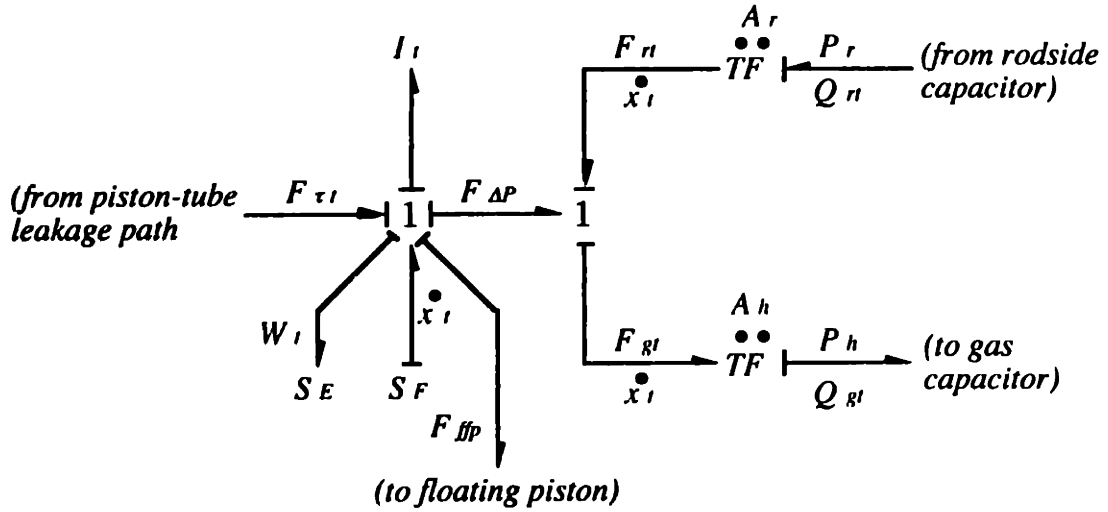

Figure 2.22: Shock absorber tube bond graph

absorber (see Figure 2.23).

The piston will be considered part of the automobile which is the sprung mass in this analysis. The compliance of the tire and of the rubber mounts attaching the shock absorber to the car are not considered. The friction between the rod guide and piston rod is also neglected assuming there is clearance between the surfaces. The effort junction of the piston in this case defines the flow of the shock piston and portion of the car which the shock suspends (often considered $\frac{1}{4}$ of the car mass).

$$\frac{d\dot{x}_p}{dt} = \frac{1}{m_p}[-F_s - W_p - P_{atm}A_{rod} - P_rA_r + P_hA_h + F_{rp}] \tag{2.170}$$

$$\frac{dx_p}{dt} = \dot{x}_p \tag{2.171}$$

$$\frac{dF_s}{dt} = \frac{1}{C_s}(\dot{x}_p - \dot{x}_t) \tag{2.172}$$

where W_p includes the weight of the piston, piston rod, and, most importantly, the portion of the car lumped with the piston. Note, the shear force is a function of states and the input. Friction between the rod and rod guide has been neglected.

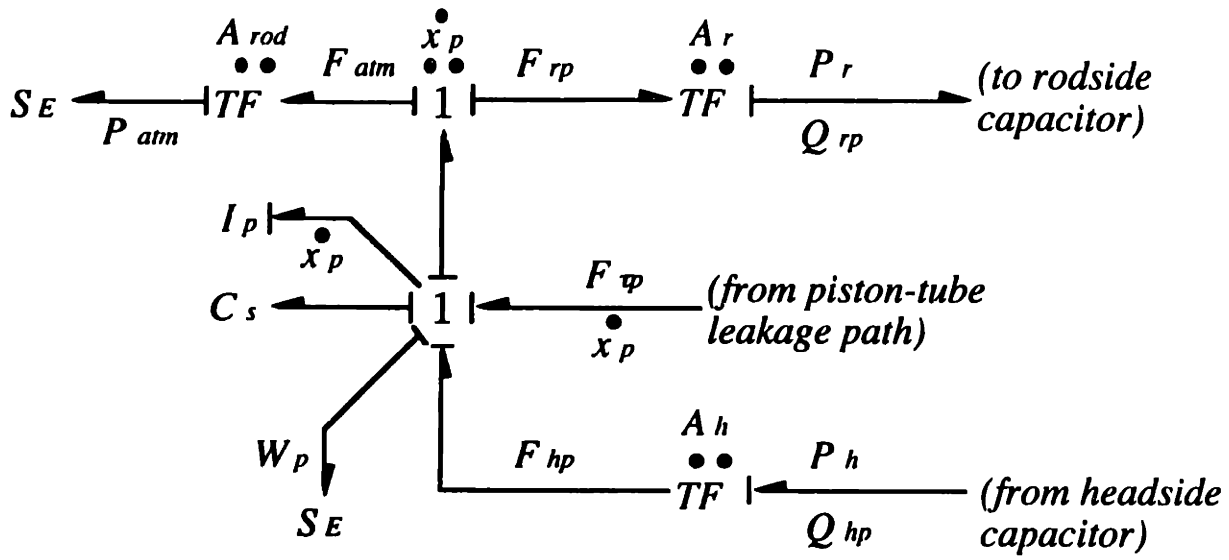

Figure 2.23: Piston state bond graph for automotive installed case

2.10.3 Output Equation for Test Machine Installation

The piston installed in a vibration test machine does not result in additional states because the piston velocity is fixed at zero while the tube portion of the shock absorber is stroked. The effort junction of the piston in this case defines the output as the effort of the piston on the rig. The sign convention selected establishes positive effort as a tensile force on the shock absorber (see Figure 2.24)

$$F_p = W_p + P_{atm}A_{rod} + P_rA_r - P_hA_h - F_{rp}. \tag{2.173}$$

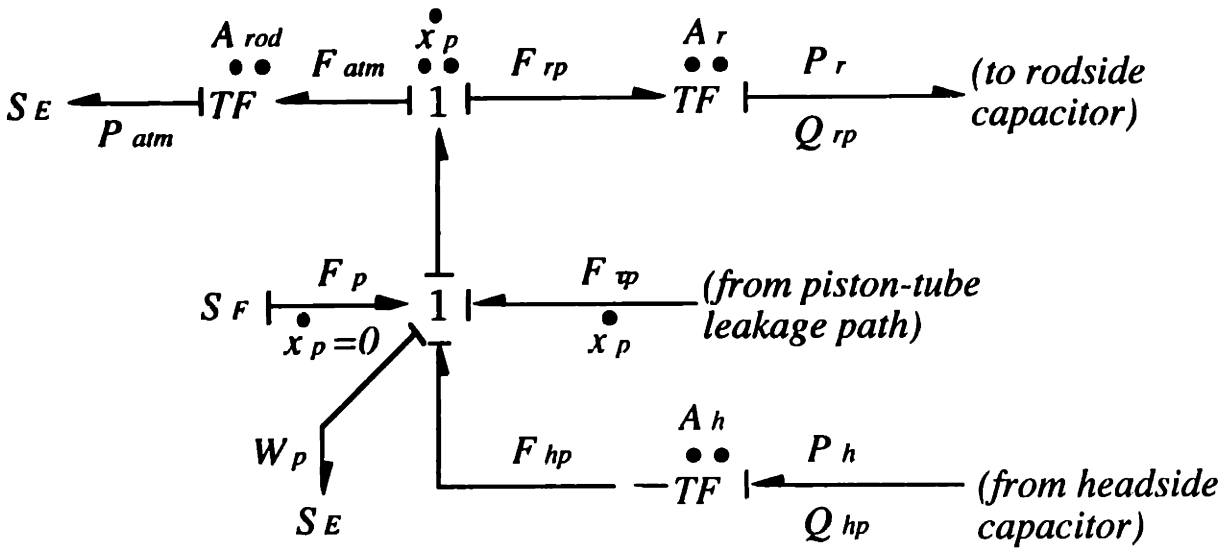

Figure 2.24: Piston effort bond graph for test machine installation

Chapter 3

Simulation Results

3.1 Verification of Shock Absorber Valving Model

The most significant component defining a shock absorber's performance is the valving design. The compressibility of the hydraulic fluid determines the pressure variation within the fluid volumes on either side of the piston as a function of the fluid flow into and out of the volume. The valving determines the force output of the shock absorber because the static pressure losses across the piston are a function of the characteristics of the orifice and valve designs within the piston.

A simulation of a valve design for which the characteristics are known was performed in order to validate the model derived for the piston valving including the port and bleed orifices. Data for a monotube shock absorber was not available at the time of this writing. However, experimental data was made available for a Monroe dualtube shock design. This dualtube design was modelled as a monotube for comparison purposes. Some of the more important parameters used for this analysis are summarized in Table 3.1.

Both monotubes and dualtubes in automotive applications have unequal piston areas on the rod and headsides. When either design is stroked, the equivalent flow from the swept volume due to the rod must in large part go to a third reservoir because the oil is "mostly" incompressible. The ride from a shock with hydraulic fluid which did not have a third reservoir would be extremely stiff and would tend to be underdamped due to the compressiblity of the fluid, and the high transient

Shock Parameter	Value	Units
Shock Absorber Tube Diameter	1.75	in
Check Valve Preload	0.025	MPa
Port Restriction $\frac{L}{D}$	1.45	DMSL
Port Restriction Quantity	8	DMSL
Orifice Discharge Coefficients	0.611	DMSL
Bleed Slot Quantity	7	DMSL
Blow-off Valve Preload	0.62	MPa

Table 3.1: Significant dualtube simulation parameters

pressures would tend to destroy the seal components.

The form the third reservoir takes is the principle difference between a monotube and a dualtube shock design. The monotube design has a gas-filled reservoir which is pressurized often on the order of 20bar. This high pressure produces a force by the shock which is always present and would tend to extend the shock. The force at an equilibrium condition is the pressure of the headside volume acting on the eq ivalent area of the piston rod. This force is related to the piston displacement. In order to correctly compare the valve characteristics of monotube and dualtube shock designs, only that portion of the total force of the monotube related to the piston motion was compared to the dualtube sinusoidal test results. The force due to the headside pressure acting on the rod area must be subtracted from the total monotube force. In addition, only the maximum forces obtained during a cycle at a given frequency were compared because the transient effects would tend to be different in both types of designs due to different component behavoirs. The peak force tends to occur near the instant where the maximum velocity is imposed which is when most of the states have nearly zero derivatives. This is the instant where the behavior is closest to steady flow conditions for sinusoidal inputs. The exception in the case of a monotube are the states due to the rod and headside capacitors which again are related to the

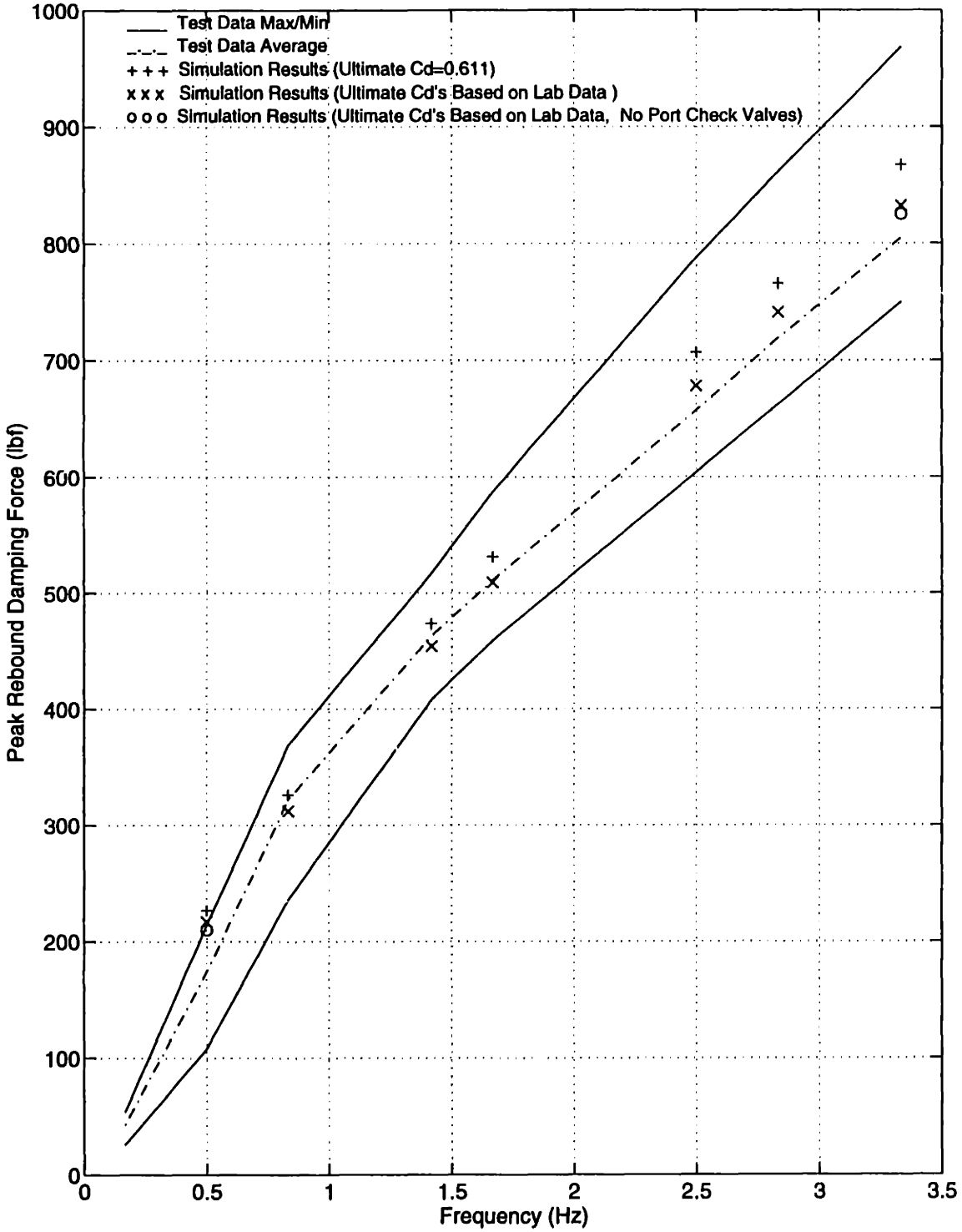

Figure 3.1: Verification of valving model

equivalent displacement of the gas volume and will be handled as described above.

Test data for the peak rebound damping force at various frequencies for a constant 1.5in input displacement amplitude are shown in Figure 3.1. The maximum and minimum peak forces for several input cycles are shown in addition to the average peak force in order to consider cycle to cycle variation. Simulation results for seven frequency cases are plotted for the model force. Several simulation configurations were run. One configuration idealized the bleed and blow-off valve orifices as sharp-edged slit type orifices. A second configuration used ultimate discharge coefficients derived from test data for the actual (non-ideal) orifice types used in the sinusoidal testing. A third case reduces the check valve preload to zero in order to identify the sensitivity of the output force to the hysteresis produced by the check valve (see Sect. 3.2.5). The simulation results are in close agreement with the test data for all simulated frequencies (0.5-3.3Hz). The ultimate discharge coefficient derived from testing produced better results compared to average test data at high frequencies. In the middle frequency range the results were similar for either discharge coefficient assumption. The lowest frequency simulation results were on the high side of the test data results. The difference at low frequencies is most probably due to the floating piston friction in the monotube model which results in hysteresis at low velocities (see Sect. 3.2.7) that is probably more significant than the hysteresis in the actual dualtube shock absorber at low velocities.

3.2 Monotube Dynamic Simulation Results

Dynamic simulation results for a realistic monotube design are presented in this section. Test data for an actual monotube design were not available at the time of this writing. The design configuration simulated is shown in Table 3.2. The rebound and

Shock Parameter	Value	Units
Shock Absorber Tube Diameter	36	mm
Nitrogen Gas Equilibrium Pressure	20	Bar
Nitrogen Gas Equilibrium Volume	50	cc
Check Valve Preload	0.050	MPa
Port Restriction $\frac{L}{D}$	1.45	DMSL
Port Restriction Quantity	4	DMSL
Orifice Discharge Coefficients	0.611	DMSL
Bleed Slot Quantity	8	DMSL
Blow-off Valve Preload	0.2	MPa
Floating Piston Static Friction	55	N
Floating Piston Dynamic Friction	50	N

Table 3.2: Significant monotube simulation parameters

compression valving designs are identical.

The results of several test cases are shown in the following sections. These cases demonstrate the dynamics of monotube shock absorbers and the effect of changes in parameters which influence the dynamic response of the shock absorber. The dynamic performance is evaluated from the characteristic force-displacement and force-velocity curves.

3.2.1 Example Test Case at 5Hz

An example simulation is examined in this section which describes the operation of this monotube design starting from rest. The input is a sinusoidal velocity applied to the base of the tube while the piston end is held fixed. The input is $100\frac{mm}{s}$ maximum velocity at 5Hz for one cycle starting from rest. The full range displacement is about $0 - 6.4$mm.

Figure 3.2 shows the input velocity and displacement for this example case. The velocity is the relative velocity of the shock absorber ends such that a positive value

extends the shock absorber. The output force is the total force on the shock absorber piston (or rod end) for an input velocity applied to the tube base. The total force includes the load required to offset the nitrogen chamber pressurization. As a result, there is a "static" load required to maintain the piston rod end in an equilibrium state of nearly 200N.

The fluid flow model results are shown in Figures 3.3, 3.4, and 3.5. Figure 3.3 shows the results for the fluid port, bleed, and blow-off valve flowrates through the piston orifices. The compression circuit port flow does not immediately begin once the piston starts moving. This is a result of the port check valve which does not open until sufficient pressure has built up across the port restriction (see Figure 3.7). During the first time step (each time step in this example is 0.002s), the pressure builds until the check valve opens. By 0.002s, the compression port restriction is fully open allowing flow to pass through the bleed restriction slots. The flow of the port restrictions continues to increase as the pressure builds across the piston. Note, the sum of the bleed restriction flows is nearly identical to the sum of the port restriction flows in Figure 3.3. At about 0.030s, the pressure across the bleed restriction exceeds the blow-off valve preload and the blow-off valve opens. The additional flow across the piston tends to equilibrate the pressure difference and flatten the output force response (see Figures 3.2, 3.6, and 3.7). The compression blow-off valve closes at approximately 0.068s when the pressure drops again below the "blow-off" threshold. The port check valve closes at about 0.01s when the pressure difference across the valve drops below its threshold. A similar sequence of events occurs during the rebound stroke in the second half of the cycle. The leakage flow around the piston is also shown in Figure 3.3. Because of the nominally tight clearances, this leakage flow is very small as compared to the orifice flows.

Figures 3.4 and 3.5 show the piston flow channel Reynolds numbers and discharge

coefficients. The Reynolds number of the port channels is low enough in this example that the fully developed flow profile would be laminar. The bleed and blow-off orifice flow is effectively in the laminar regime for less than one time step while the fluid is passing through the orifices because of their low transitional Reynolds number. Once the blow-off valve opens, the bleed orifice flow merges with the blow-off valve flow.

The pressures of the nitrogen gas, rod, and headside chamber volumes are shown in Figure 3.6, as are the pressure differences across the port channels floating piston. During the first 0.002s, the pressure in the rebound chamber drops as the fluid is extended while very little flow entered the rebound chamber. Once the rebound check valve opens, the pressure builds up before dropping again when the input velocity effects overcome the effects of the entering fluid flow on the pressure. The pressure flattens out when the blow-off valve opens. The headside volume pressure increases due the the compression of the nitrogen gas volume. When the rebound stroke begins, the rodside pressure initially increases while both check valves prevent fluid flow from entering either volume. The rebound check valve valve opens at betwen $0.100 - 0.102$s when fluid flow to the headside volume begins reducing the rodside pressure. This pressure begins to increase again as the stroke velocity increases. A similiar cycle of events occurs for the remainder of the rebound stroke. The offset between the headside volume and gas volume pressures is effectively the pressure loss due to the friction on the floating piston. The pressure differences across the flow channels, as compared to the pressure difference across the piston, are shown in Figure 3.7. Most of the pressure losses occur across the more narrow bleed and blow-off orifices.

Figure 3.8 shows the forces and velocities acting on the floating piston and the volume of the nitrogen gas chamber. The floating piston "sticks" to the tube for the first 0.004s after which it begins to slide relative to the tube until 0.1s when the net force acting on the piston reverses and it enters the stiction region again as the

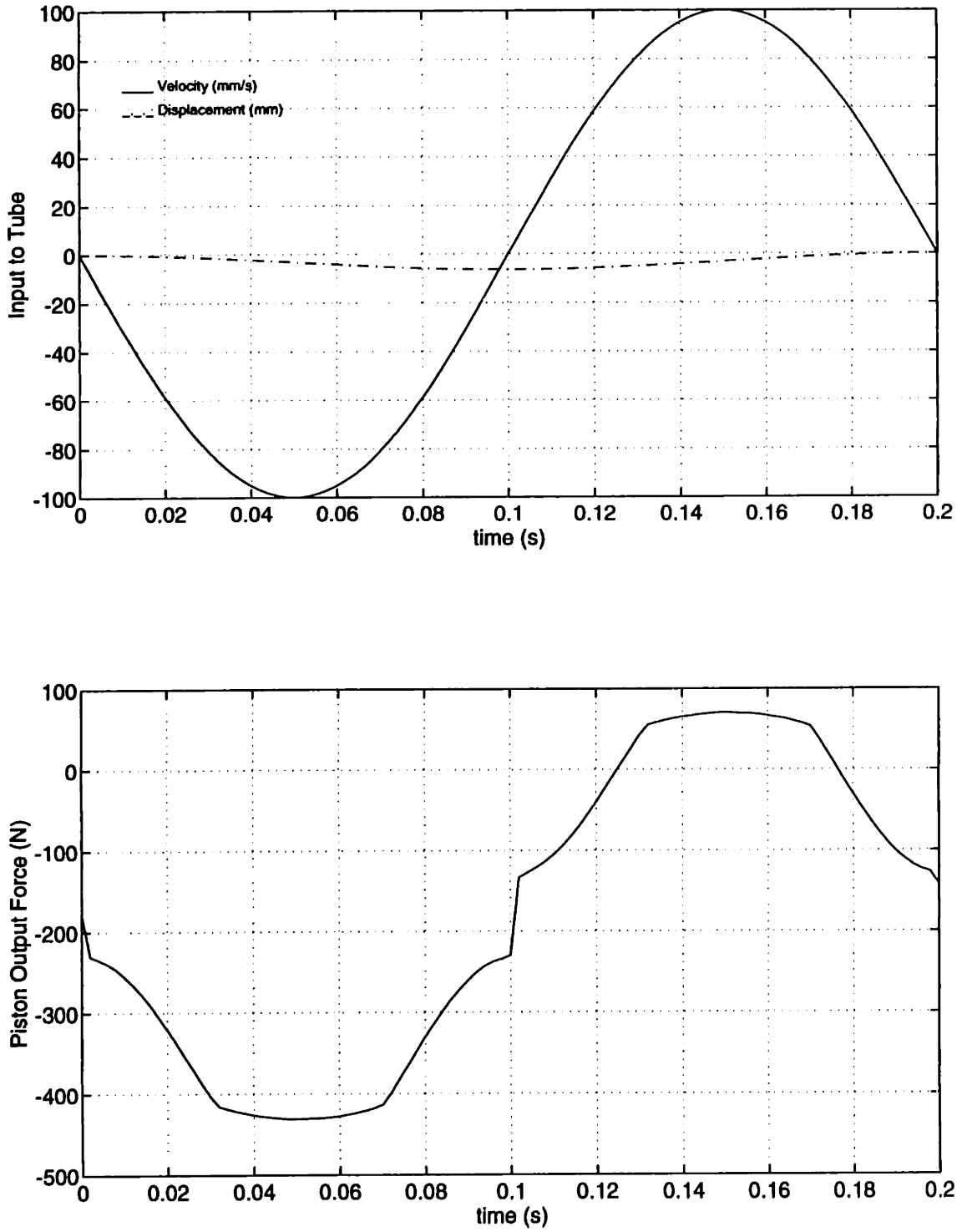

Figure 3.2: Shock absorber input and output ($V_{max} = 100\frac{mm}{s}$ at 5Hz)

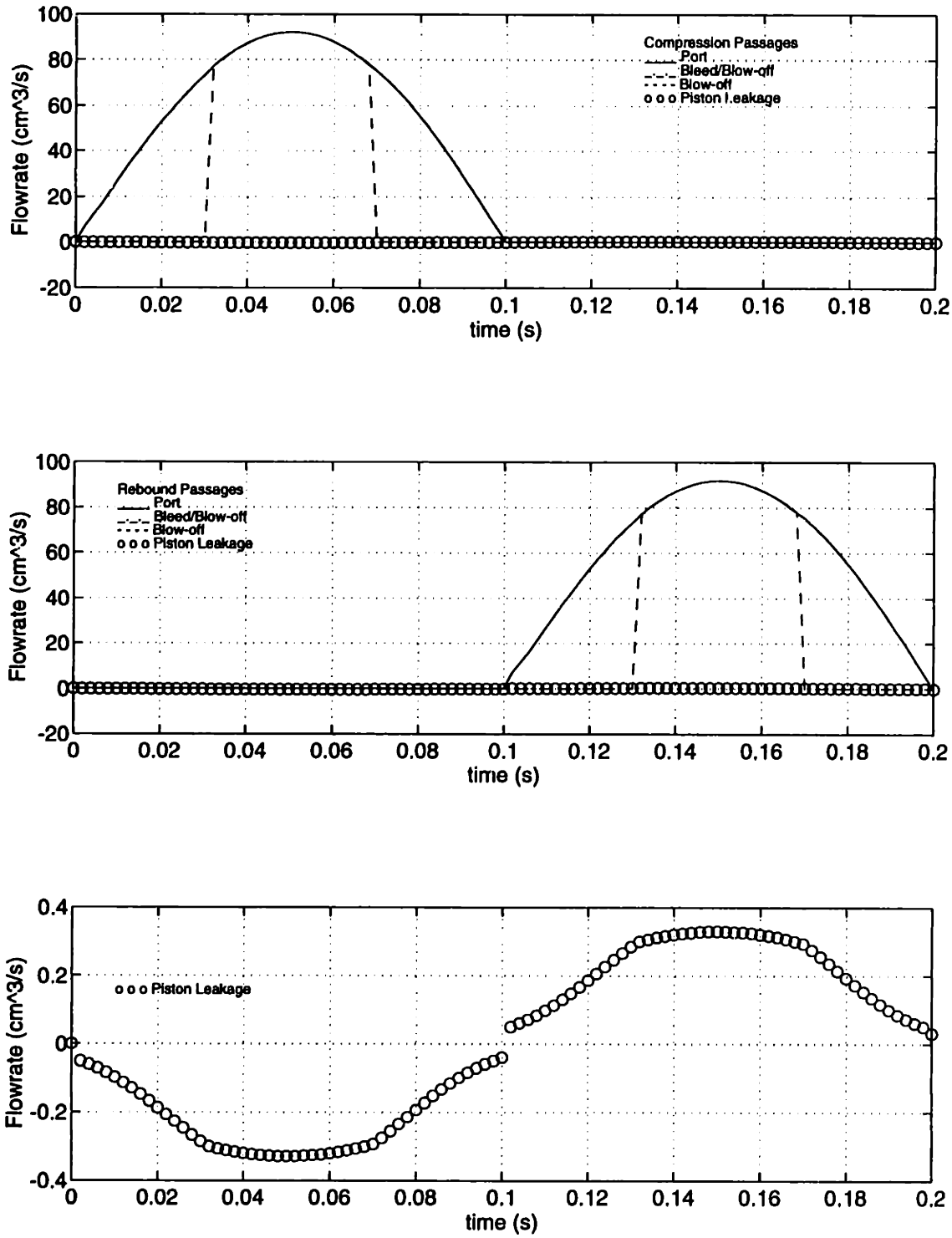

Figure 3.3: Fluid flow across piston ($V_{max} = 100\frac{mm}{s}$ at 5Hz)

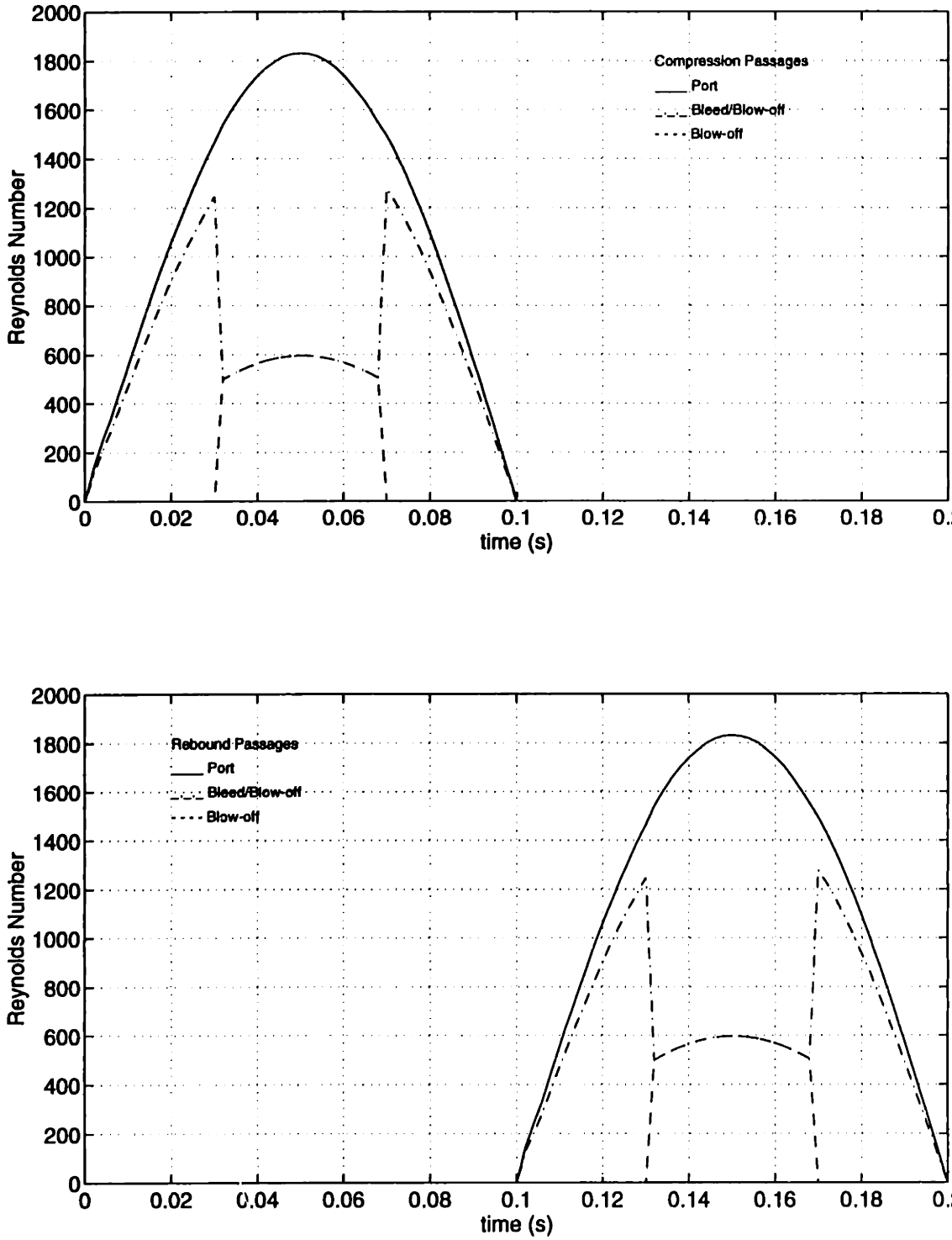

Figure 3.4: Fluid flow Reynolds number ($V_{max} = 100\frac{mm}{s}$ at 5Hz)

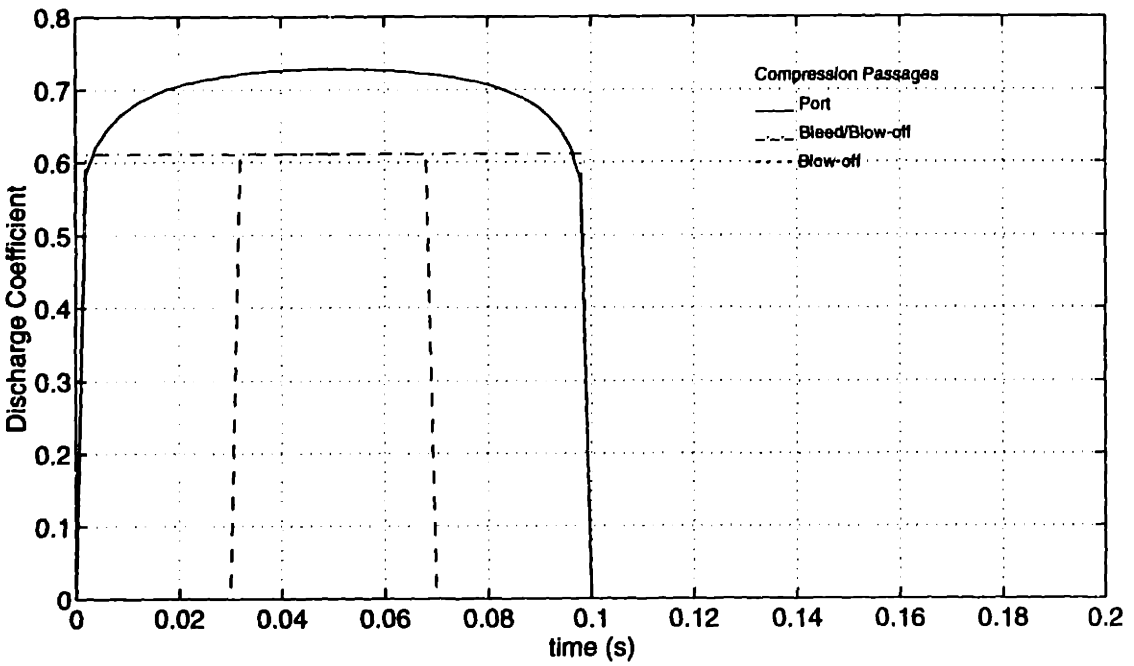

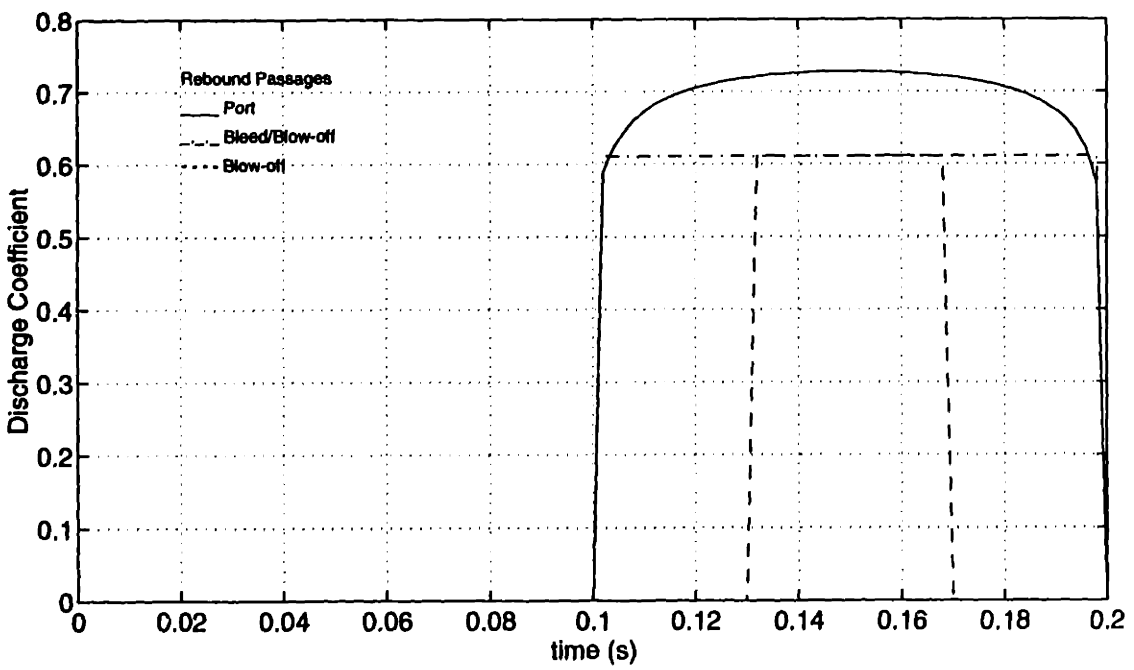

Figure 3.5: Fluid flow discharge coefficient ($V_{max} = 100\frac{mm}{s}$ at 5Hz)

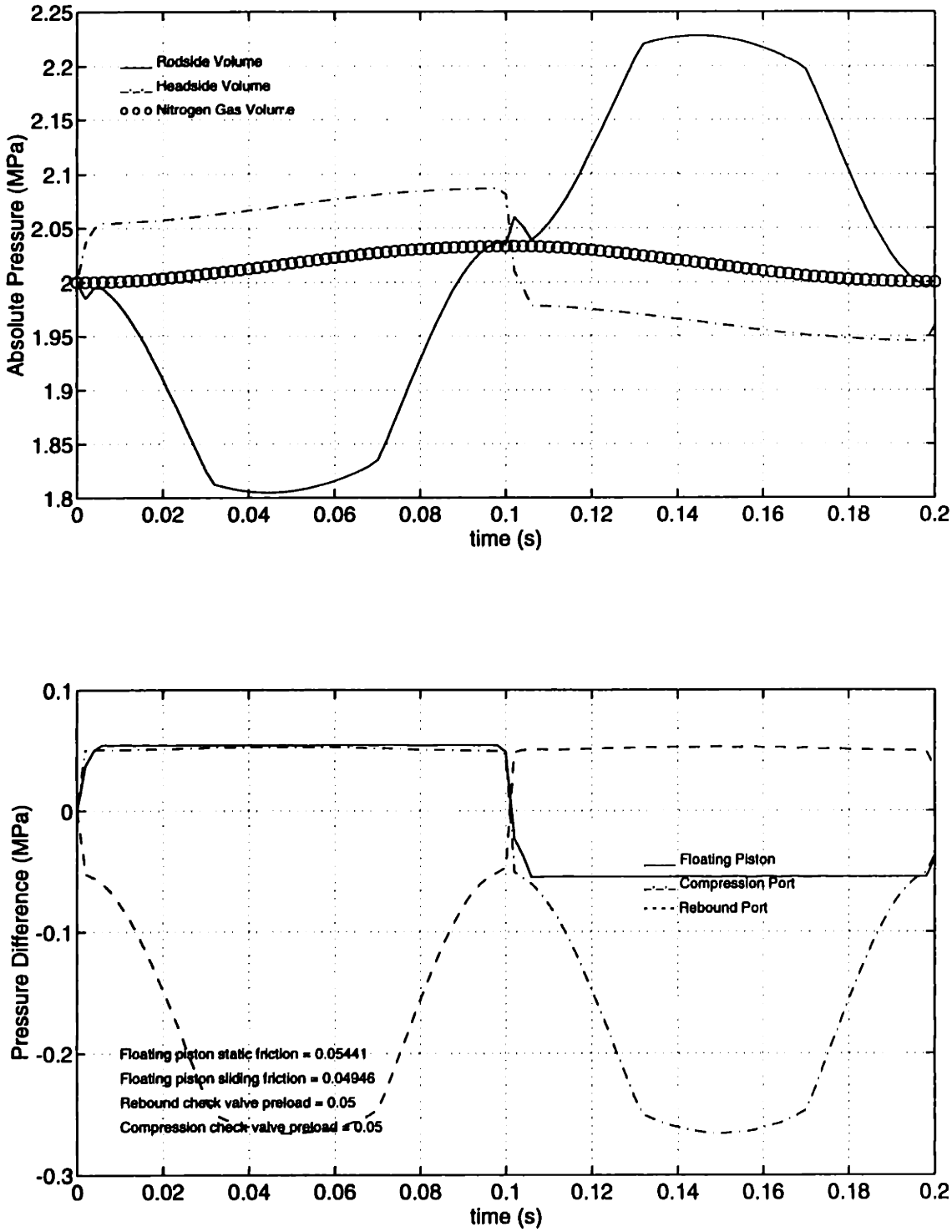

Figure 3.6: Floating piston, rod and headside pressures ($V_{max} = 100\frac{mm}{s}$ at 5Hz)

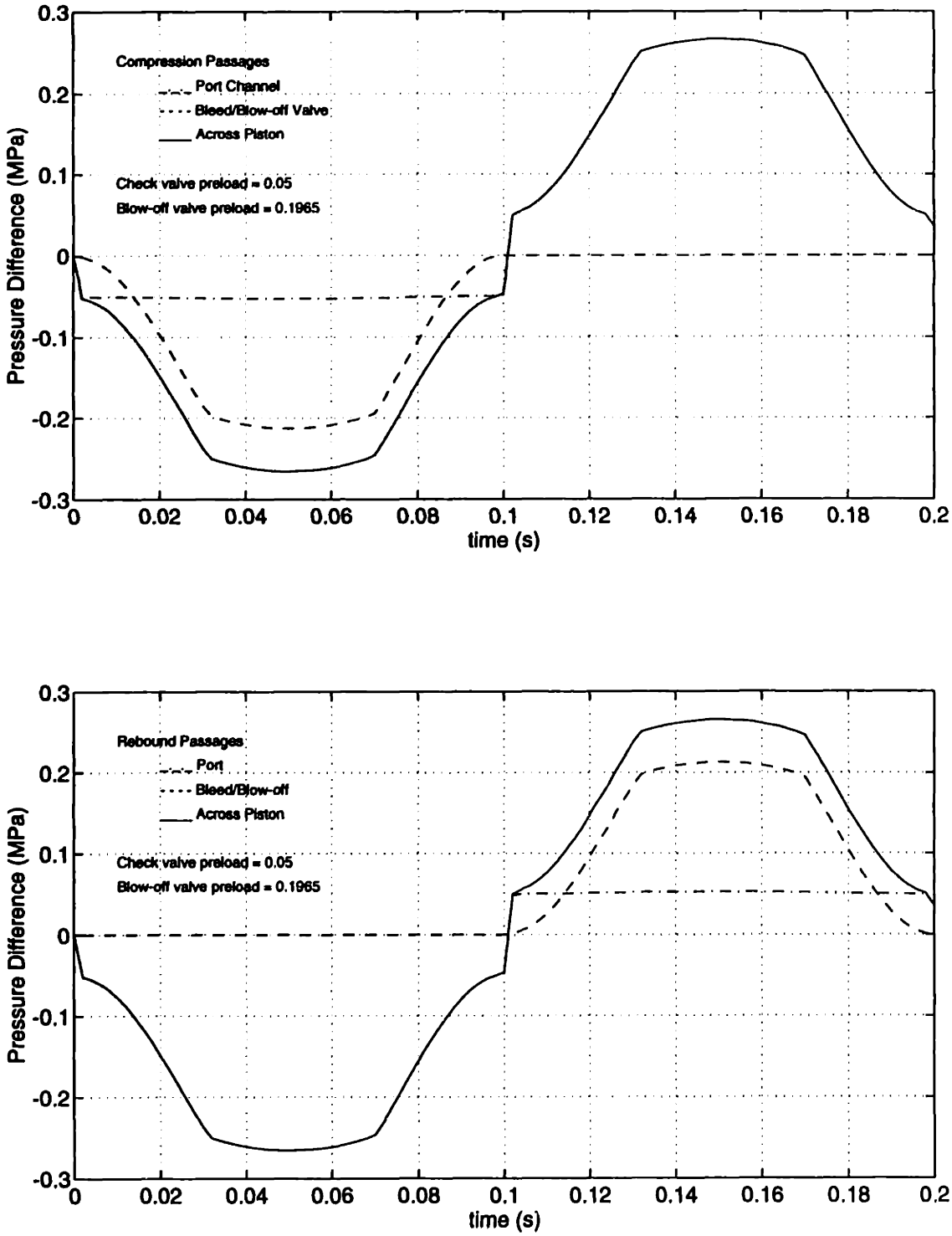

Figure 3.7: Piston fluid flow pressures ($V_{max} = 100\frac{mm}{s}$ at 5Hz)

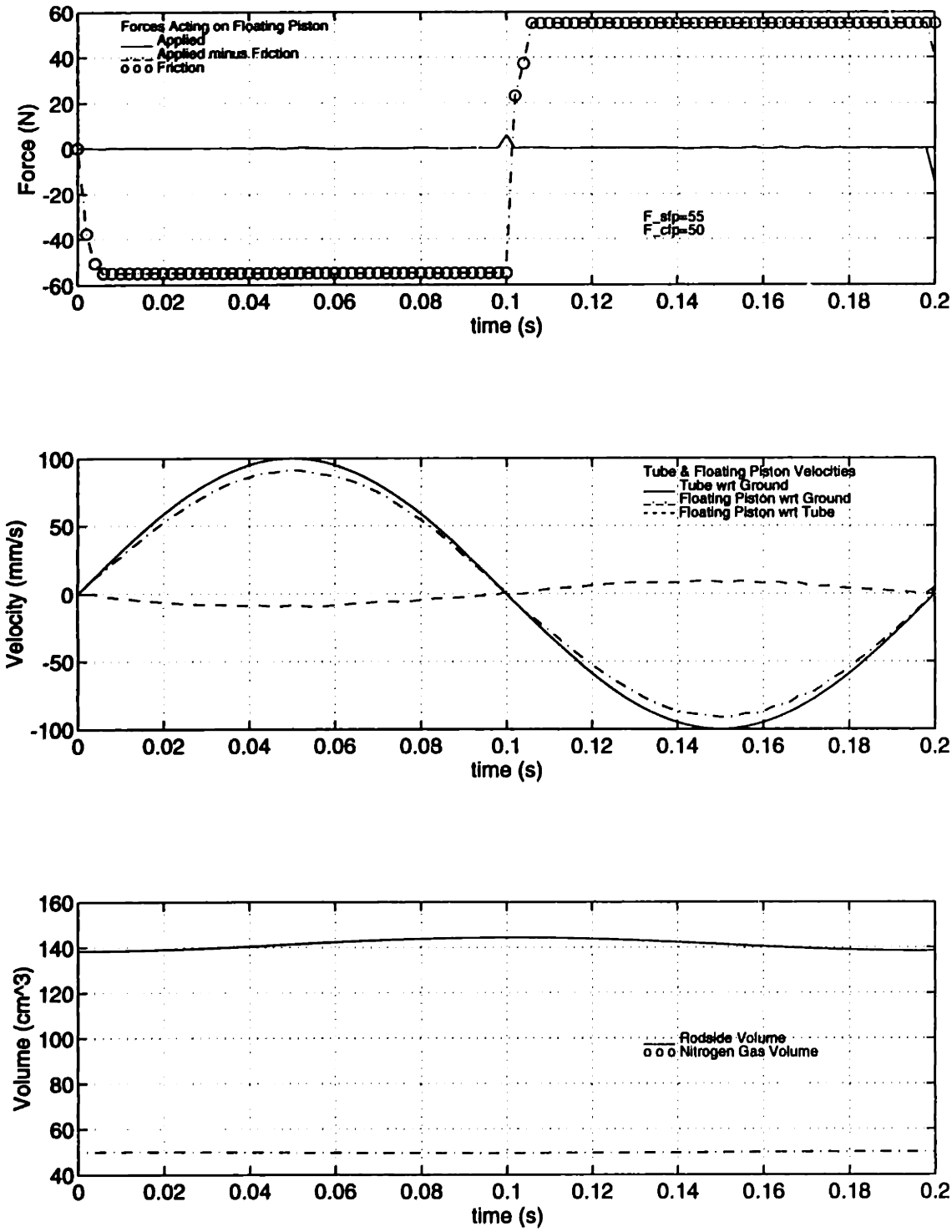

Figure 3.8: Floating piston and gas volume parameters ($V_{max} = 100\frac{mm}{s}$ at 5Hz)

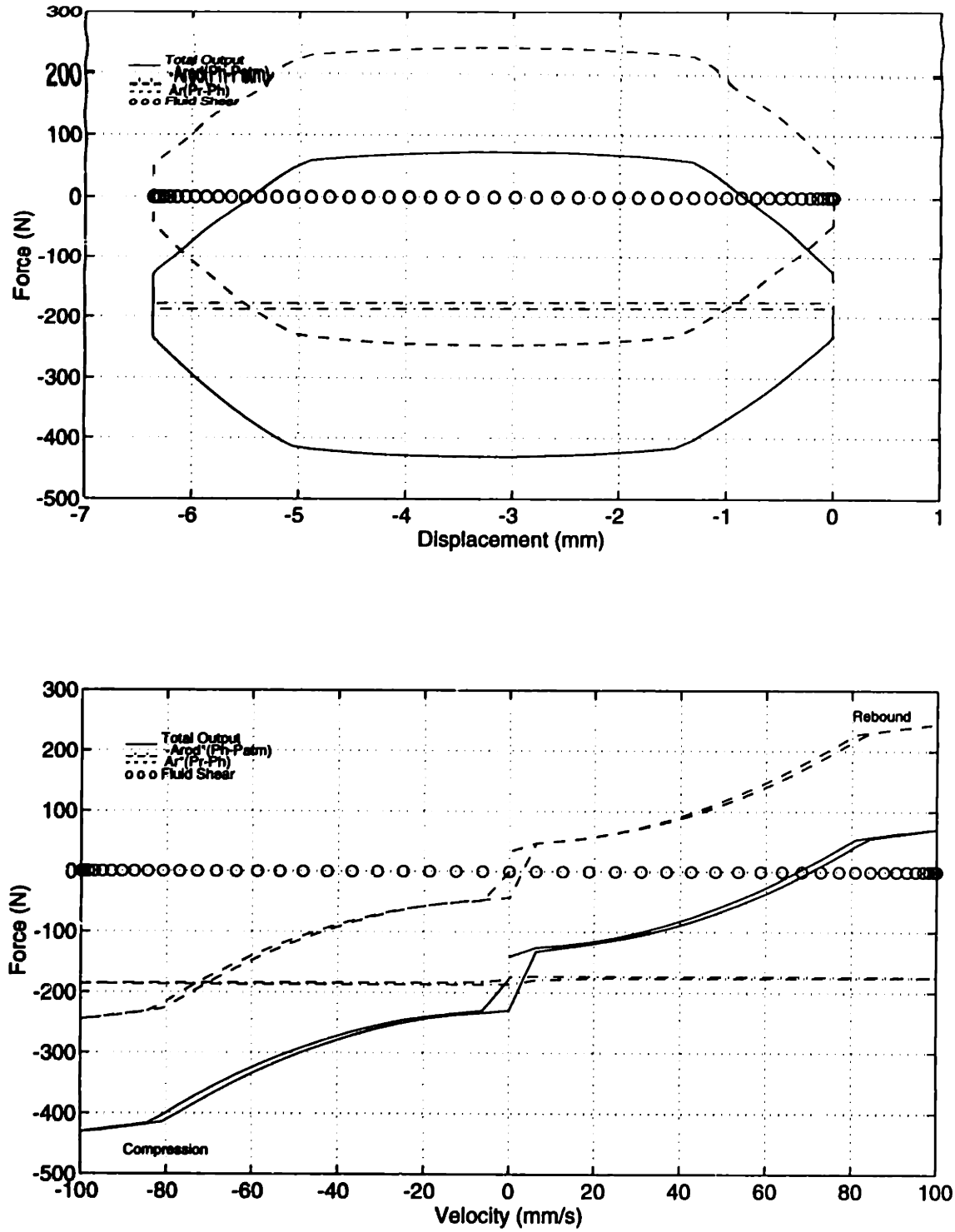

Figure 3.9: Force-displacement and force-velocity diagrams ($V_{max} = 100\frac{mm}{s}$ at 5Hz)

rebound stroke begins. The floating piston begins sliding again at 0.106s. The gas volume is fairly constant for this example where the maximum shock displacement is only 6.4mm.

Figure 3.9 shows the force-displacement and force-velocity diagrams for this case. The total force is shown along with components of the total shock absorber force (see Eqn. (2.173)). Showing the component $-A_{rod}(P_h - P_{atm})$ attempts to isolate the effect of the gas pressure on the piston, while the component $A_r(P_r - P_h)$ removes the effect of unequal piston areas and highlights the compliance effects of the fluid volumes and the resistive pressure losses across the piston. The fluid shear component is the term $-F_{rp}$ in Eqn. (2.173) and results from the fluid leakage around the piston. The shear component is negligible for this case. The hysteresis seen in both the force-displacement and force-velocity curves will be investigated parametrically in the following sections of this chapter.

3.2.2 Restriction Inertia and Variable Discharge Coefficients

The results for the restriction flowrates indicated the flow acceleration rates were typically small or of extremely short duration so as to have a negligible impact on the dynamics of the shock absorber. The same could be said for the variable discharge coefficients in the bleed and blow-off restrictions. The low transitional Reynolds number tended to result in laminar flow for very short durations even for very low velocities. The check valve preload in the design in this study produced a build-up in pressure across the restrictions larger than the pressure drop across the bleed restriction required for transition to turbulent flow. The variable discharge coefficient for the port flow was typically of significant duration during the cycle. However, the pressure drop across the port restrictions used in this study was negligible when compared to the check valve preload due to the larger size and the quantity of these

restrictions.

3.2.3 Excitation Frequency

The influence of the stroking frequency of shock absorbers has been (and continues to be) a source of interest to manufacturers. In this study, the effect of frequency on the dynamic characteristics is examined at both constant maximum velocity and constant maximum displacement.

Constant Maximum Input Velocity

Various cases were run for the same maximium velocity. By holding the maximum velocity constant between cases, the maximum displacement for each successive simulation reduces as the frequency increases. This is made evident in the figures of the force-displacement plane.

Four different frequency cases $(1, 5, 10, 20\text{Hz})$ were run at $50\frac{mm}{s}$. The results in Figures 3.10 and 3.11 indicate the width of hysteresis loop in the force-displacement plane remains the same with increasing frequency because the maximum force is about the same for the different frequencies. The hysteresis is largest at 1Hz in the force-velocity plane particularly in the region near zero velocity. The difference between the total load and the force component, $A_r(P_r - P_h)$, would seem to attribute this to the larger displacement at the lower frequency. Figures 3.12 and 3.13 show the amount of force-velocity hysteresis slightly increasing with increasing frequency between $5 - 20$Hz.

The same four frequency cases were run at $100\frac{mm}{s}$. Figures 3.14 and 3.15 more clearly show the larger total force-velocity hysteresis at 1Hz near zero velocity where the relative displacement is largest. At higher velocities, the hysteresis increases monotonically with frequency. The hysteresis in the $A_r(P_r - P_h)$ force component is

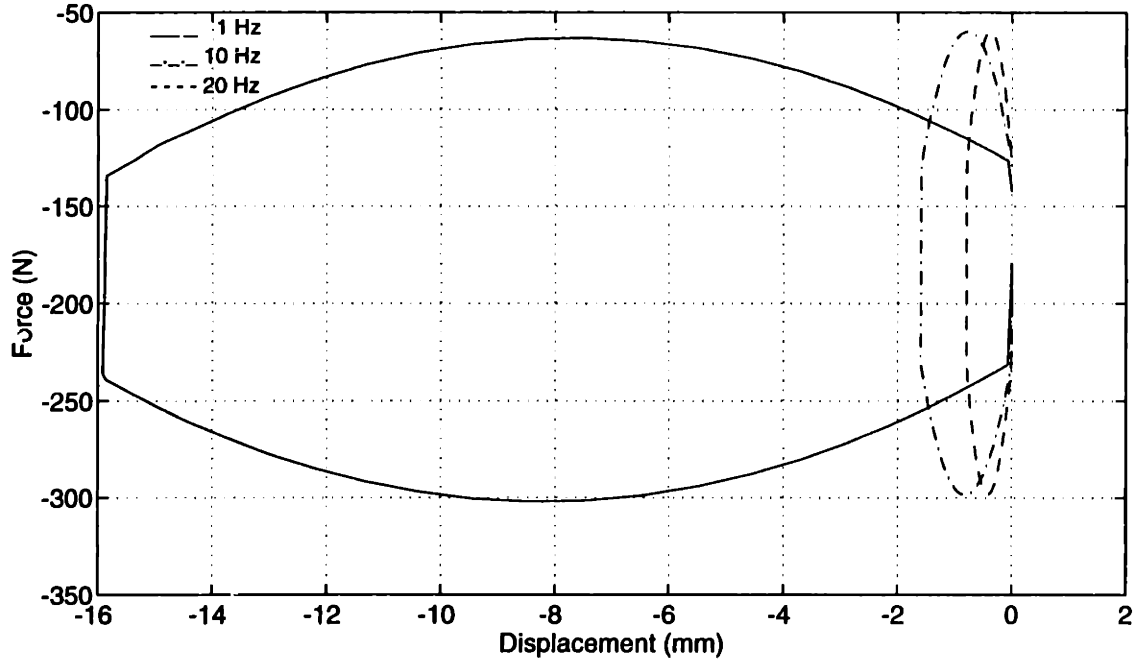

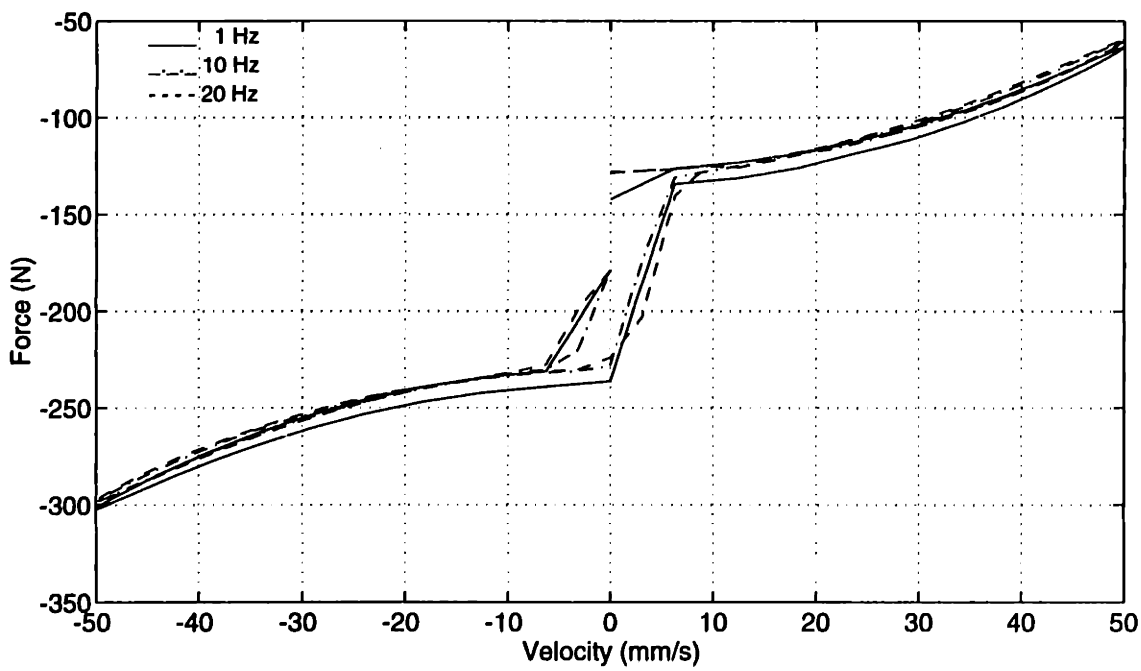

Figure 3.10: Force-displacement and force-velocity diagrams ($V_{max} = 50\frac{mm}{s}$ at $1, 10, 20$Hz)

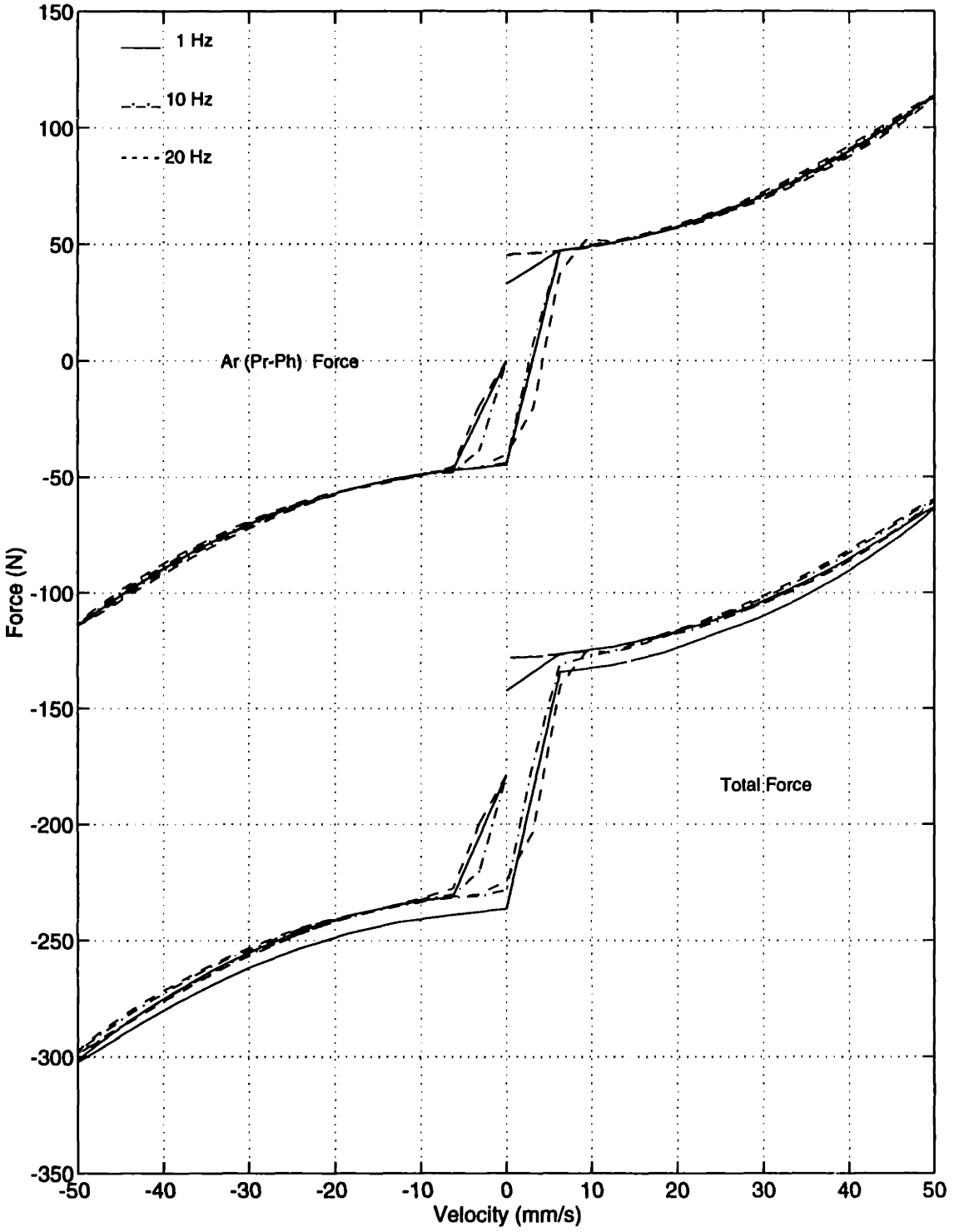

Figure 3.11: Force(component)-velocity diagram ($V_{max} = 50\frac{mm}{s}$ at $1, 10, 20$Hz)

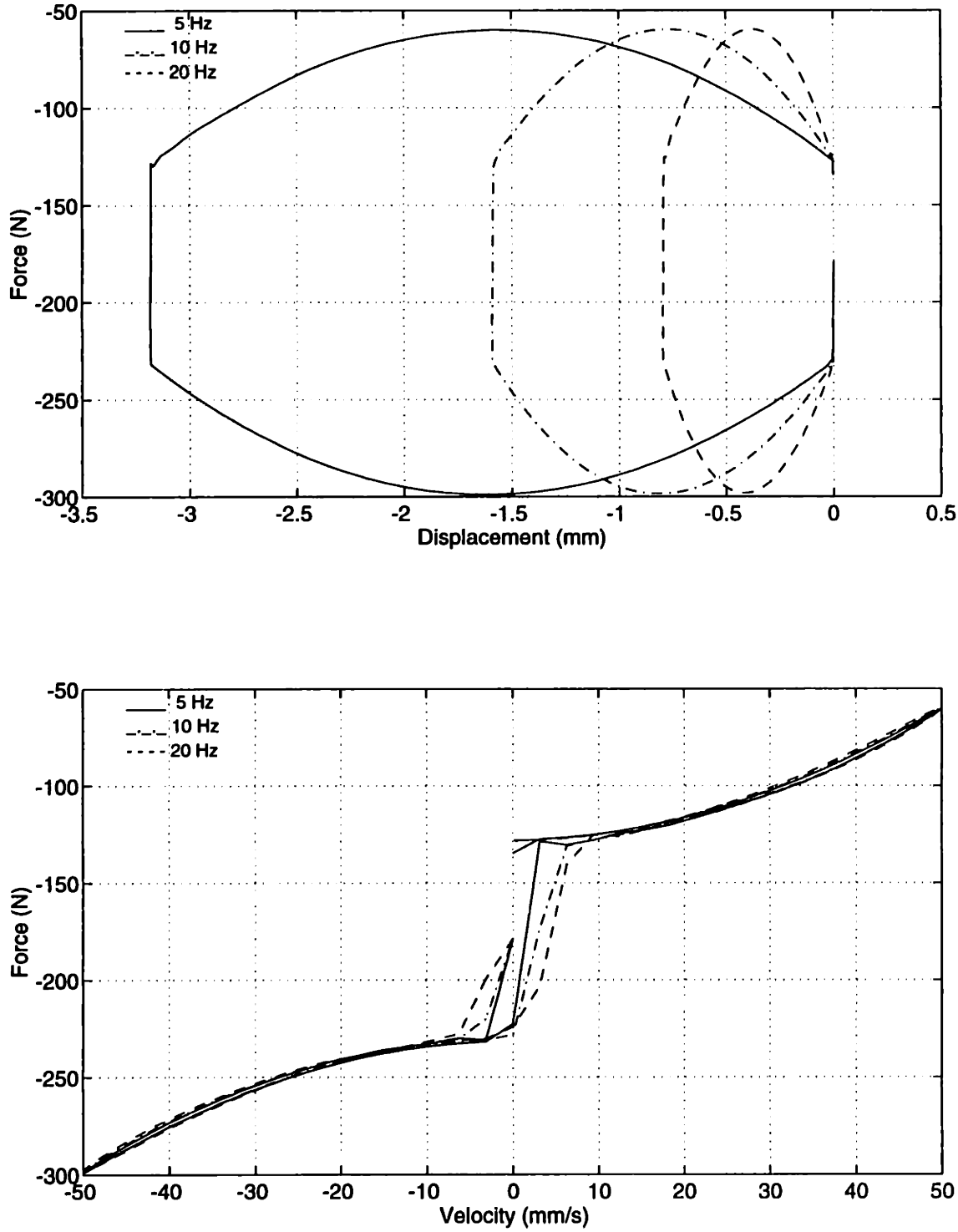

Figure 3.12: Force-displacement and force-velocity diagrams ($V_{max} = 50\frac{mm}{s}$ at 5, 10, 20Hz)

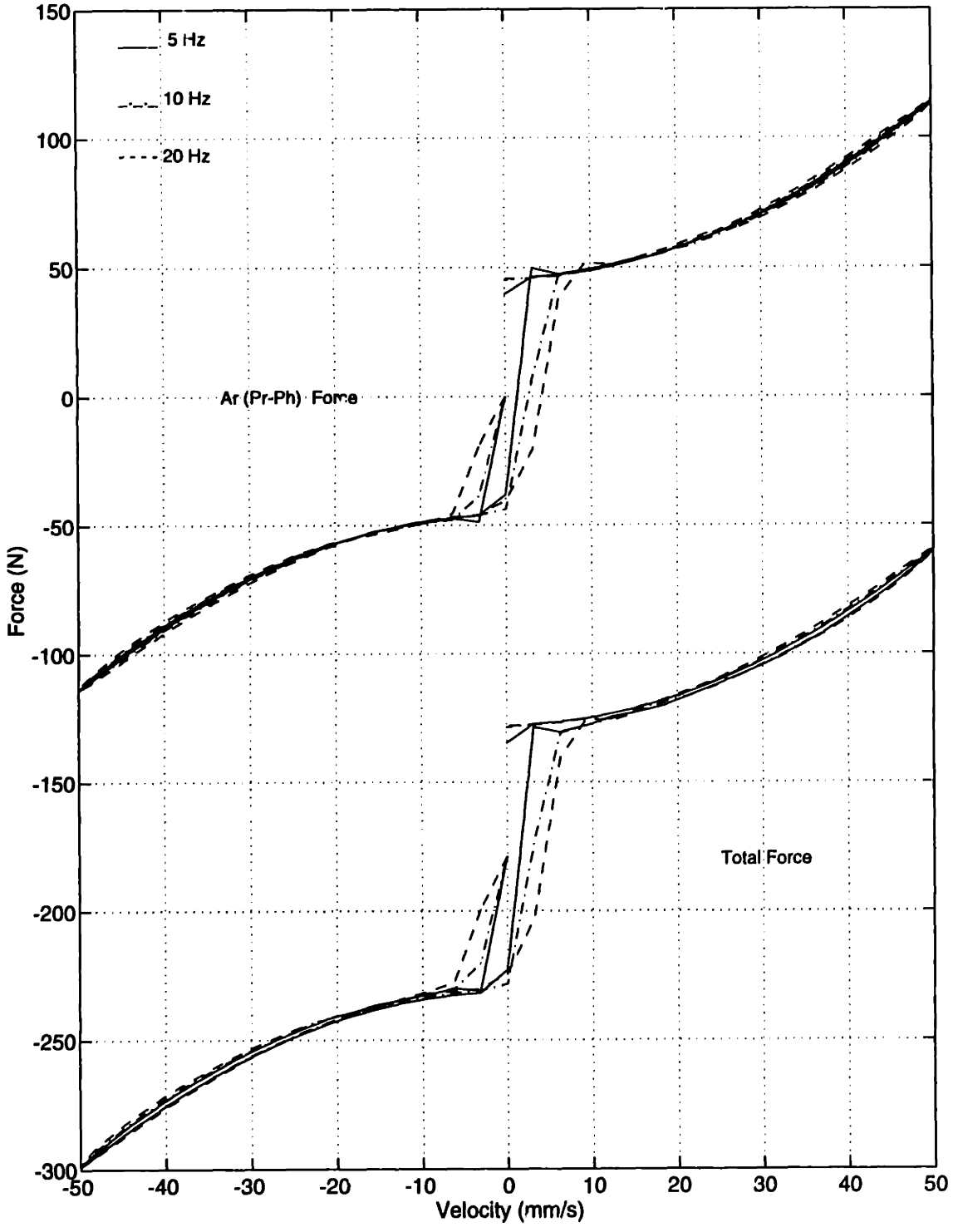

Figure 3.13: Force(component)-velocity diagram ($V_{max} = 50\frac{mm}{s}$ at $5, 10, 20$Hz)

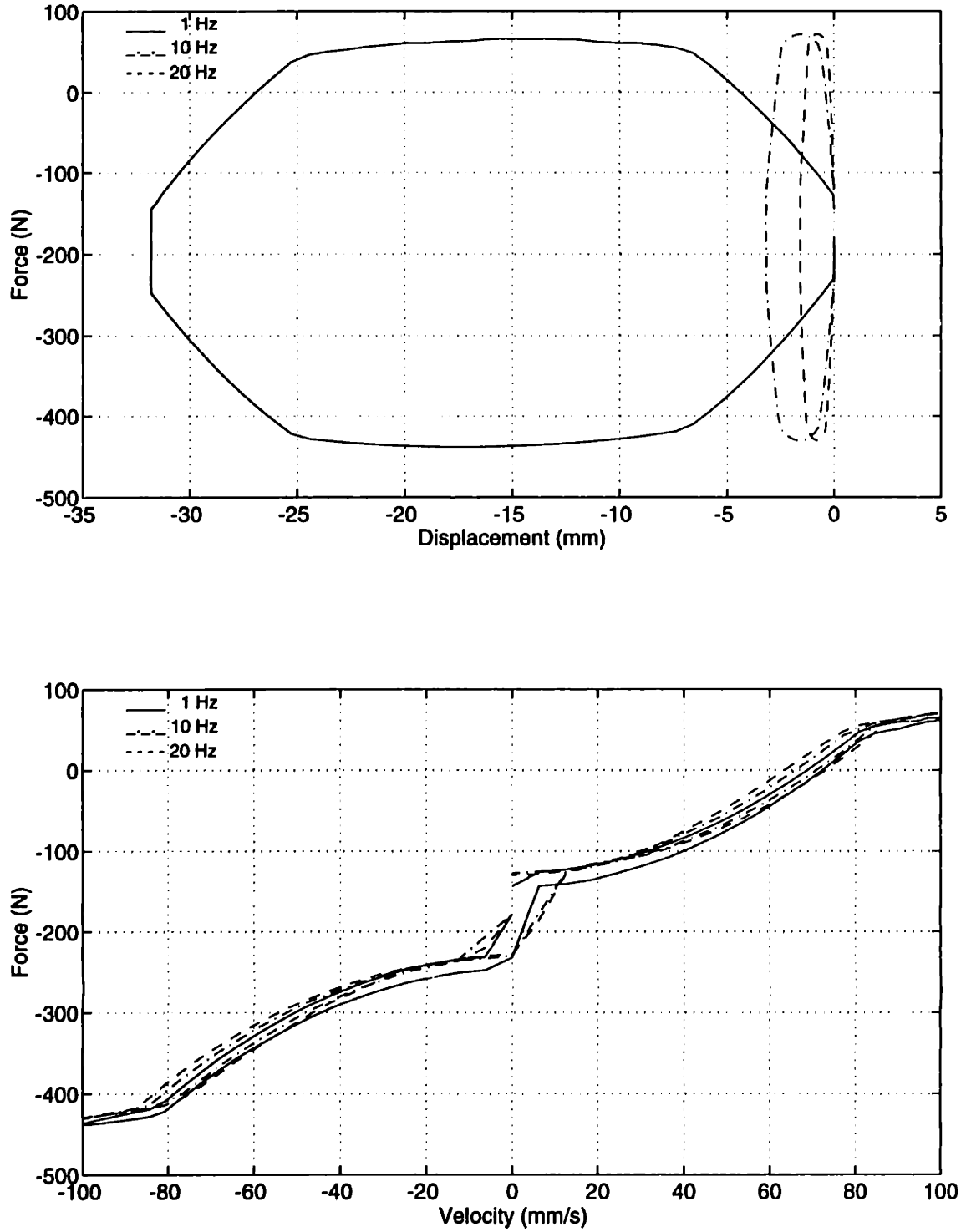

Figure 3.14: Force-displacement and force-velocity diagrams ($V_{max} = 100\frac{mm}{s}$ at $1, 10, 20$Hz)

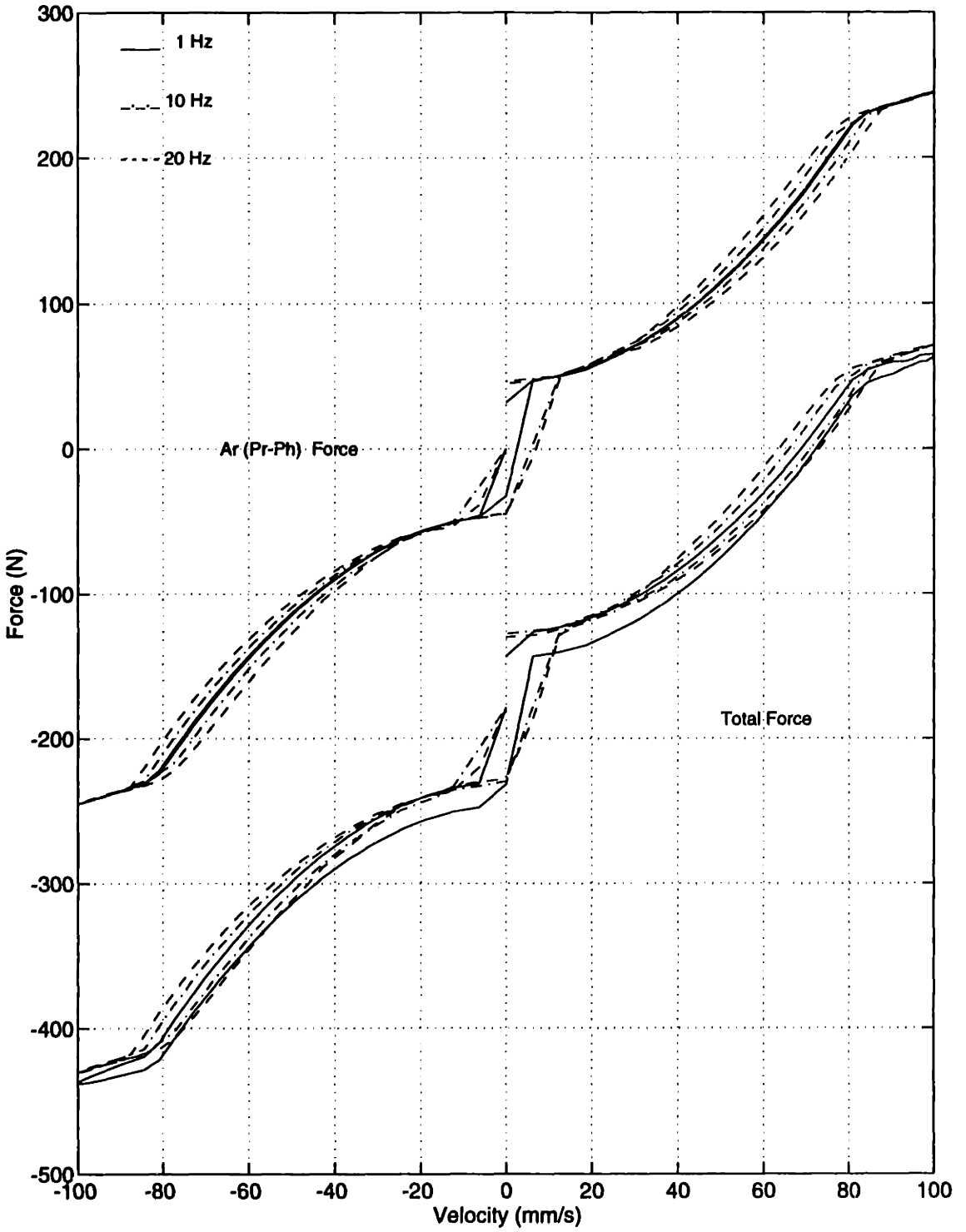

Figure 3.15: Force(component)-velocity diagram ($V_{max} = 100\frac{mm}{s}$ at $1, 10, 20$Hz)

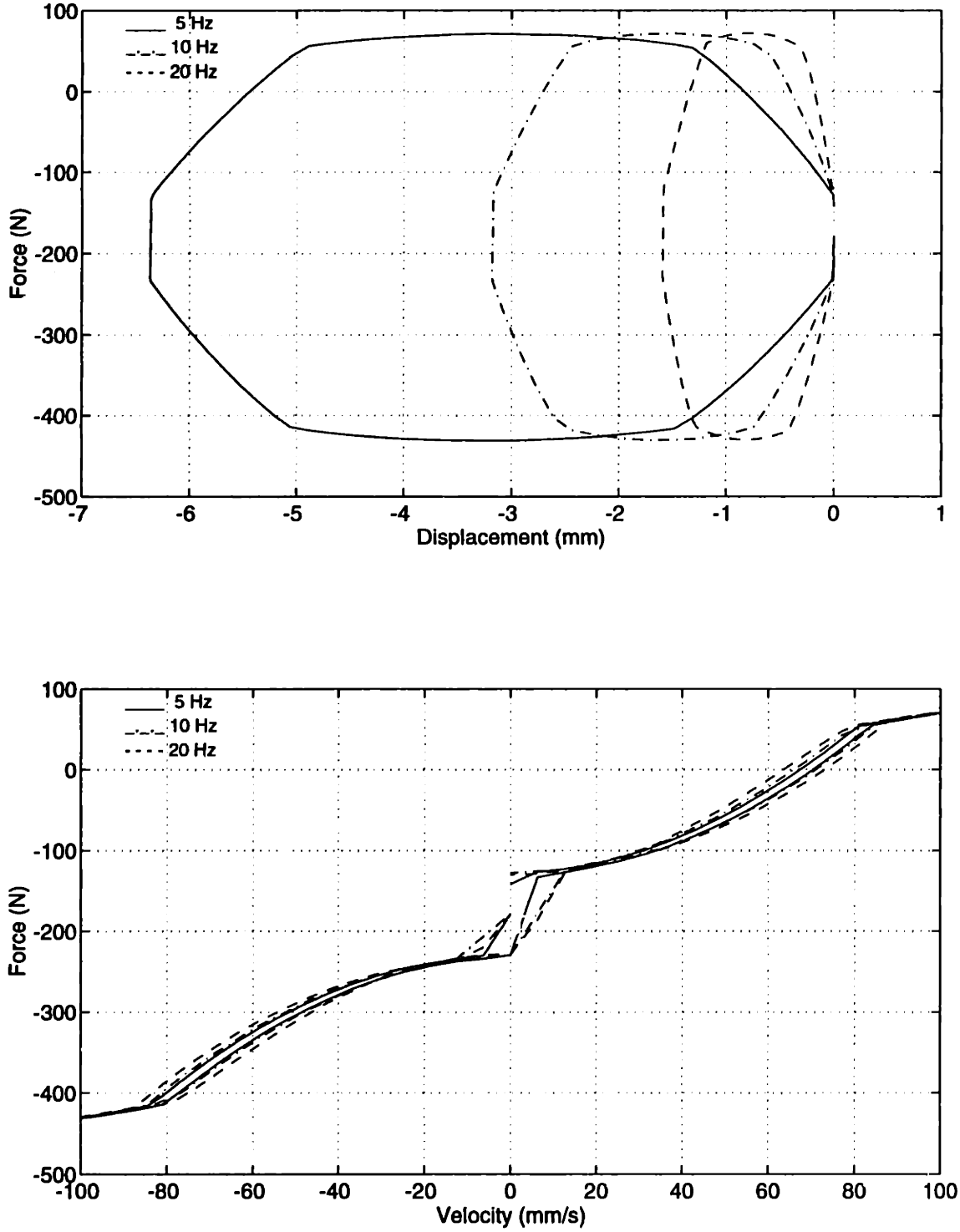

Figure 3.16: Force-displacement and force-velocity diagrams ($V_{max} = 100\frac{mm}{s}$ at 5, 10, 20Hz)

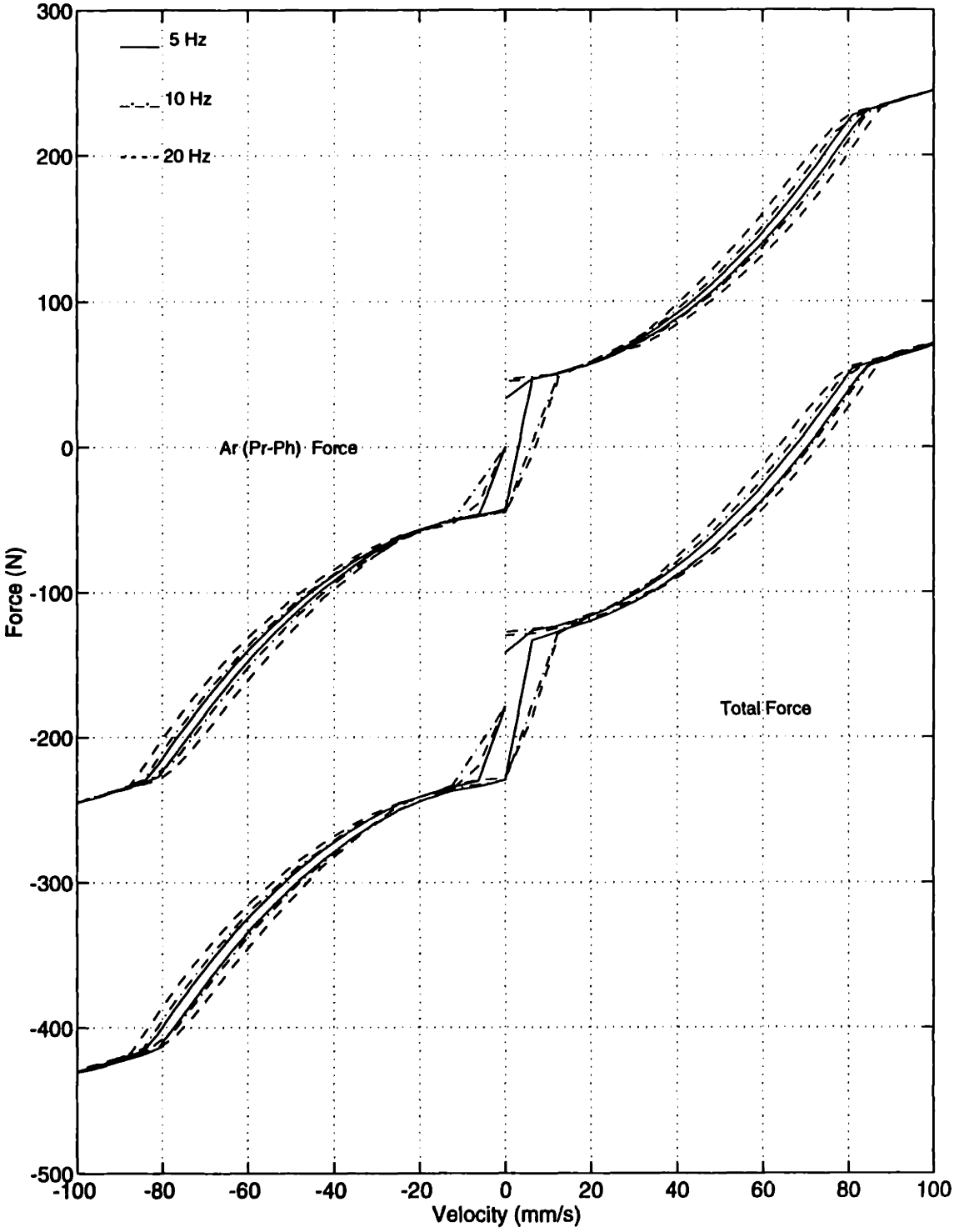

Figure 3.17: Force(component)-velocity diagram ($V_{max} = 100\frac{mm}{s}$ at $5, 10, 20$Hz)

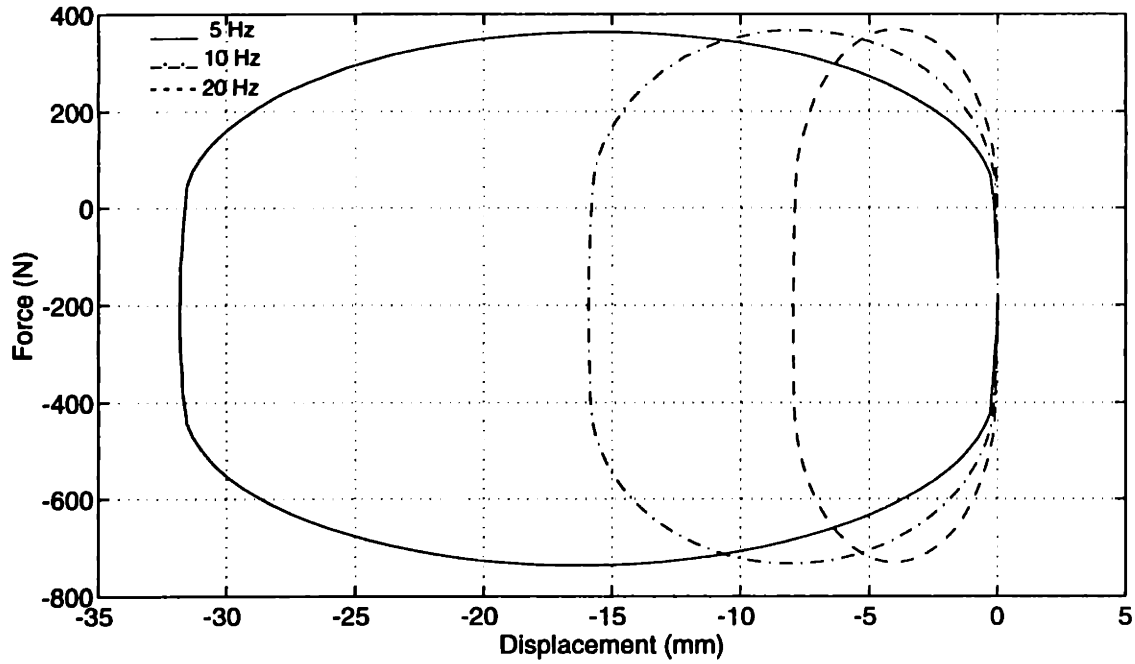

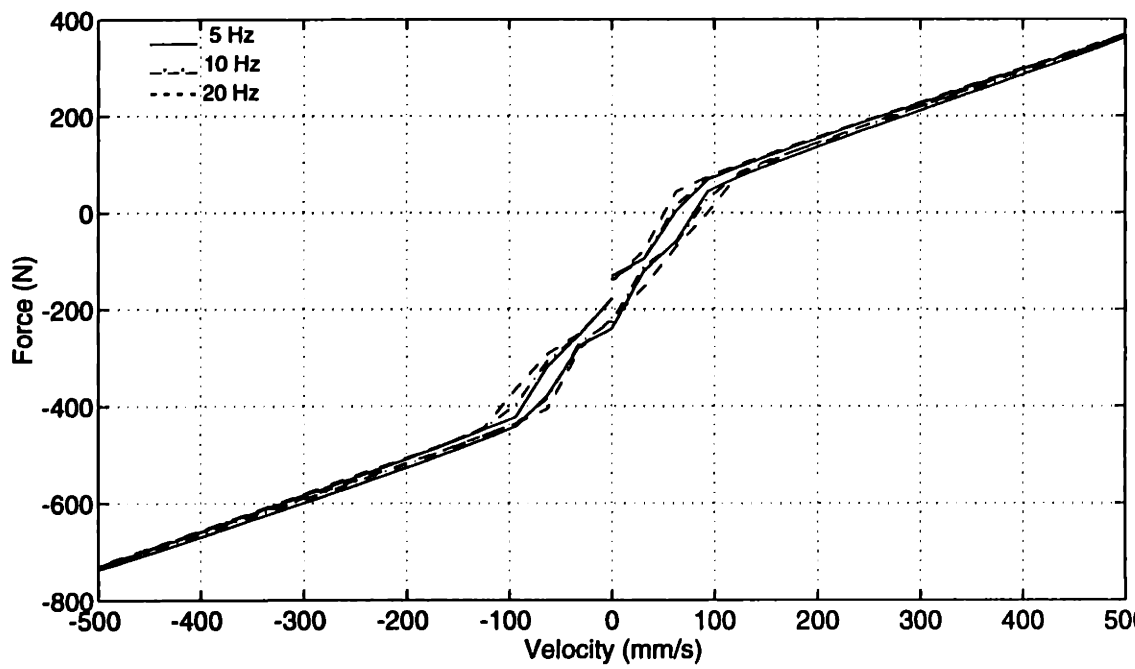

Figure 3.18: Force-displacement and force-velocity diagrams ($V_{max} = 500\frac{mm}{s}$ at 5, 10, 20Hz)

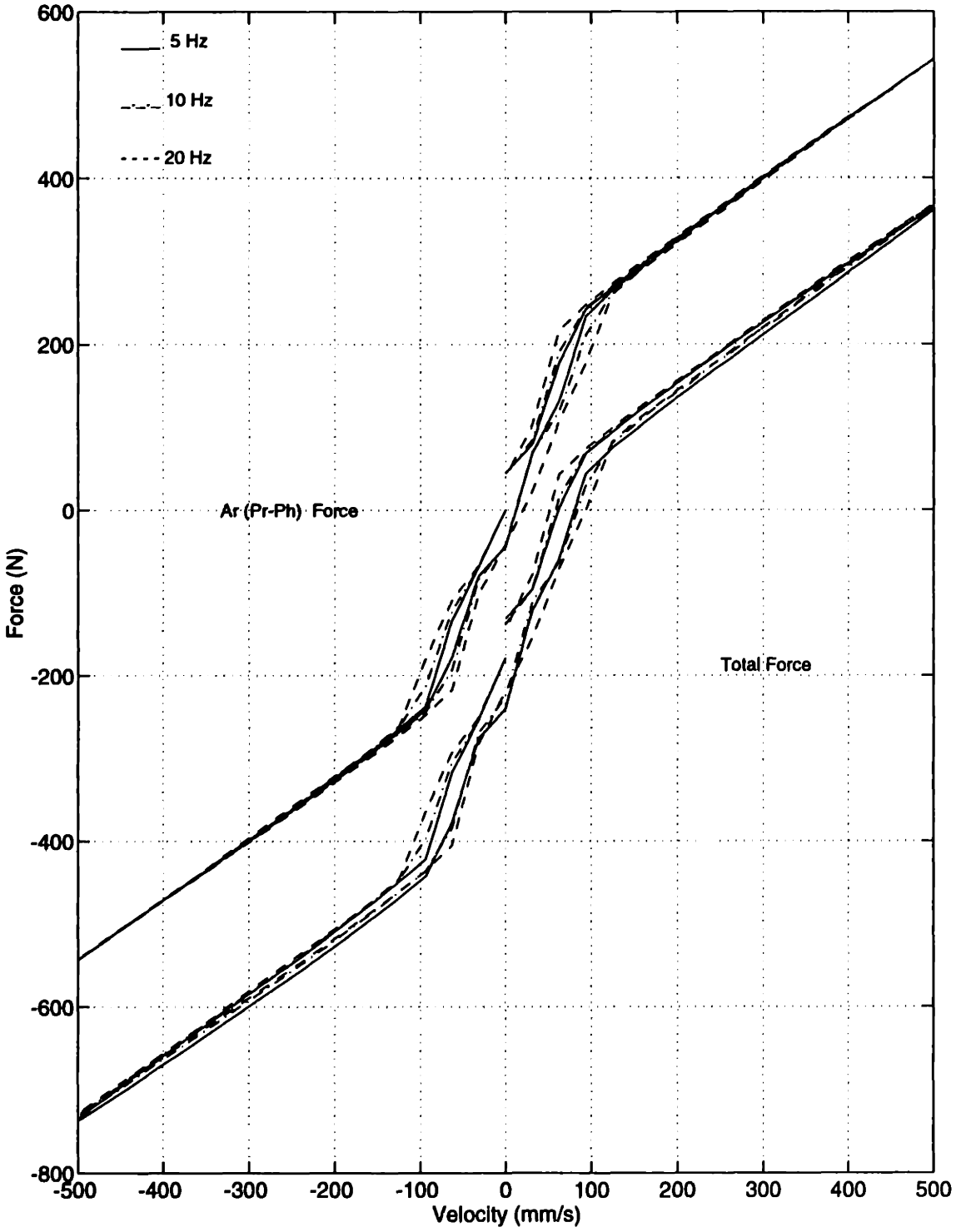

Figure 3.19: Force(component)-velocity diagram ($V_{max} = 500\frac{mm}{s}$ at $5, 10, 20$Hz)

everywhere larger with increasing frequency. Figures 3.16 and 3.17 indicate similar behavior although not as pronounced when comparing the 5Hz data to the 10 and 20Hz data. These trends also tend to attribute the hysteresis near zero velocity to the compression of the nitrogen gas volume and the hysteresis of the outer lobes to how the pressure varies in the rod and headside volumes during a cycle. Note the hysteresis in the force-velocity plane tends to collapse above $80\frac{mm}{s}$ when the blow-off valve opens.

Figures 3.18 and 3.19 at $500\frac{mm}{s}$ indicate similar trends with five distinct regions of hysteresis in the force-velocity plane. One near zero velocity where the amplitude appears to cause lower frequencies to have greater hysteresis. The second and third regions occur in the middle velocity region where the larger frequencies have the larger amount of hysteresis. Beyond the region where the blow-off valve opens, the lower frequencies again appear to have the greater hysteresis due to the larger displacements for the same maximum velocity. Note that the quadratic damping at high orifice flows is offset when the blow-off valve opens which "straightens" the force velocity curve.

Constant Maximum Input Displacement

Additional cases were run for the same maximium displacement. As a result, the maximum velocity for each successive simulation increases as the frequency increases. Note that the displacement is starting from 0mm. Hence, the total displacement is double the magnitude of the sinusoidal displacement input.

The hysteresis in the force-displacement plane increases as frequency increases as observed in Figure 3.20. The force-displacement hysteresis is related to the amount of energy dissipated per cycle. This result indicates that the larger obtained velocities result in larger static pressure losses for the same displacements due to increased orifice flows. The amount of force-velocity hysteresis is difficult to compare for different

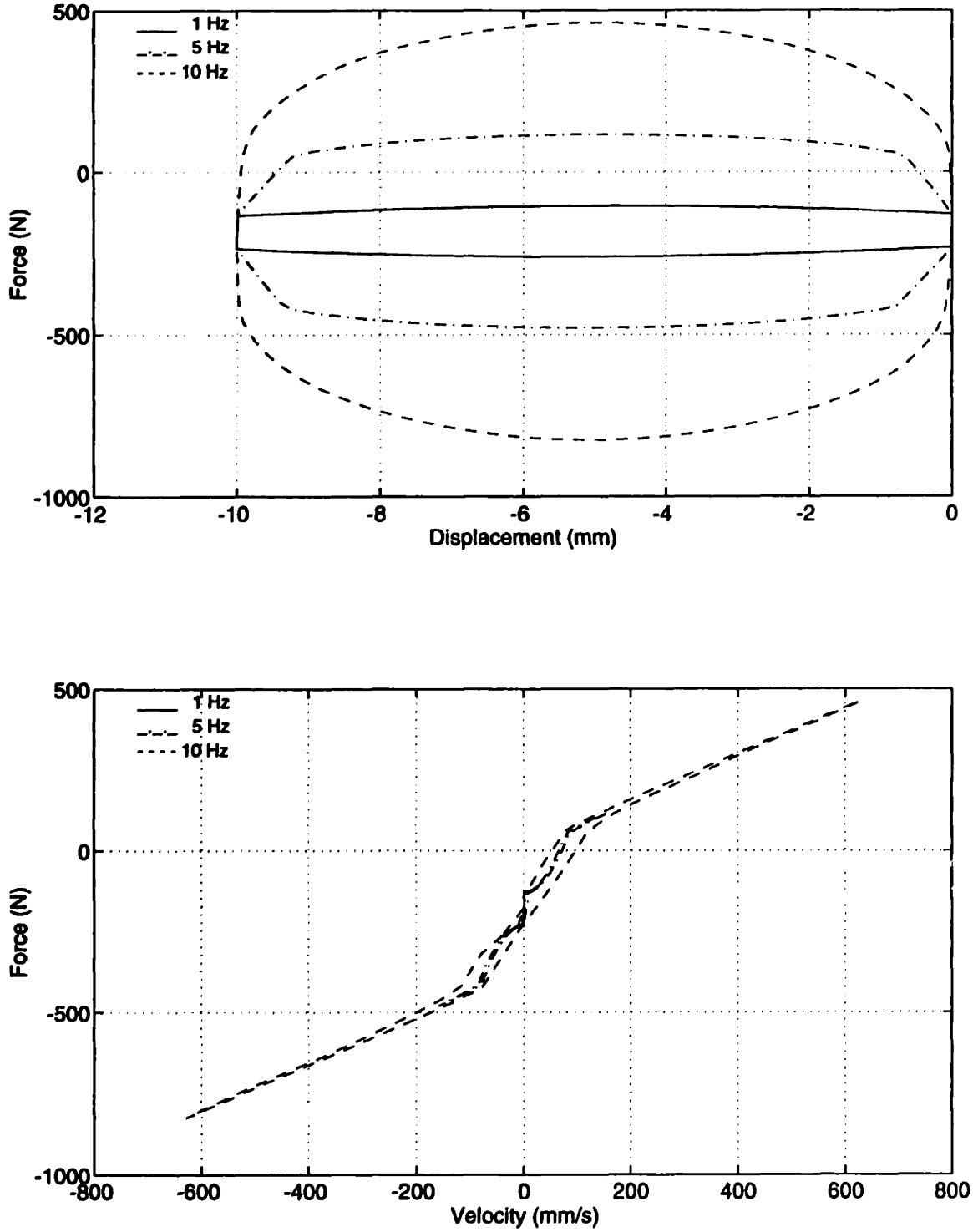

Figure 3.20: Force-displacement and force-velocity diagrams ($X_{max} = \pm 5$mm at $1, 5, 10$Hz)

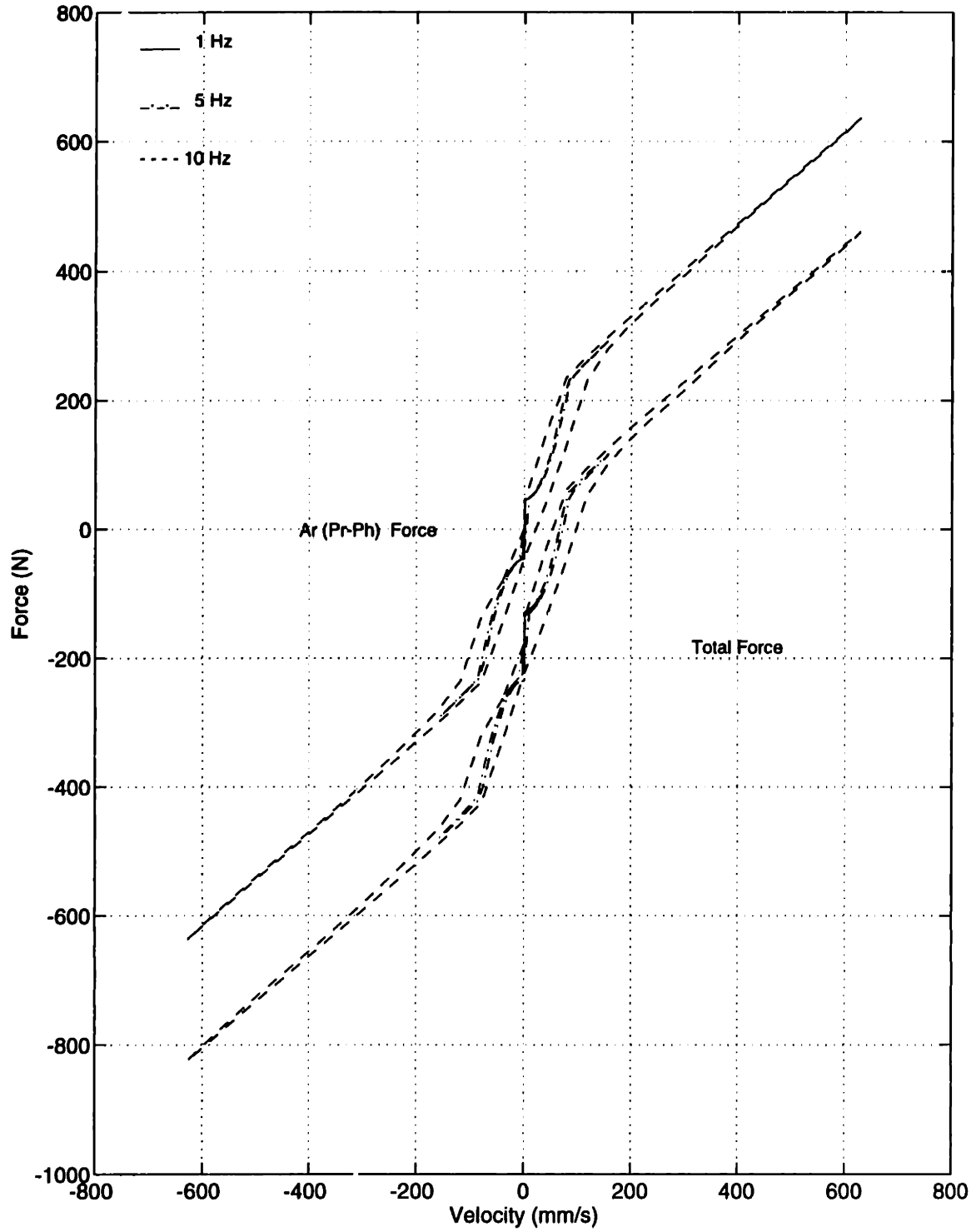

Figure 3.21: Force(component)-velocity diagram ($X_{max} = \pm 5mm$ at $1, 5, 10$Hz)

frequencies in this case. However, the similarity between the component of force, $A_r(P_r - P_h)$, and the total force near zero velocity in Figure 3.21 appears to confirm the assumption that the hysteresis in this region is in part related to the displacement due to compression of the gas volume.

3.2.4 Entrained Air

Simulations where run to show the effect of entrained air as bubbles on the dynamic performance of the shock absorber. The maximum velocity and frequency are held constant as the amount of air by volume at equilibrium is increased.

At $100\frac{mm}{s}$ and 5Hz, the addition of $5-10\%$ air in the hydraulic fluid had the effect of increasing the hysteresis everywhere in the force-velocity plane and skewing the characteristic force-displacement hysteresis slightly (see Figure 3.22 and 3.23). The air in the fluid creates barely perceptable additional lags in the pressure responses as observed in Figure 3.24. Figures 3.25, 3.26, and 3.27 at $500\frac{mm}{s}$ and 10Hz indicate comparable trends with the loss of the distinct regions of hysteresis in the force-velocity plane. Because air has the effect of decreasing the effective bulk modulus of the fluid, the observed effect on both the force-velocity and force-displacement planes are attributable to increases in the compressiblity of the fluid.

3.2.5 Check Valve Preload

The check valve preload is a source of hysteresis in this monotube design because the only flow across the piston when the pressure difference across the piston is low enough that both the rebound and compression check valves are closed is the leakage flow around the piston which is very small by comparison. The check valve preload is reduced to demonstrate the effect on the hysteresis characteristics of the shock absorber.

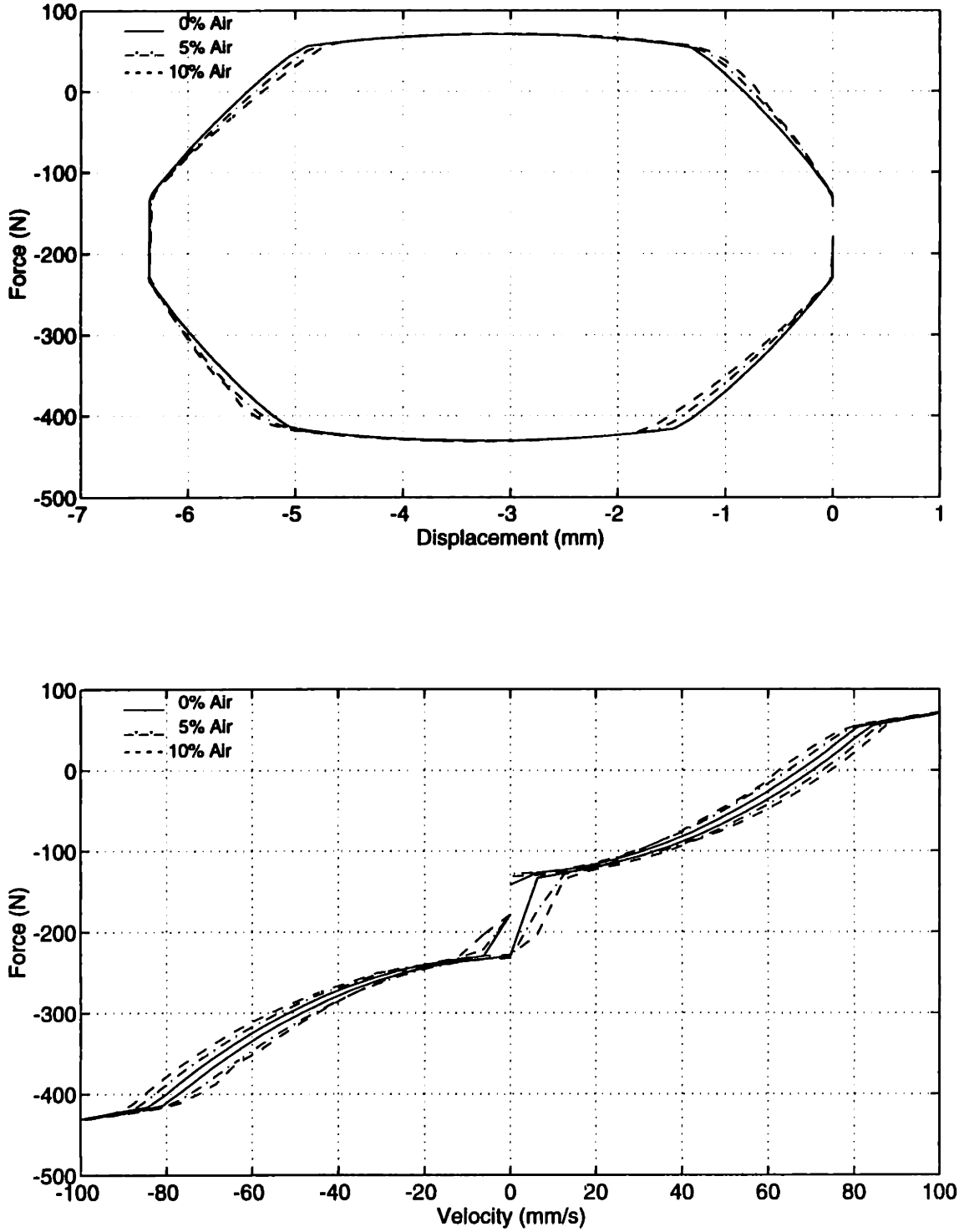

Figure 3.22: Entrained air: Force-displacement and force-velocity diagrams ($V_{max} = 100\frac{mm}{s}$ at 5Hz)

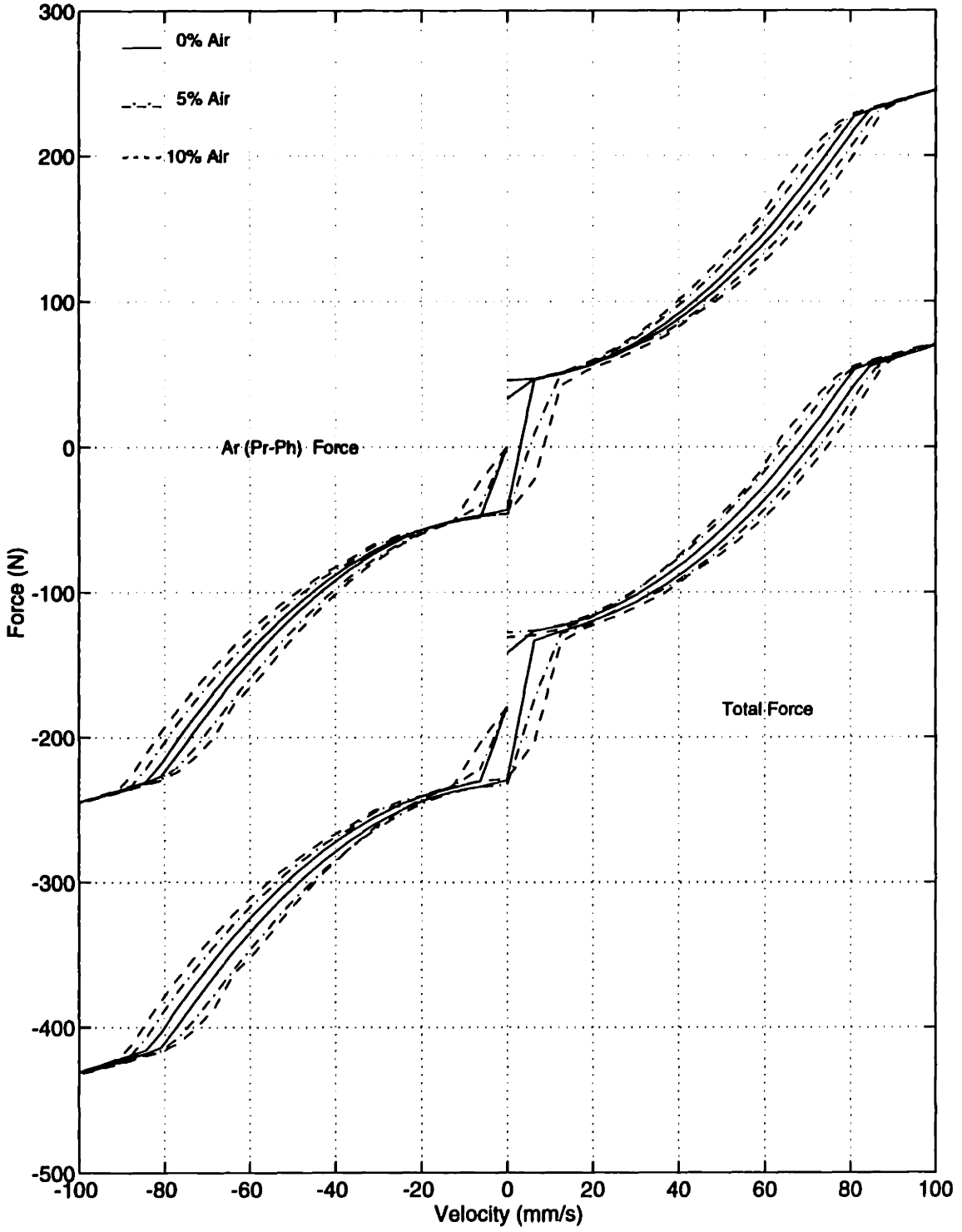

Figure 3.23: Entrained air: Force(component)-velocity diagram ($V_{max} = 100\frac{mm}{s}$ at 5Hz)

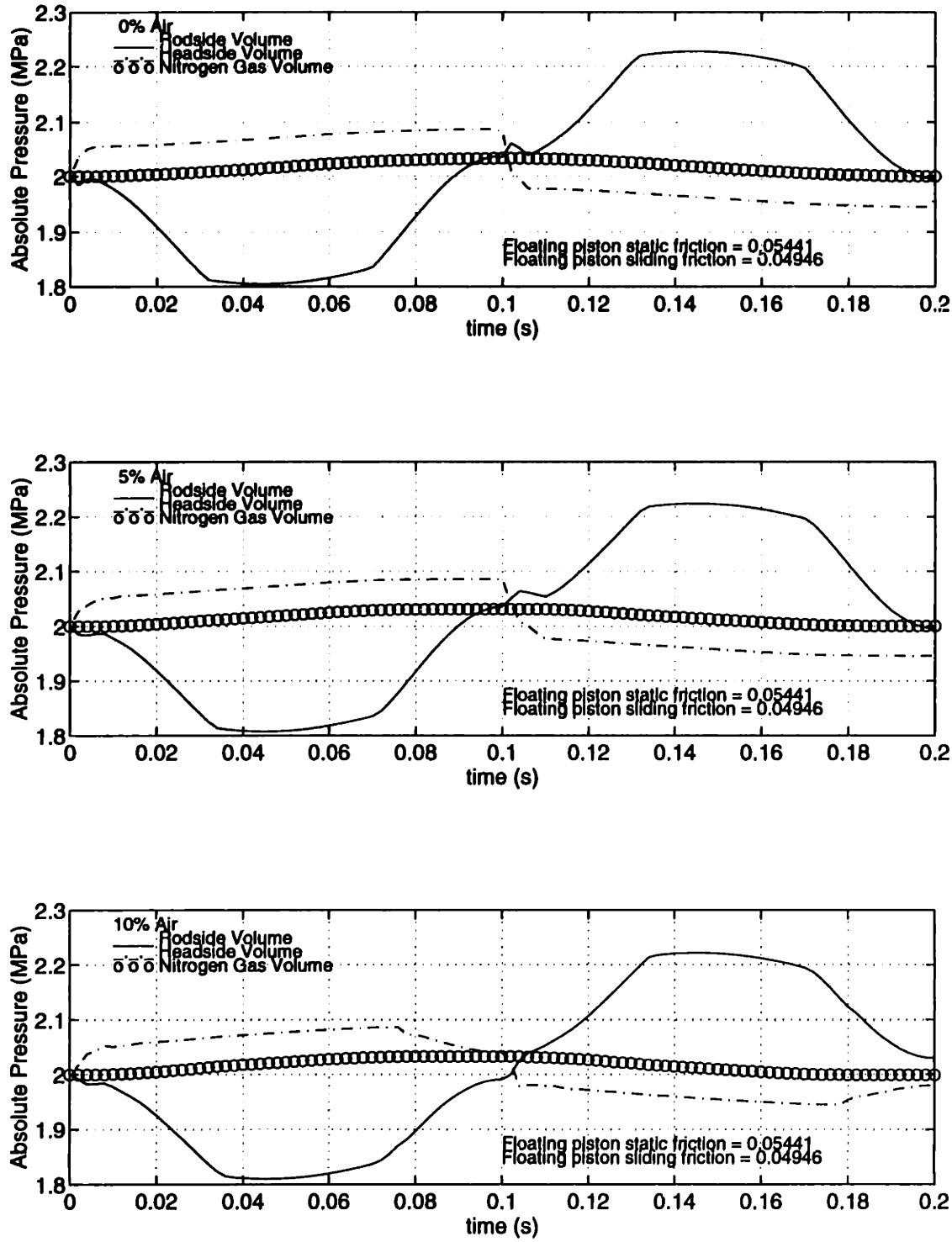

Figure 3.24: Entrained air: Rodside, headside, and gas pressures ($V_{max} = 100\frac{mm}{s}$ at 5Hz)

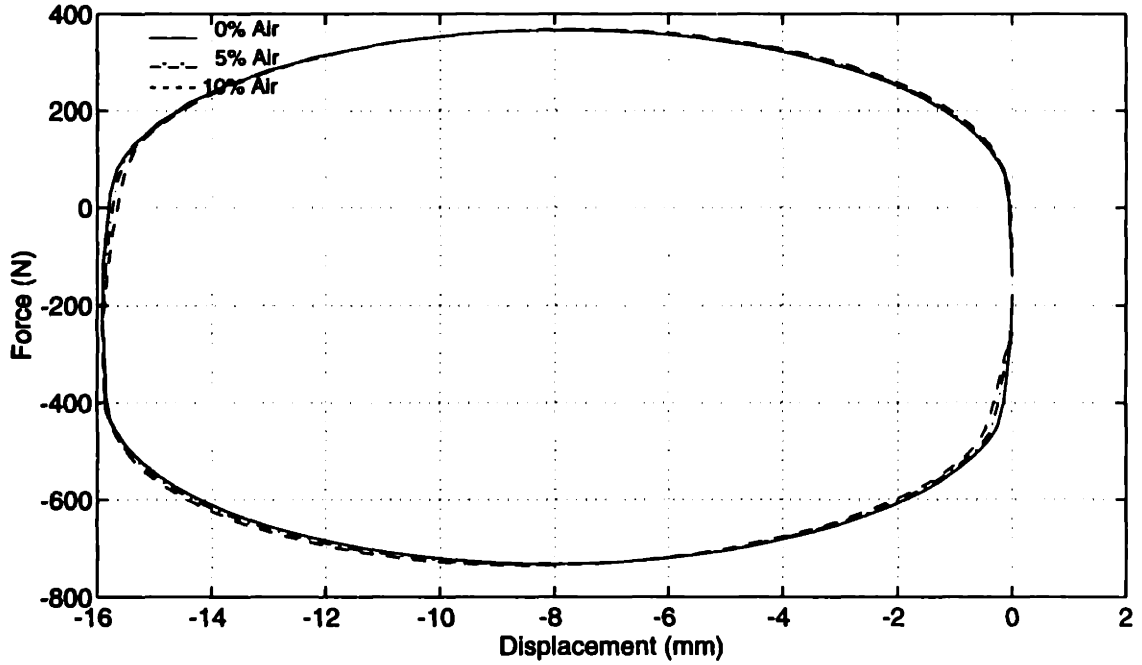

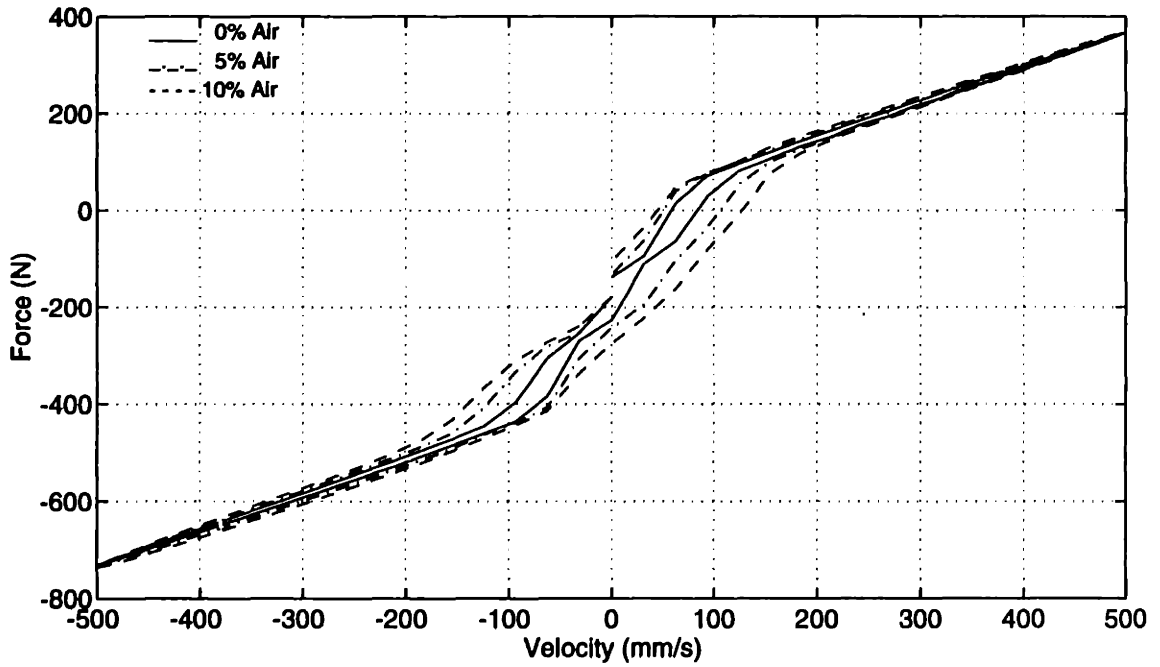

Figure 3.25: Entrained air: Force-displacement and force-velocity diagrams ($V_{max} = 500\frac{mm}{s}$ at 10Hz)

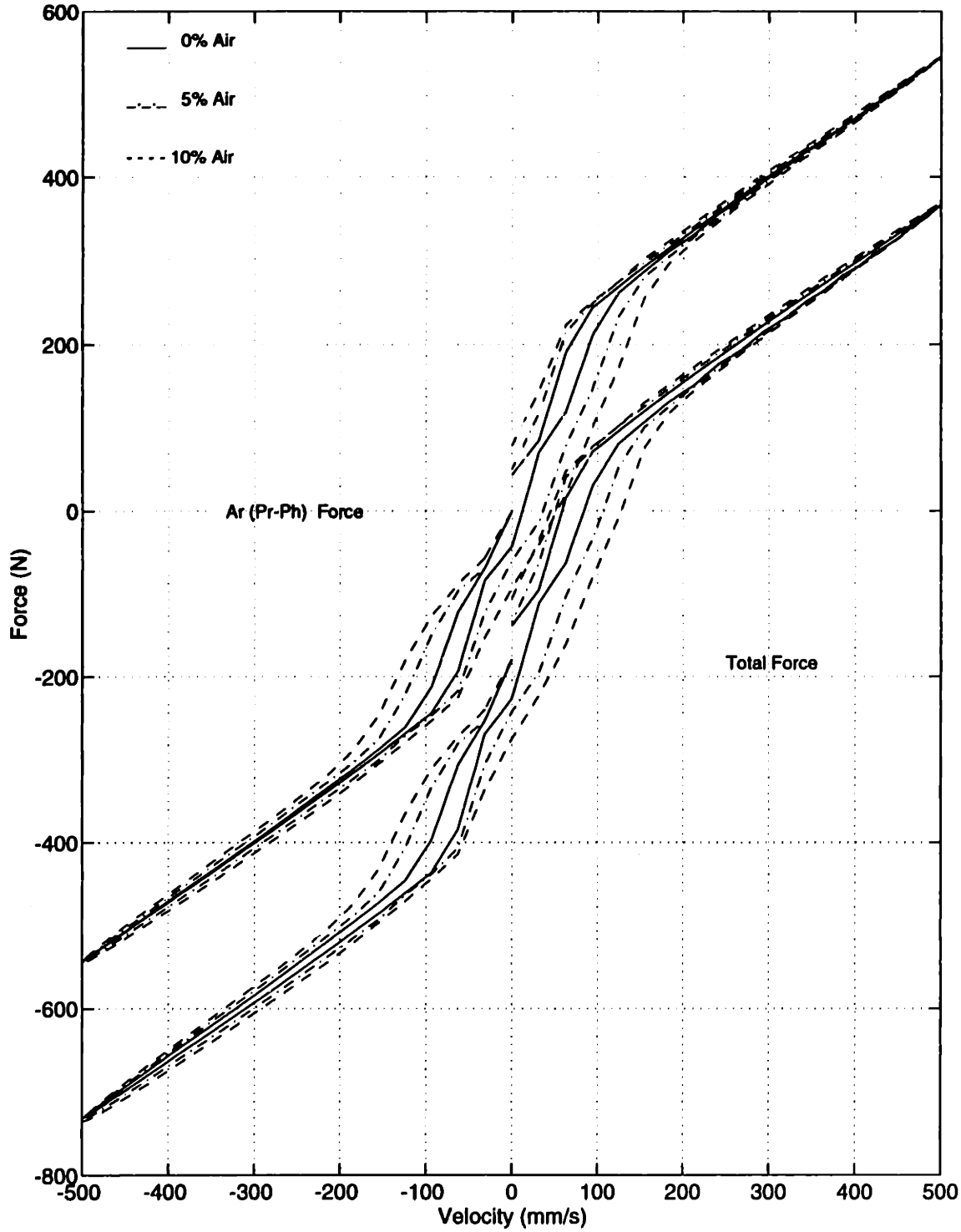

Figure 3.26: Entrained air: Force(component)-velocity diagram ($V_{max} = 500\frac{mm}{s}$ at 10Hz)

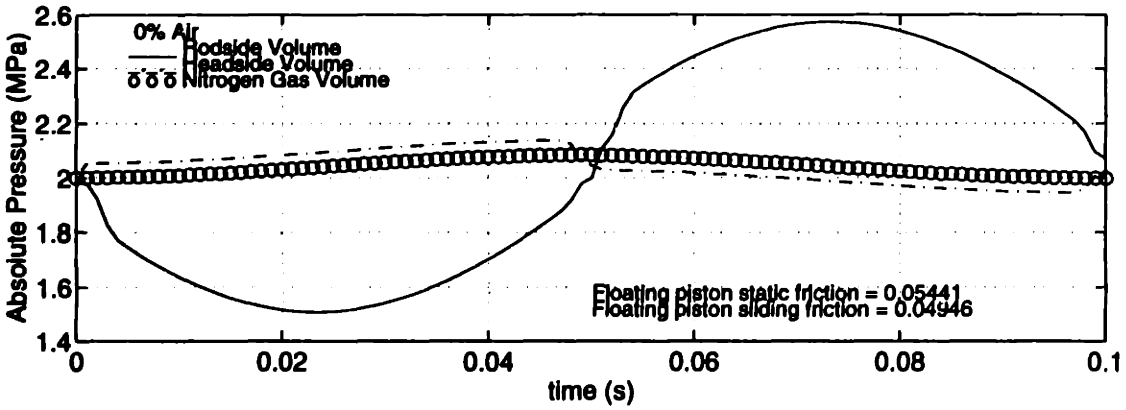

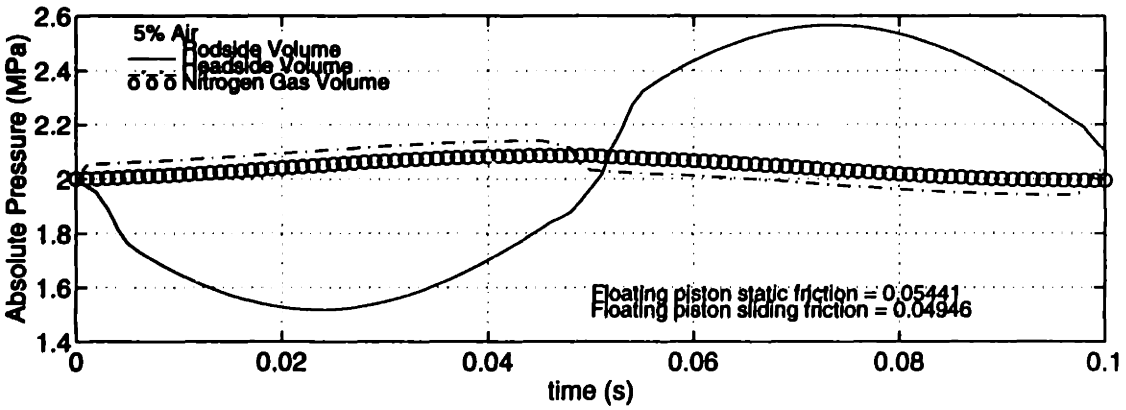

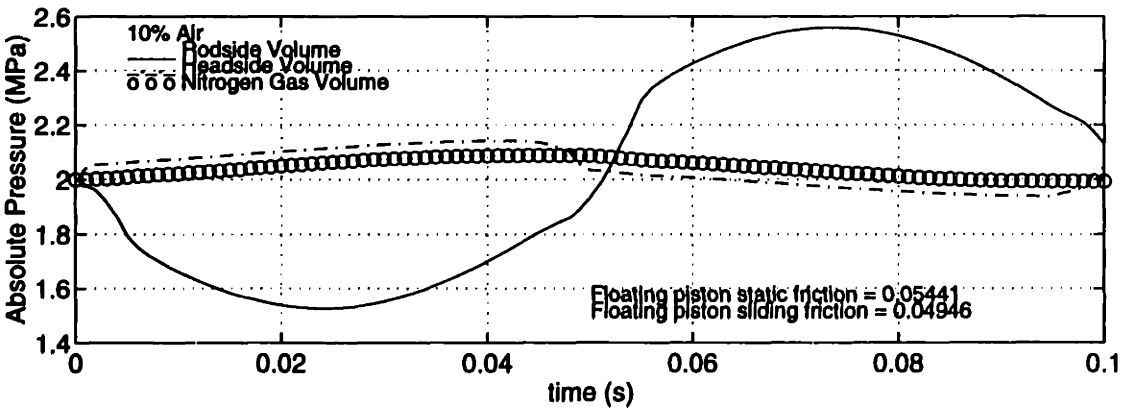

Figure 3.27: Entrained air: Rodside, headside, and gas pressures ($V_{max} = 500\frac{mm}{s}$ at 10Hz)

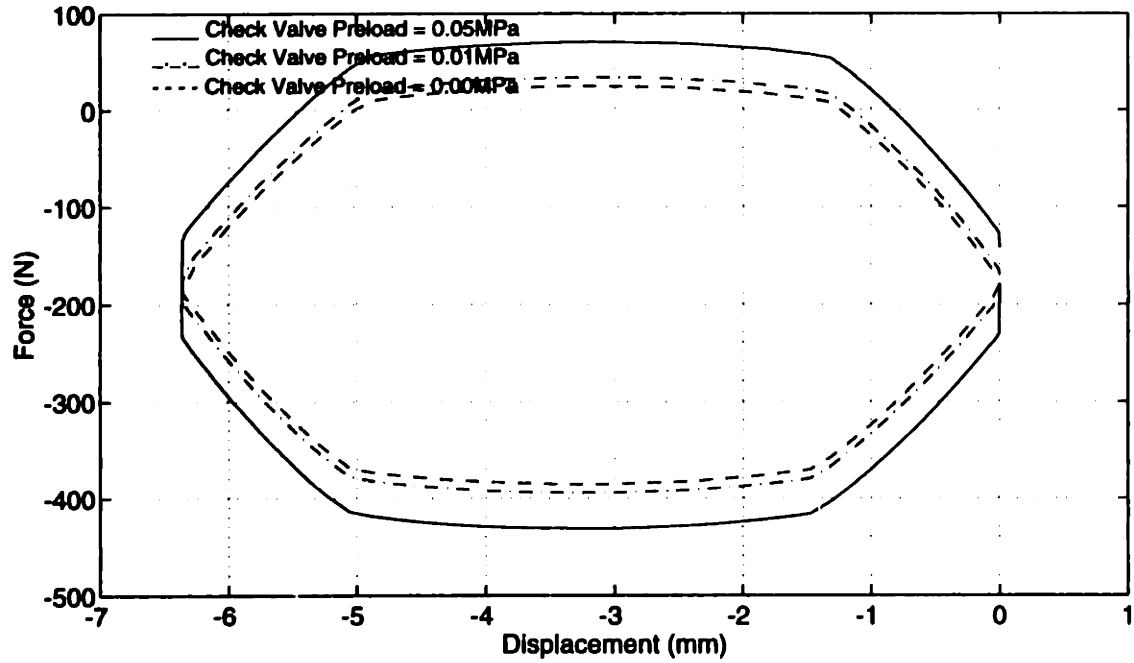

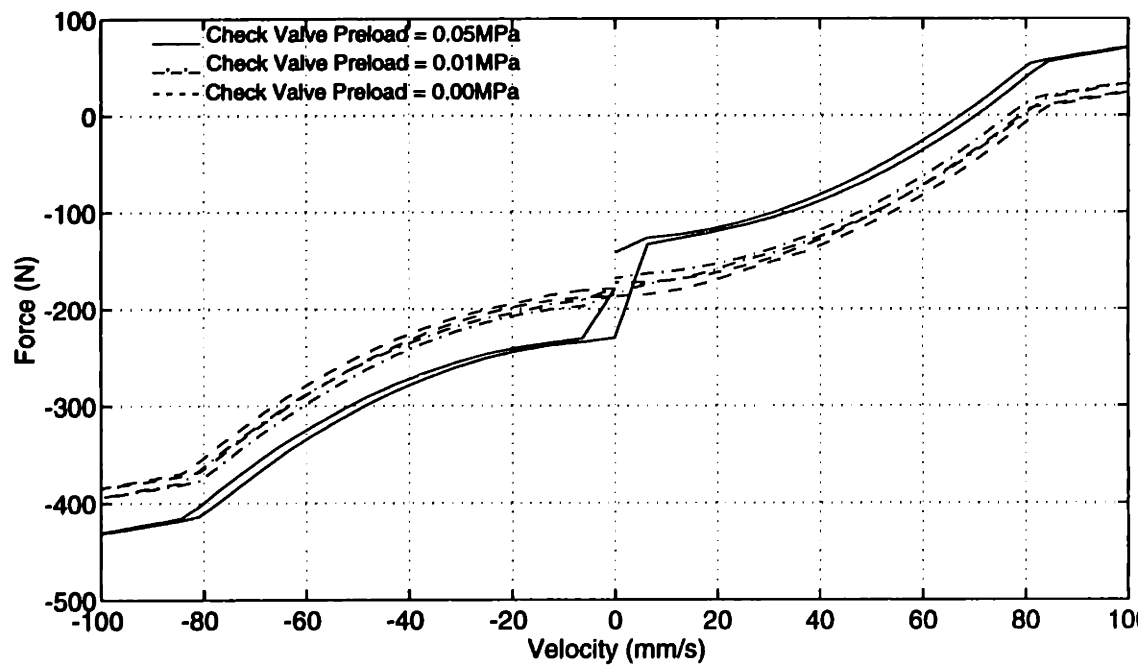

Figure 3.28: Check valve preload: Force-displacement and force-velocity diagrams ($V_{max} = 100\frac{mm}{s}$ at 5Hz)

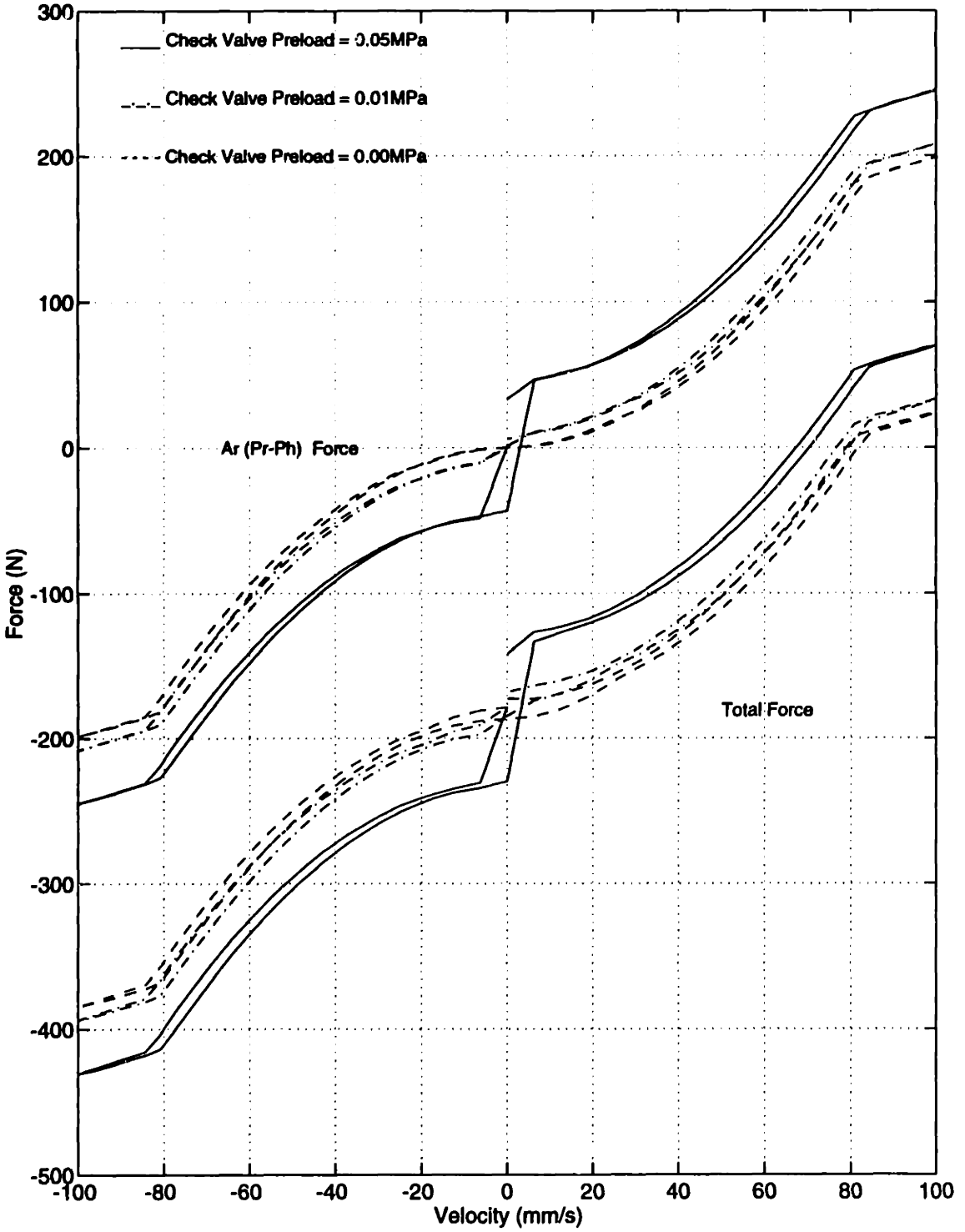

Figure 3.29: Check valve preload: Force(component)-velocity diagram (V_{max} = $100\frac{mm}{s}$ at 5Hz)

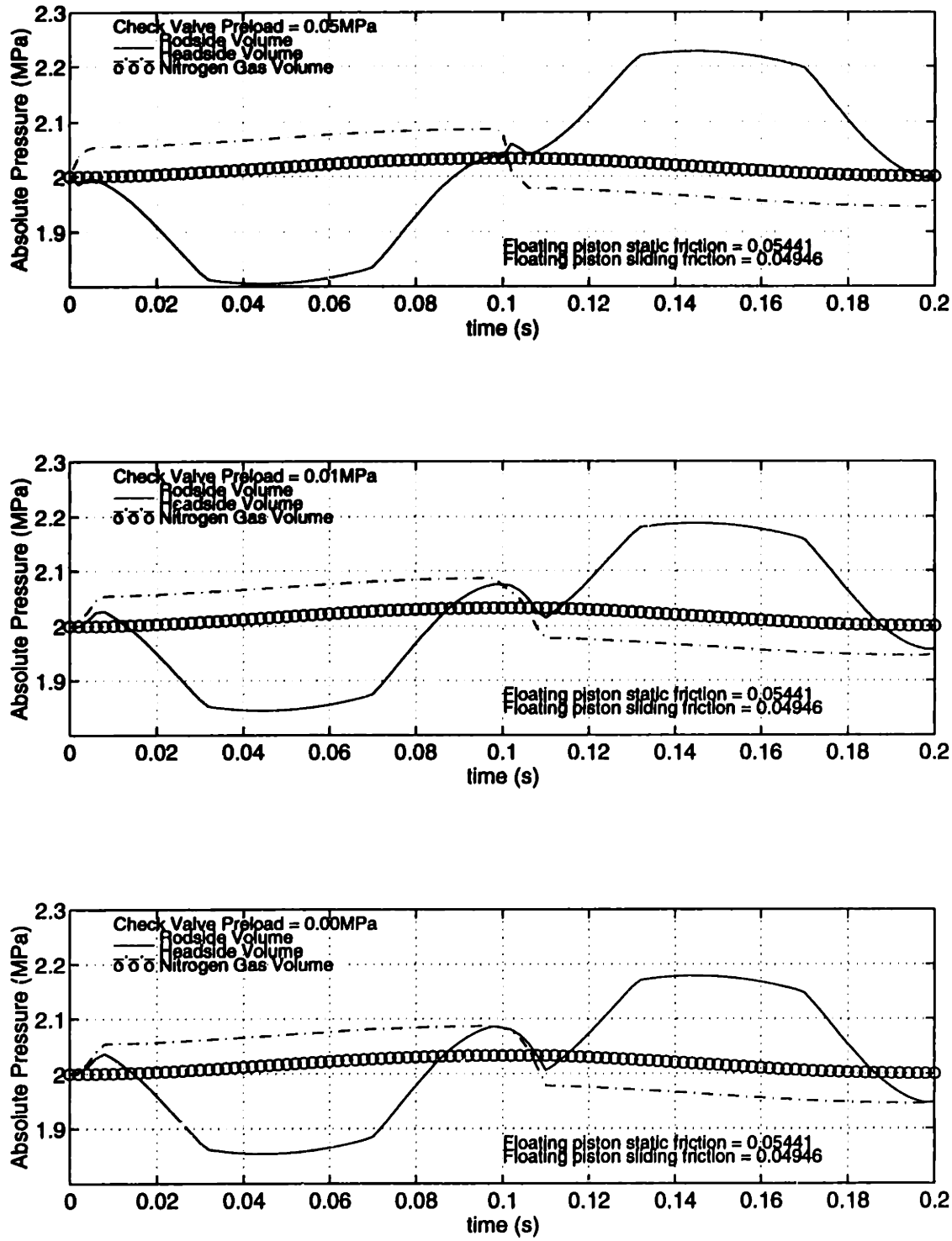

Figure 3.30: Check valve preload: Rodside, headside, and gas pressures ($V_{max} = 100\frac{mm}{s}$ at 5Hz)

Figures 3.28 and 3.29 show that at $100\frac{mm}{s}$ and 5Hz the hysteresis near zero velocity can be reduced to a very small amount. As the check valve preload is reduced, the hysteresis near zero velocity goes to zero for the $A_r(P_r - P_h)$ force while the total force has some remaining hysteresis due to the friction on the floating piston. From Figure 3.30, it is possible to see that friction produces a pressure difference across the floating piston approximately equal to that required to overcome the static friction. The headside volume at the end of the cycle is at a pressure lower than the initial condition pressure of the gas volume by the amount required to offset the floating piston static friction, thereby, eliminating the hysteresis due to the check valve. The check valve without a preload allows the pressures across the piston to equilibrate across the piston (not the floating piston) near zero velocity at the middle and end of the cycle.

3.2.6 Gas Chamber Pressure

The equilibrium pressure of the nitrogen gas was varied from 20bar down to 5bar in order to understand the influence of this pressure on the dynamic response. In Figure 3.31, the hysteresis at $500\frac{mm}{s}$ and 10Hz in the force-displacement plane is not affected significantly accept for the area where the fluid on the rodside volume cavitates for the 5bar case. The cavitation manifests itself on the force-displacement plane as a flattened area where the load does not increase much between -8 and -6mm. On the force displacement plane the cavitation, results in a flattened area near the minimum velocity for the 5bar case. Figure 3.32 shows the cavitation effect for this case as the rodside pressure drops to the vapor pressure of the fluid (estimated to be 0MPa) but no further as the compliance for the fluid on that side of the piston effectively becomes infinite. Note, this result is not surprising as it is the high gas pressures which prevent the onset of cavitiation in monotube shock absorbers. The tolerance to cavitation is

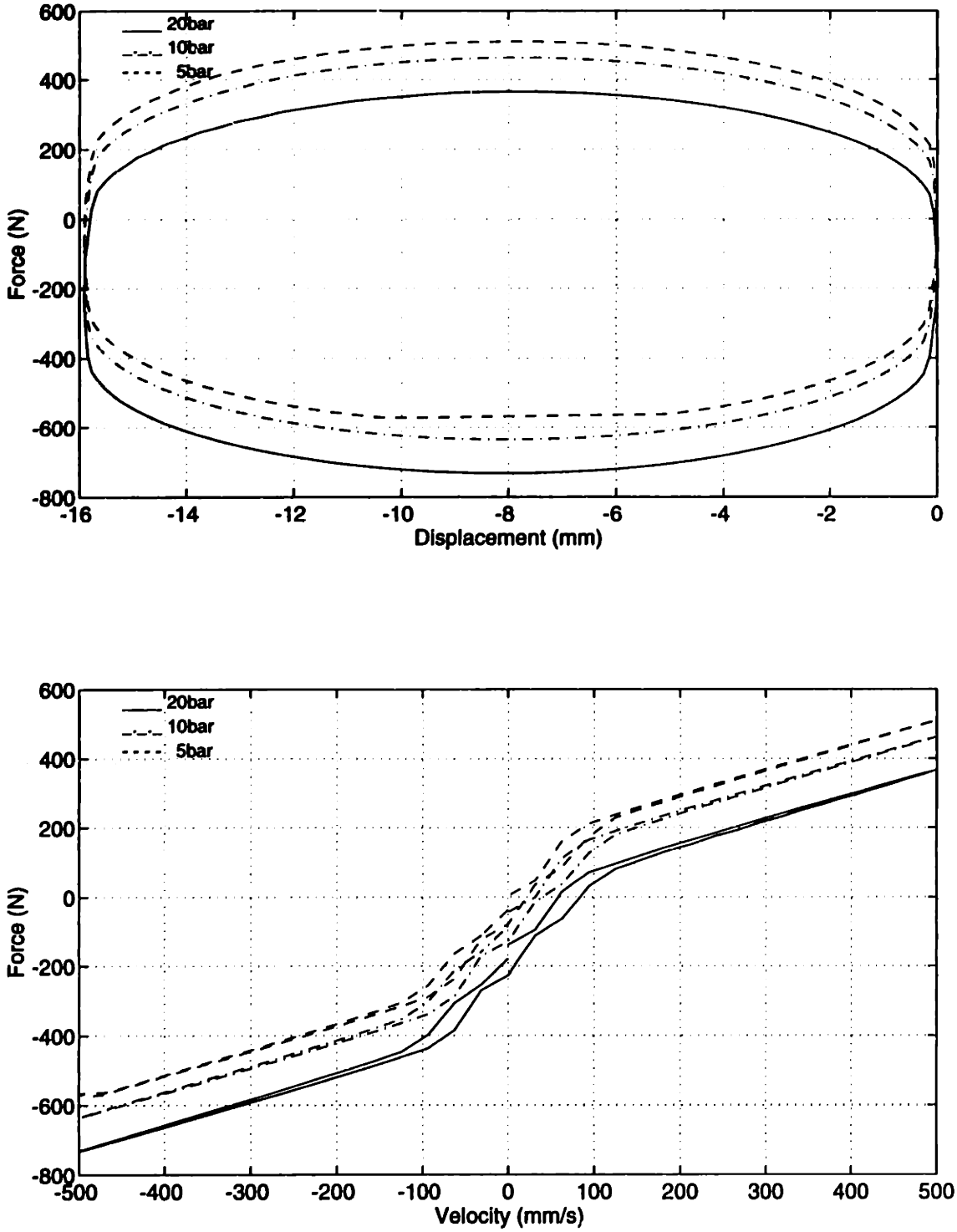

Figure 3.31: Gas equilibrium pressure: Force-displacement and force-velocity diagrams ($V_{max} = 500\frac{mm}{s}$ at 10Hz)

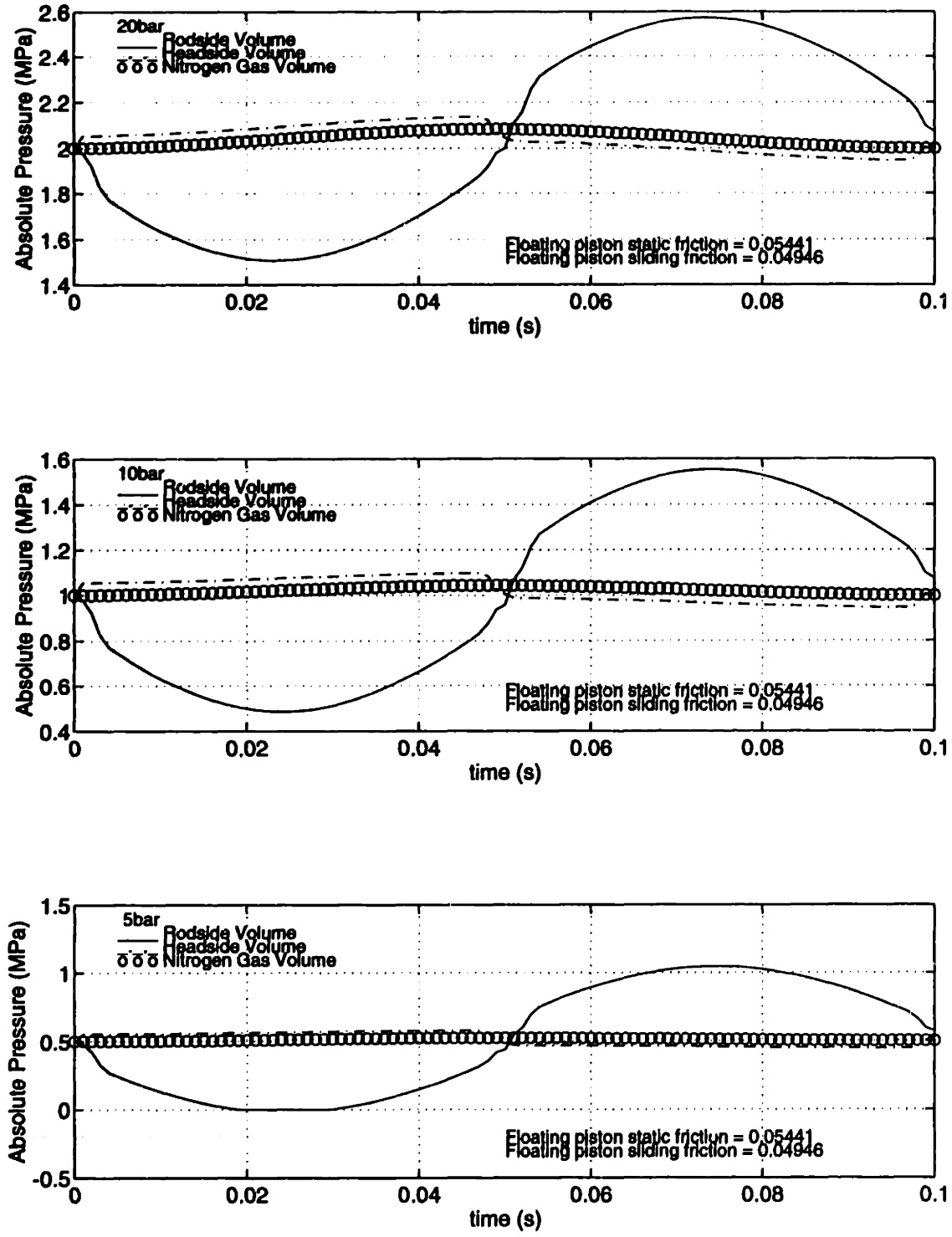

Figure 3.32: Gas equilibrium pressure: Rodside, headside, and gas pressures ($V_{max} = 500\frac{mm}{s}$ at 10Hz)

a principal advantage of the design over the dualtube design. For example, cavitation occurred for a nominal gas pressure of 20bar under extreme conditions such as ±5mm amplitude at 75Hz ($2356\frac{mm}{s}$ peak velocity). The reduction in gas pressure did not significantly effect the hysteresis for the 10Hz case presented here.

3.2.7 Floating Piston Friction

The most numerically stable characteristic for the friction acting on the floating piston was to have a relatively constant friction force with floating piston-to-tube relative velocity. As a result, the friction effects which could be most reliably characterized were those where the overall amount of friction was varied. Increasing the friction by a factor of 2 resulted in a slight increase in hysteresis on the force-displacement plane due to the additional frictional losses and an increase in hysteresis on the force-velocity plane near zero velocity with lesser effects on hysteresis at higher velocities (see Figures 3.33 and 3.34). At higher velocities the output force was more uniformly larger for higher friction on the floating piston. This resulted from an increase in rodside pressure, as well as headside pressure, during the compression stroke to offset the friction and a reduction in these pressures during the rebound stroke.

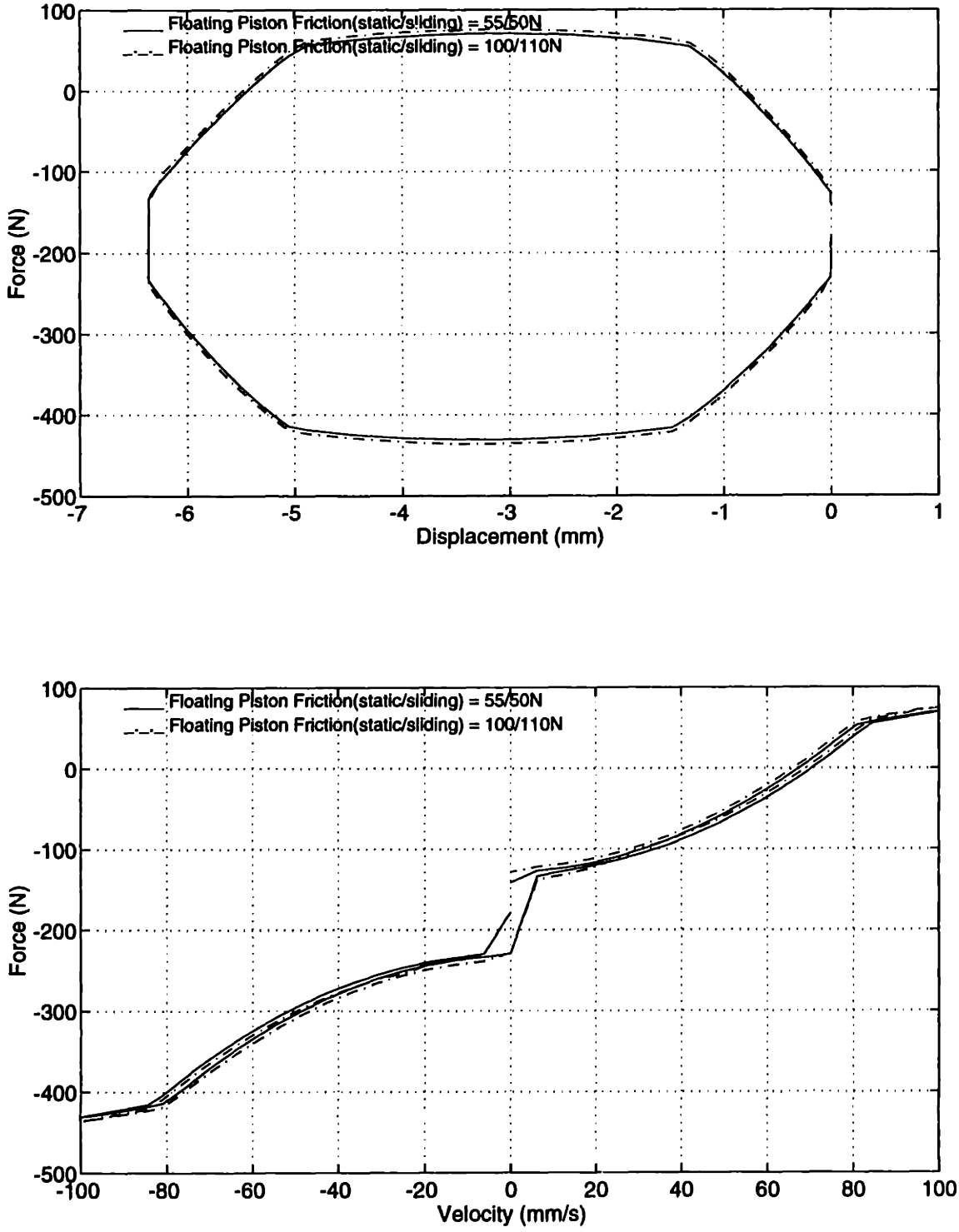

Figure 3.33: Floating piston friction: Force-displacement and force-velocity diagrams ($V_{max} = 100\frac{mm}{s}$ at 5Hz)

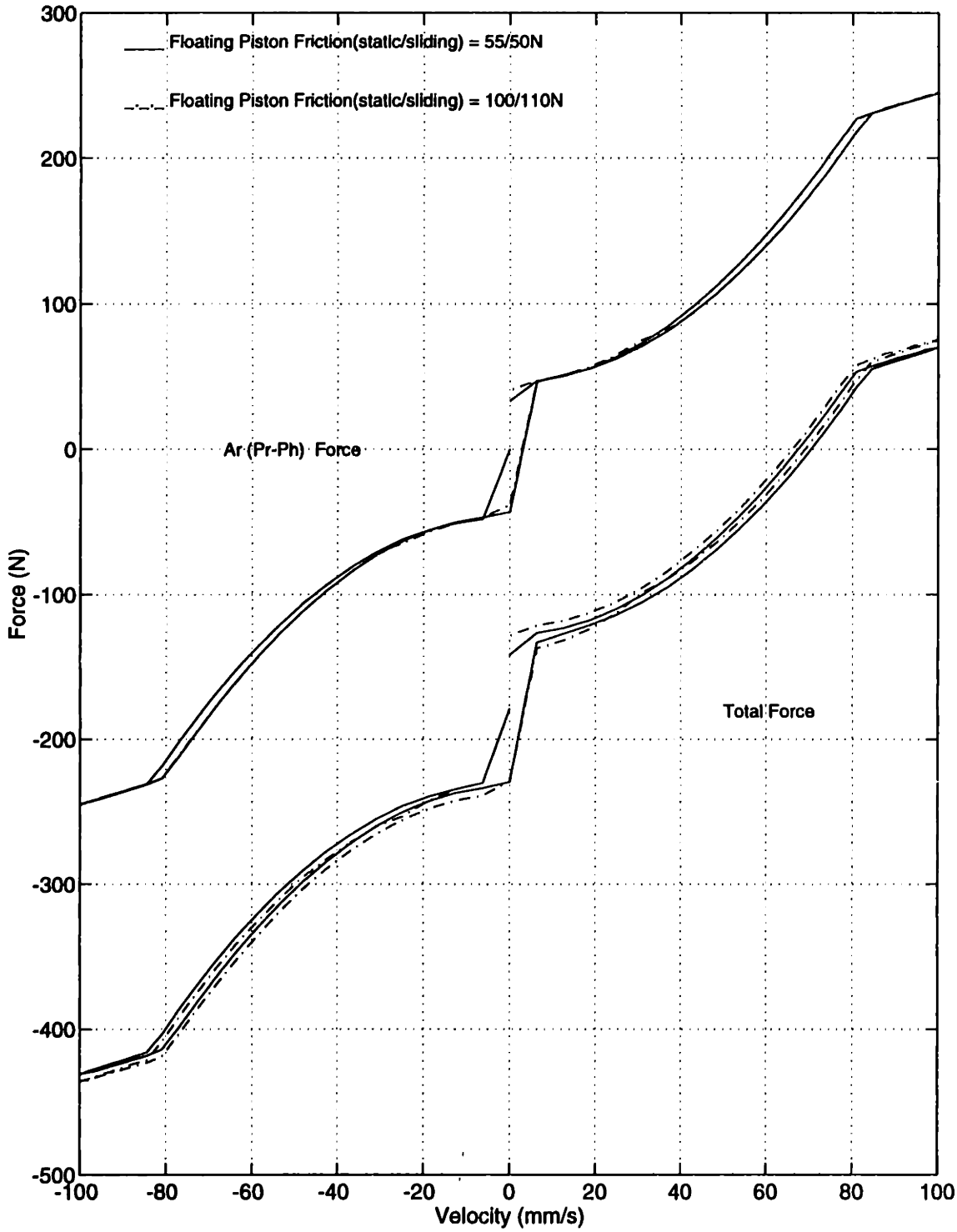

Figure 3.34: Floating piston friction: Force(component)-velocity diagram (V_{max} = $100\frac{mm}{s}$ at 5Hz)

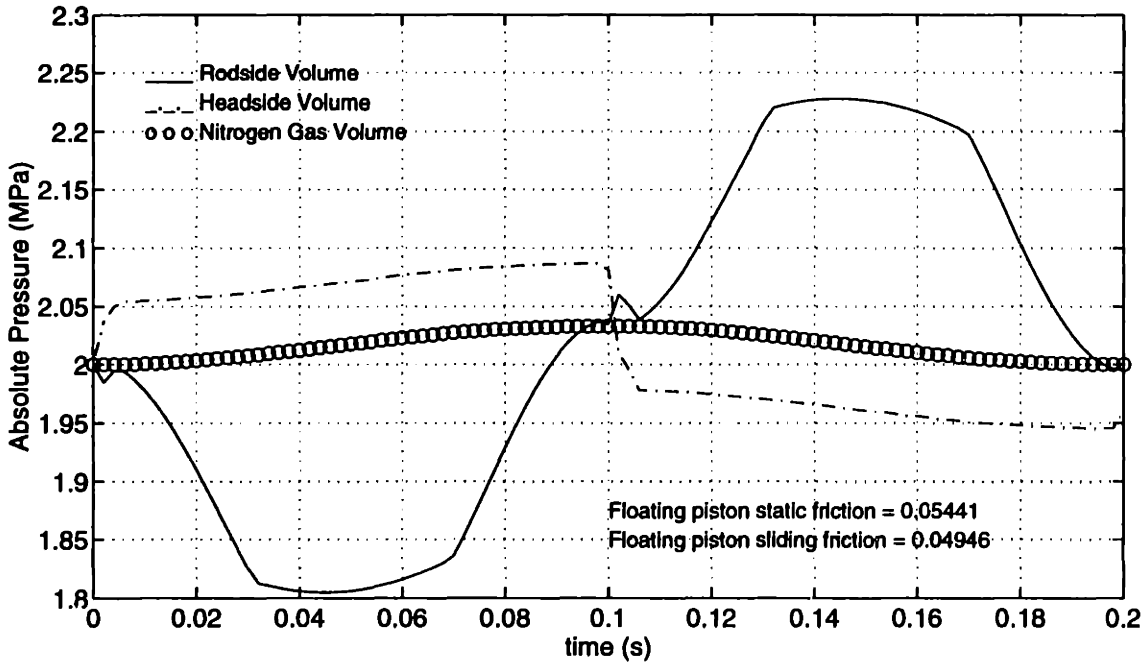

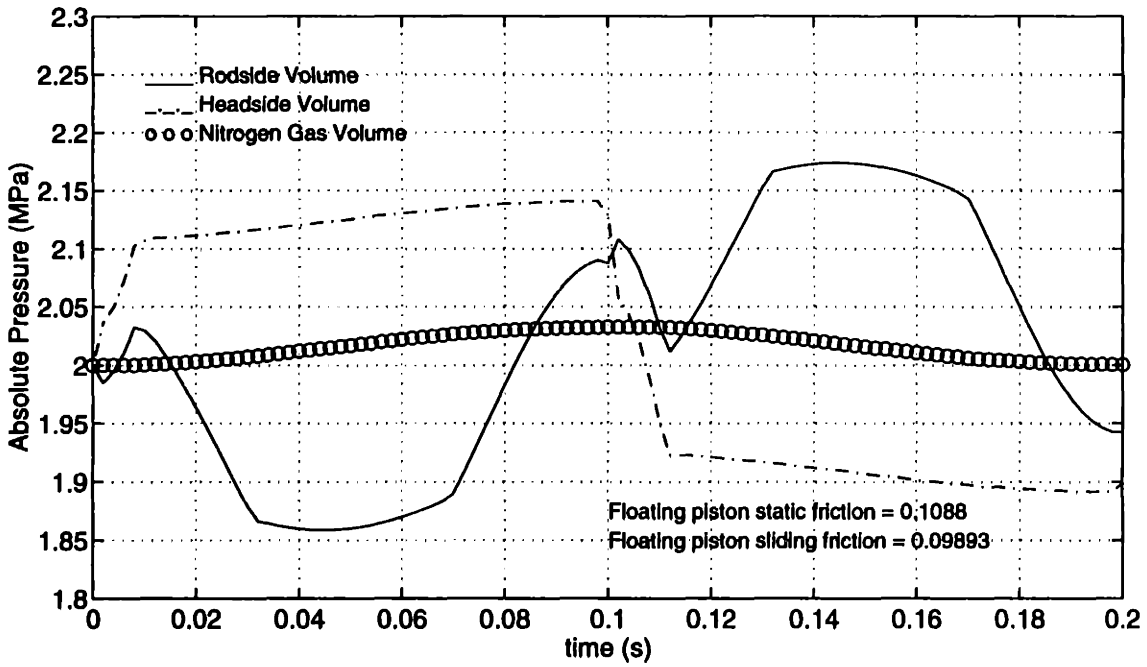

Figure 3.35: Floating piston friction: Rodside, headside, and gas pressures ($V_{max} = 100\frac{mm}{s}$ at 5Hz)

Chapter 4
Hysteresis Models and Simulations

4.1 Capacitive and Resistive Element Interaction

Hysteresis occurs in the force-displacement trace of a shock absorber due to the damping elements. The damping occurs principally as a results of losses in potential energy (in the form of static pressure) from resistive elements. The reasons for hysteresis in the force-velocity plane are, generically, the capacitive elements of the fluid volumes on either side of the piston. In a monotube, the compliance of the nitrogen gas volume also has an effect.

4.2 Simplified Shock Absorber Model

The resistive and capacitive elements interact to produce both the hysteresis in the force-displacement and force-velocity planes. Two models are derived to illustrate this interaction. These models are based on simplified models of shock absorbers. Because the output force is based directly on the pressure difference across the piston, the state equations for this pressure will be used to infer the dynamic characteristics of the shock absorber. If the leakage flow across the piston is neglected, Eqn. (2.60) for the rodside pressure reduces to the flow due to the relative velocity of the piston and tube minus the flow into the volume all over the effective compliance of the volume. The flow due to the relative velocities of the piston and tube can be viewed as the input. The flow into the volume is what comes across to it from the headside volume

and is determined by the restrictions in the piston for an applied pressure difference.

$$\dot{P} = \frac{Q_S - Q_R(\Delta P)}{C} \tag{4.1}$$

The restrictions are the damping resistors which dissipate potential energy stored in the capacitive elements on either side of the piston. Equation 4.1 is the state equation for the capacitor with the constitutive equation of a fluid resistor in conductive causal form. Then the output of the shock absorber is in large part determined by the characteristics of an RC model.

4.2.1 Resistive Element Characteristics

Constitutive relationships for the resistor can be linear or nonlinear. A linear model would be comparable to the leakage model of Eqn. (2.49) neglecting the flow due to the relative motion of the piston and tube. A quadratic model would be comparable to that defined by the orifice equation (Eqn. (2.91)) for a constant discharge coefficient. Another nonlinear model of a resistive element would be that of Coulomb friction such as that derived for the floating piston model (Eqn. (2.149)). The constitutive relationships in resistive causal form are

$$P_{Rlinear} = RQ_R \tag{4.2}$$

$$P_{Rquad} = RQ_R^2 \tag{4.3}$$

$$P_{Rcoul} = sign(Q_R)P_{Rmag}. \tag{4.4}$$

The characteristics for these three generalized resistive models are shown in Figure 4.1 for the case where flow (generalized velocity) is the input (i.e. resistive causality). The input and output to the elements are plotted versus time. The output effort is also plotted versus the input flow and displacement. The output is the effort generated by the resistor for a sinusoidal input flow of unity magnitude and period

$\frac{1}{4}$. The resistance used was also unity for the linear and quadratic models. Similar moments in time are denoted with the same symbols on all four plots. The effort is always in phase with the input flow. As a result, no hysteresis is evident when the output effort is plotted against the input flow. The portion of the curve lying in the first and third quadrants represents portions of the cycle when power flows into the resistor and is dissipated. These resistors never return power to the system and are represented in bond graph notation as 1-ports with constitutive relationships in the first and third quadrants of the effort-flow plane. The effort-displacement plot has hysteresis because of the 90^o phase shift between displacement and effort. The incremental energy dissipated by the resistor is the dot product of the effort and incremental displacement. Then the energy dissipated by any of the resistors is equal to the area enclosed by its trace on the effort-displacement plane.

4.2.2 Capacitive Element Characteristics

Three constitutive relationships for a capacitor model are investigated in the same way as for the resistive elements above. The linear model is comparable to that of a linearly elastic spring element. A spring with backlash is comparable to that resulting from an initial gap between two elastic members such that there is no force generated until the gap is closed. An example of this is the backlash between two gears. A second nonlinear model would be a spring which remains linear until the effort "yields" the spring plastically. An obvious example of this would be a tensile test specimen which is yielded plastically. However, in this case there is no residual displacement when the load is removed because there is no dissipative element. Another example is a simplified version of the cavitation model used in this thesis. In the cavitation model, the compliance of the fluid volume effectively is infinite (zero stiffness) once the pressure drops to the vapor pressure. The constitutive relationships in integral

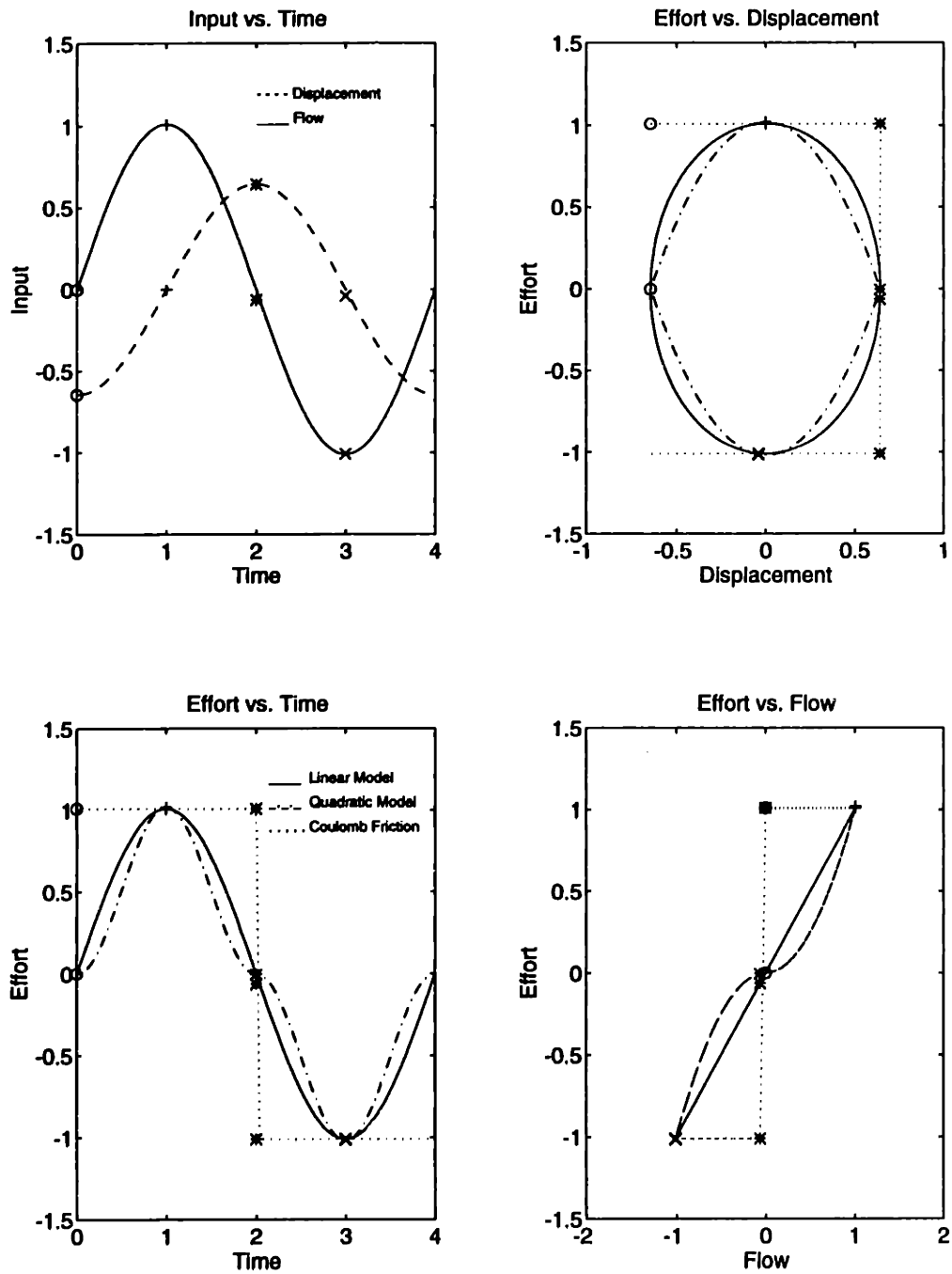

Figure 4.1: Constitutive relationships for resistor in resistive causality

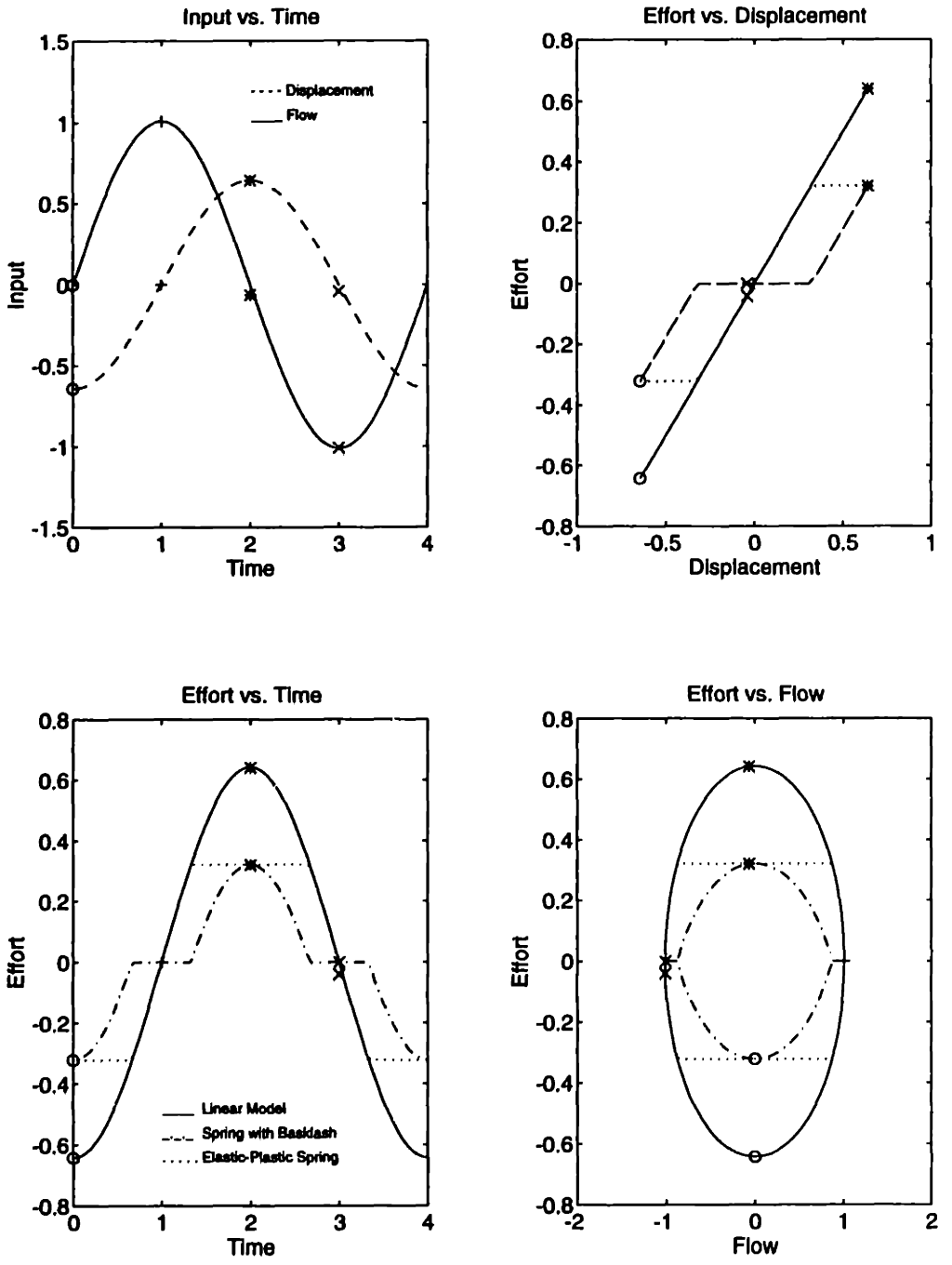

Figure 4.2: Constitutive relationships for capacitor in integral causality

causality form are

$$\dot{P}_{Clinear} = \frac{Q_S}{C} \tag{4.5}$$

$$\dot{P}_{Cgap} = \begin{cases} \frac{Q_S}{C} & \text{for } |\int Q_S dt| \geq X_{gap} \\ 0 & \text{for } |\int Q_S dt| < X_{gap} \end{cases} \tag{4.6}$$

$$\dot{P}_{Ce-p} = \begin{cases} \frac{Q_S}{C} & \text{for } |P_{Ce-p}| < P_p \\ 0 & \text{for } |P_{Ce-p}| \geq P_p. \end{cases} \tag{4.7}$$

The constitutive relationships for these capacitor models are demonstrated in Figure 4.2 for the case where flow (generalized velocity) is the input (i.e. integral causality). The output is the effort generated by the capacitor for a sinusoidal input flow of unity magnitude and period $\frac{1}{4}$. The compliance used was unity for all models with equally arbitrary values selected for the gap displacement of the spring with backlash model and the effort at which the "elastic limit" of the elastic-plastic capacitor is achieved. Notice the effort is in-phase with the integral of the input flow (displacement). Consequently, no hysteresis is evident in the effort-displacement plane. The portion of the curve lying in the first and third quadrants represents portions of the cycle when potential energy is maintained by the capacitor. Potential energy is returned to the environment when the capacitor is displaced toward the origin and stored by the capacitor as it is displaced further from the origin. These capacitors store potential energy in the first and third quadrant and release potential energy in the second and fourth quadrants of the effort-flow plane. The effort-flow plot has hysteresis because of the 90^o phase shift between flow and effort.

4.2.3 RC Model of Shock Absorber

A simple model consisting of the fundamental elements of a shock absorber is shown in Figure 4.3. Note that the piston rod extends through both sides of the cylinder and there is no gas capacitor. As a result, this model is roughly analogous to a simple dualtube shock absorber where the requirement for a reserve chamber has

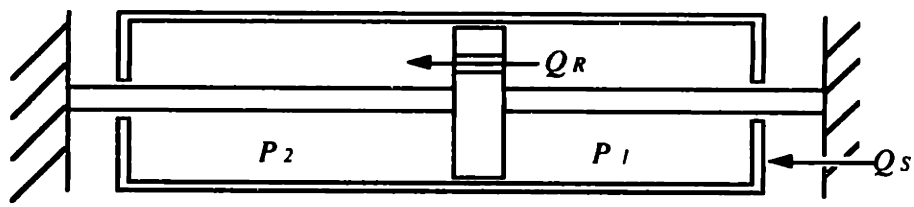

Figure 4.3: Simple dualtube RC model

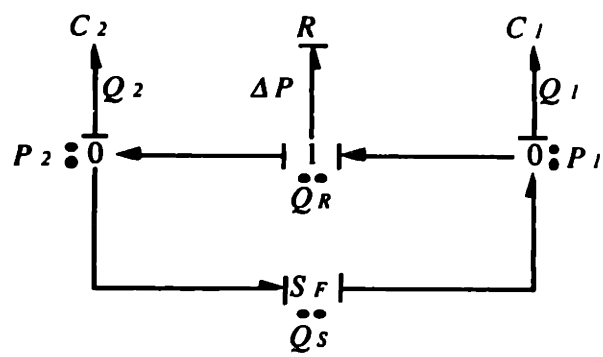

Figure 4.4: Bond graph for simple dualtube RC model

been relaxed due to the piston rod extending through the body of the shock. The bond graph for this model consists of the fluid capacitors on either side of the piston and the single orifice resistor porting flow across the piston between the capacitors. The input will be the equivalent flow in the fluid domain due to the relative motion between the piston and the tube. There is no need for a transformer between the mechanical and fluid domains because the areas on either side of the piston are the same. As a result, we can look at the relationship between the input flow and output effort (pressure difference across the piston) strickly in the fluid domain from the

bond graph of Figure 4.4.

A simple model of a monotube shock absorber will be derived next. The model is shown in Figure 4.5 with the accompaning bond graph in Figure 4.6. A monotube replaces the reserve chamber with a nitrogen-filled chamber. This is modelled as a second compliance on one side of the piston. The floating piston separating the gas is idealized as massless and frictionless. As a result, the pressure on either side of the floating piston is always identical. The monotube model will have a piston with unequal areas in order that the difference in effective flows enters or exists the gas volume.

For both the dualtube and monotube models, the state equations for the pressures on either side of the piston are simply

$$\dot{P}_1 = \frac{\frac{A_1}{A_2}Q_S - Q_R - Q_g}{C_1} \tag{4.8}$$

$$\dot{P}_2 = \frac{-Q_S + Q_R}{C_2} \tag{4.9}$$

where the compliance can be a nonlinear function of displacement and/or effort and

$$Q_g = \begin{cases} 0 & \text{for dualtube case} \\ C_g\dot{P}_1 & \text{for monotube case.} \end{cases} \tag{4.10}$$

The area ratio is unity for the dualtube case in this simplified model. The constitutive law for the orifice flow in conductive causal form can be linear or nonlinear and is generally expressed by

$$Q_R = f(P_1 - P_2). \tag{4.11}$$

Two examples of each system will be investigated. An all linear example will be analyzed first to develop a general understanding of the behavior of the system. Then a model with nonlinear capacitor and resistor constitutive relationships will be investigated.

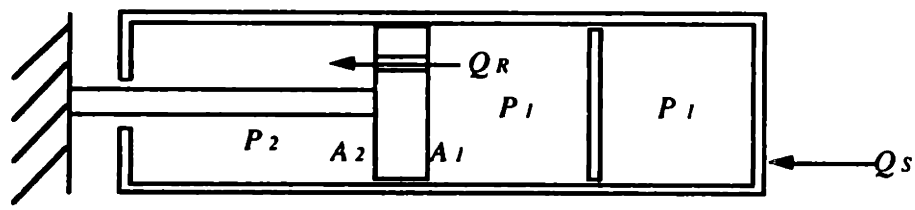

Figure 4.5: Simple monotube RC model

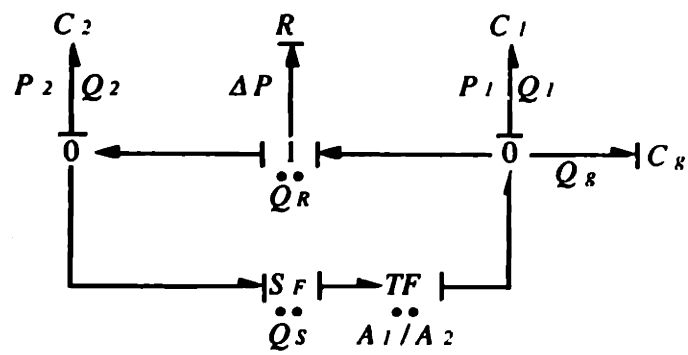

Figure 4.6: Bond graph for simple monotube RC model

The linear compliance model is equivalent to assuming the tube is rigid, the fluid is free of gas content, and the relative displacements are small. Combining the state equations into a single expression for the output effort results in the expressions

$$\Delta P = \begin{cases} \frac{Q_S - Q_R}{C_{eff}} & \text{for dualtube case} \\ \frac{1}{C_1 + C_g}\left(\frac{A_1}{A_2}Q_S - Q_R\right) + \frac{1}{C_2}\left(Q_S - Q_R\right) & \text{for monotube case.} \end{cases} \tag{4.12}$$

Note, that the effective compliance for the dualtube models is

$$\frac{1}{C_{eff}} = \frac{1}{C_1} + \frac{1}{C_2}. \tag{4.13}$$

The linear resistor model is comparable to the leakage model of Eqn. (2.49) as

described above and is then given by the conductive causal form of Eqn. (4.2).

$$Q_R = \frac{\Delta P}{R} \tag{4.14}$$

Combining Eqn. (4.14) with Eqn. (4.12) and computing the transfer function between the input flow and the output pressure difference for the dualtube model results in

$$\frac{\Delta P(s)}{Q_S} = \frac{R}{RC_{eff}s + 1} \tag{4.15}$$

where s is the Laplace complex variable. Notice a single state exists in actuality in this linear model because the compliances are dependent. The transfer function between the input displacement and the output pressure difference is

$$\frac{\Delta P(s)}{\frac{Q_S}{s}} = \frac{Rs}{RC_{eff}s + 1} \tag{4.16}$$

The phase of the transfer functions indicates that at very low frequencies ($s \rightarrow 0$) the effort is in-phase with the flow (velocity of the piston) and leads the displacement by 90^o indicating dominant resistive characteristics. As in Figure 4.1, hysteresis would appear in the effort-displacement plane and to a lesser degree in the effort-flow plane. At very high frequencies ($s \rightarrow \infty$), the effort is in-phase with the displacement of the piston and lags the flow by 90^o indicating the dominance of the capacitive element. The hysteresis would appear in the effort-flow plane and to a lesser degree in the effort-displacement plane as in Figure 4.2. Similiarly, transfer functions can be computed for a linear model of the monotube.

$$\frac{\Delta P(s)}{Q_S} = \frac{R\frac{C'}{C''}}{RC's + 1} \tag{4.17}$$

$$\frac{\Delta P(s)}{\frac{Q_S}{s}} = \frac{R\frac{C'}{C''}s}{RC's + 1} \tag{4.18}$$

$$\frac{1}{C'} = \frac{1}{C_1 + C_g} + \frac{1}{C_2} \tag{4.19}$$

$$\frac{1}{C''} = \frac{\frac{A_1}{A_2}}{C_1 + C_g} + \frac{1}{C_2} \tag{4.20}$$

Notice when comparing the effective RC time constants of the two different types of shock absorbers (RC_{eff} for the dualtube vs. RC' for the monotube), the monotube linear model predicts more phase loss at a given frequency because a monotube would have a larger time constant due to the additional compliance of the gas all other considerations being equal. This would translate to additional hysteresis in the force-velocity plane at a given frequency.

The question of whether nonlinearities effect the dynamic behavior can be investigated by substituting nonlinear constitutive relationships for the elements. A nonlinear simplified model of the compliance is made based on the constitutive law of Eqn. (4.7) for the elastic-plastic model. In this law, when the pressure on one side of the piston drops to zero, the compliance becomes infinite as in the case in the cavitation model for the full shock absorber model. As a result, a 2-state model is required for both the monotube and dualtube simple models. The resistor constitutive equation will be the quadratic model of Eqn. (4.3) in conductive causal form representative of the orifice equation for a constant discharge coefficient.

$$Q_R = sign(\Delta P)\left(\frac{\Delta P}{R}\right)^{\frac{1}{2}} \tag{4.21}$$

Both the linear and nonlinear model behavior are shown for three test cases to qualitatively demonstrate the behavior at different frequencies. Unity resistance and compliance values are used for all models with the exceptions of the nonlinear models of the compliances on either side of the piston when the pressure approaches zero and the gas compliance of the monotube which is set to 100 because the compressibility of nitrogen gas is between two and three orders of magnitude larger than oil. The area ratio for the monotube model is set to 2. Both models start from rest. The monotube state initial pressures (i.e. efforts) are unity while those for the dualtube are $\frac{1}{20}$ representing the initial gas pressurization order of magnitude. The input

sinusoidal flow is held at a peak value of unity for each test case.

Figures 4.7 are 4.8 the responses for two oscillations at a frequency one order of magnitude lower than the case defined by the RC time constant for the dualtube linear simplified model. (The time constant defines the break frequency $\frac{1}{RC_{eff}}$.) The output effort is the pressure difference across the piston determined by the capacitor states. The linear model effort is the pressure difference across the piston for both the dualtube and monotube models. In the dualtube model, this is the total (or net) force. In the monotube model, the pressure difference is proportional to the "damping" force or $A_r(P_r - P_h)$ force plotted in Sect. 3.2 because of the unequal piston areas. The net effort for the monotube model considers the unequal piston areas. The component of effort related to the headside pressure acting on the equivalent rod area is referred to as the "gas" component in the monotube model.

At this low frequency, the output of the system appears to be more closely the characteristic of a resistor (compare to Figure 4.1). The efforts in both models slightly lag the input flow because of the "memory" added to the system by the capacitors allowing the pressure difference to continue to build even after the input flow has reversed direction. The indications of hysteresis loops occurring in the effort-flow plane result from the lagging pressure differential with respect to the input flow. The quadratic resistor constitutive relationship in combination with the lagged pressure response due to the state produces the figure-8 hysteresis loops in both the dualtube and monotube nonlinear model effort-flow curves.

Note that the rodside pressure drops to zero initially on the dualtube nonlinear model. The cavitation model in this case prevents the pressure difference from rising as rapidly and, in combination with the quadratic resistor law, flattens the effort-flow curve around zero flow. The combined system will, like the resistor model, dissipate energy when in the first and third quadrants of the effort-flow plane. The

gas volume of the simple monotube model produces a similar type of hysteresis near zero flow as resulted in the higher-order model of this study. Note the similarity between the nonlinear simple monotube model results (Figure 4.8) and the higher order model results without a check valve (Figures 3.28 and 3.29). This indicates the hysteresis in the higher order model near zero velocity is in part due to the gas volume compression and the hysteresis at higher velocities is attributable to the interaction of the compliance of the system with the quadratic resistance of the bleed orifices. (The combination of *RC* elements to produce general hysteresis models with finite states is discussed by Karnopp [10].)

Figures 4.9 are 4.10 are the responses for two oscillations at a frequency equal to that defined by the break frequency for the simple dualtube linear model for the same initial conditions as the prior test case. The output of the system has hysteresis in both the effort-displacement and effort-flow planes. Additional phase loss at this higher frequency produces more hysteresis in the effort-flow plane for all flows for all models. Because input flow was held constant relative to the prior lower frequency case, the input displacement is smaller which reduces the impact of hysteresis near zero velocity for the simple monotube model. The more rapid flow (i.e. velocity) input rise produces a larger pressure difference which cavitates the fluid on either side of the dualtube piston reducing the potential pressure difference across the piston in the nonlinear model. Because all of these systems dissipate energy, all will eventually orbit the origins of the effort-displacement and effort-flow planes.

The final test case is for a frequency one order of magnitude higher than the break frequency of the linear dualtube model (see Figures 4.11 and 4.12). The response at this frequency appears more like that of a capacitor (compare to Figure 4.2) although the amplitude of the input displacement appears small compared to the input flow at this frequency. This effect would be more significant if the the input flow were

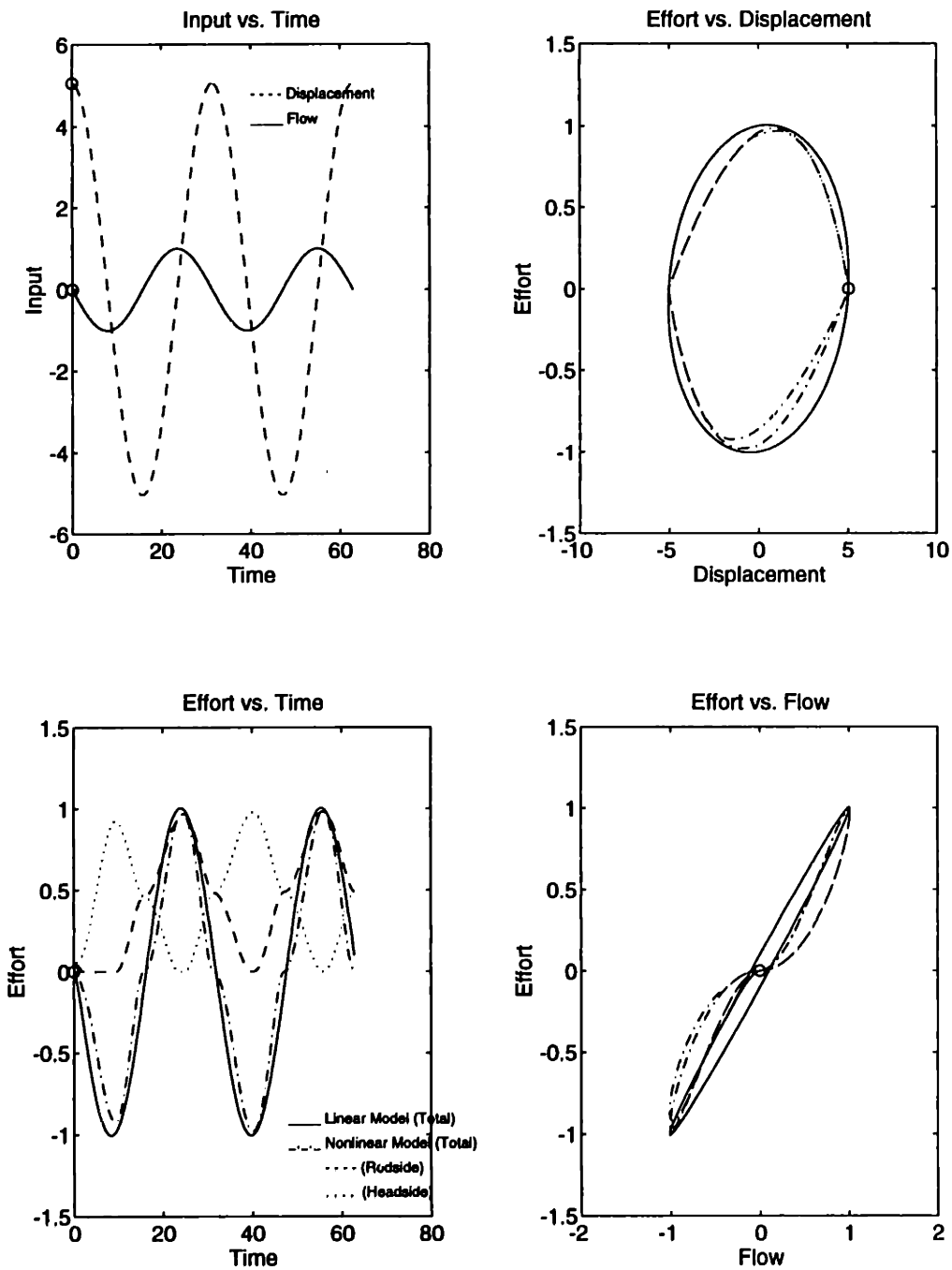

Figure 4.7: Simplified shock absorber model (dualtube) at $\frac{\frac{1}{10}}{RC_{eff}}$ frequency units

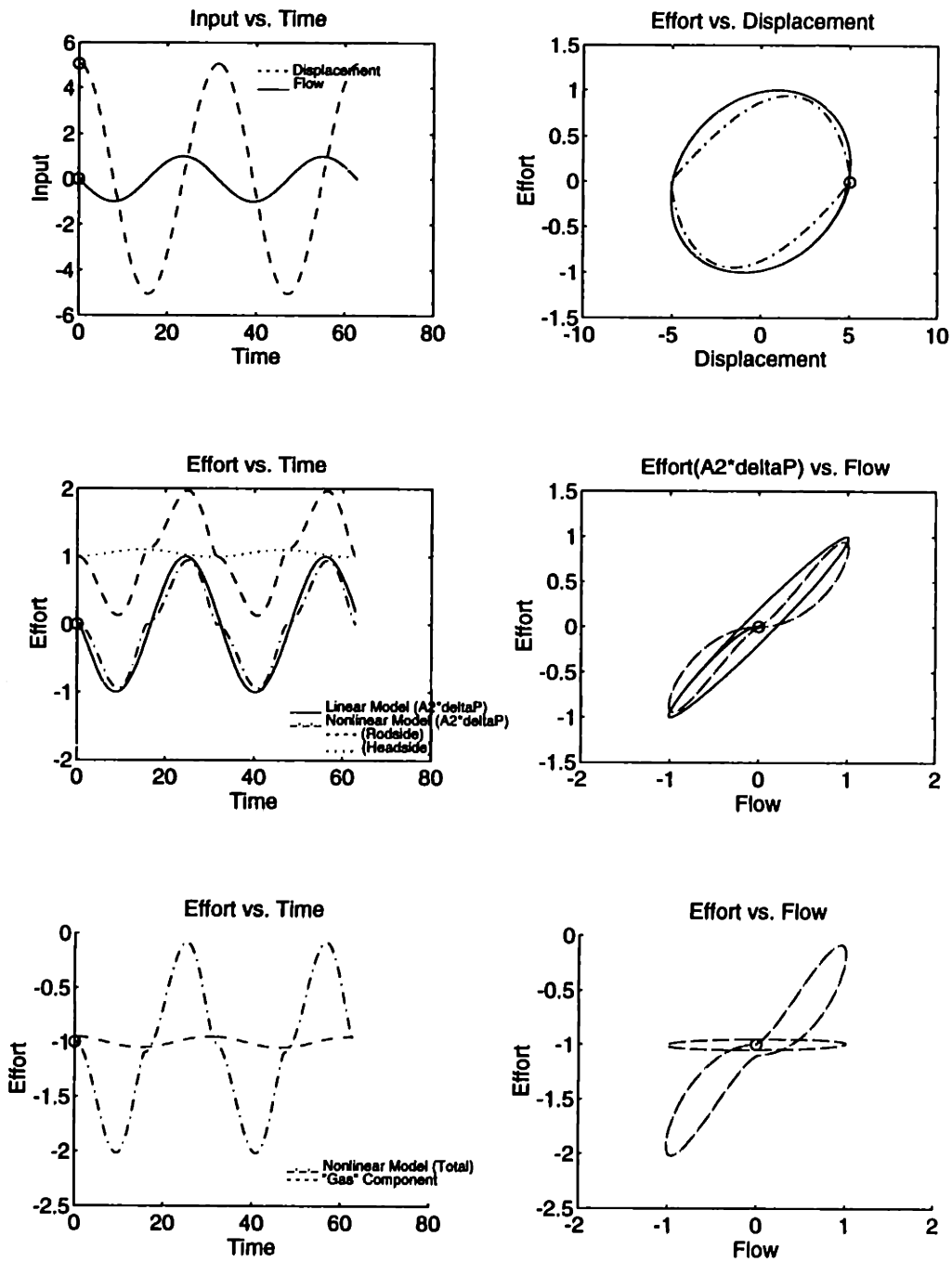

Figure 4.8: Simplified shock absorber model (monotube) at $\frac{\frac{1}{10}}{RC_{eff}}$ frequency units of dualtube

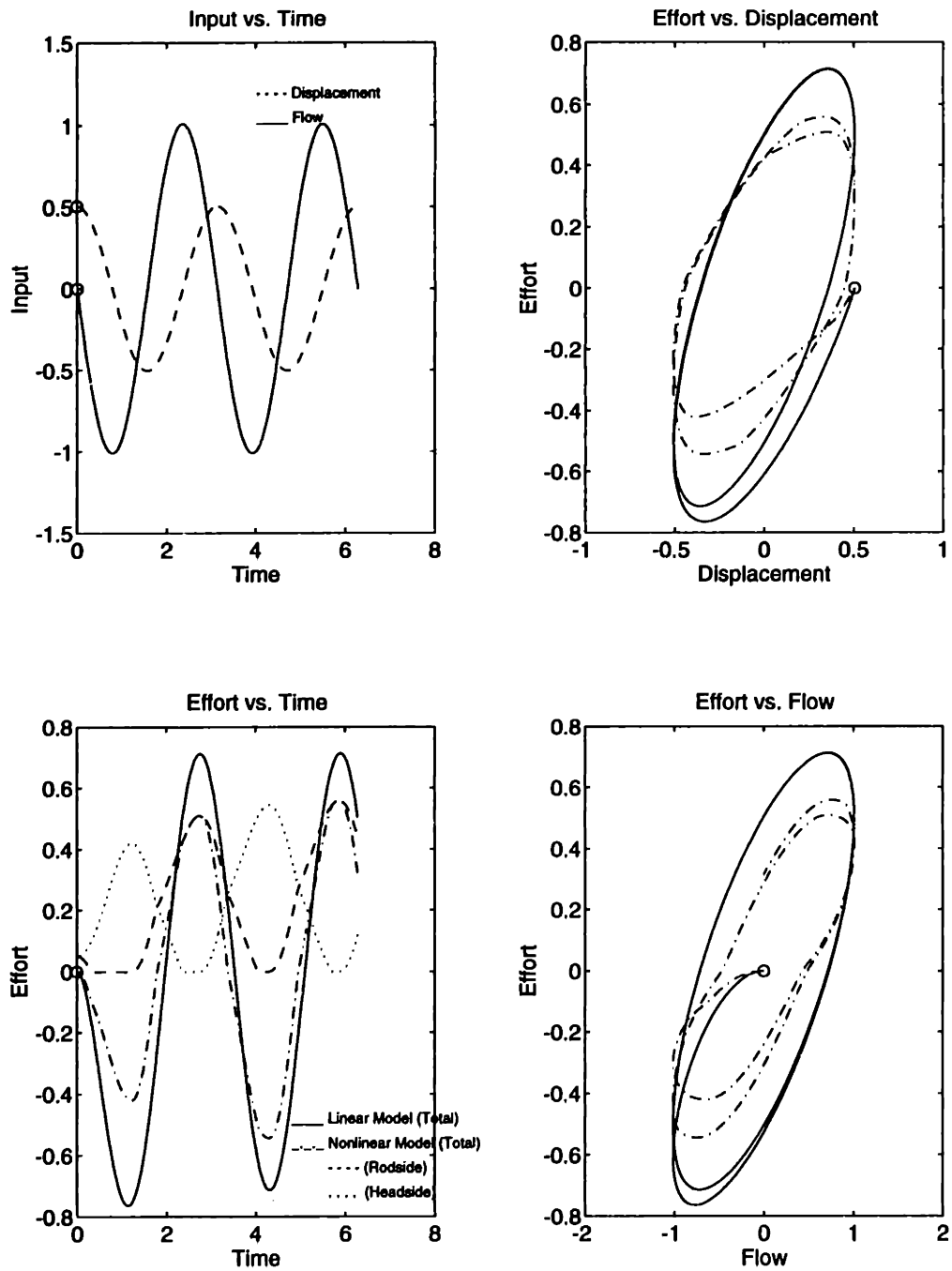

Figure 4.9: Simplified shock absorber model (dualtube) at $\frac{1}{RC_{eff}}$ frequency units

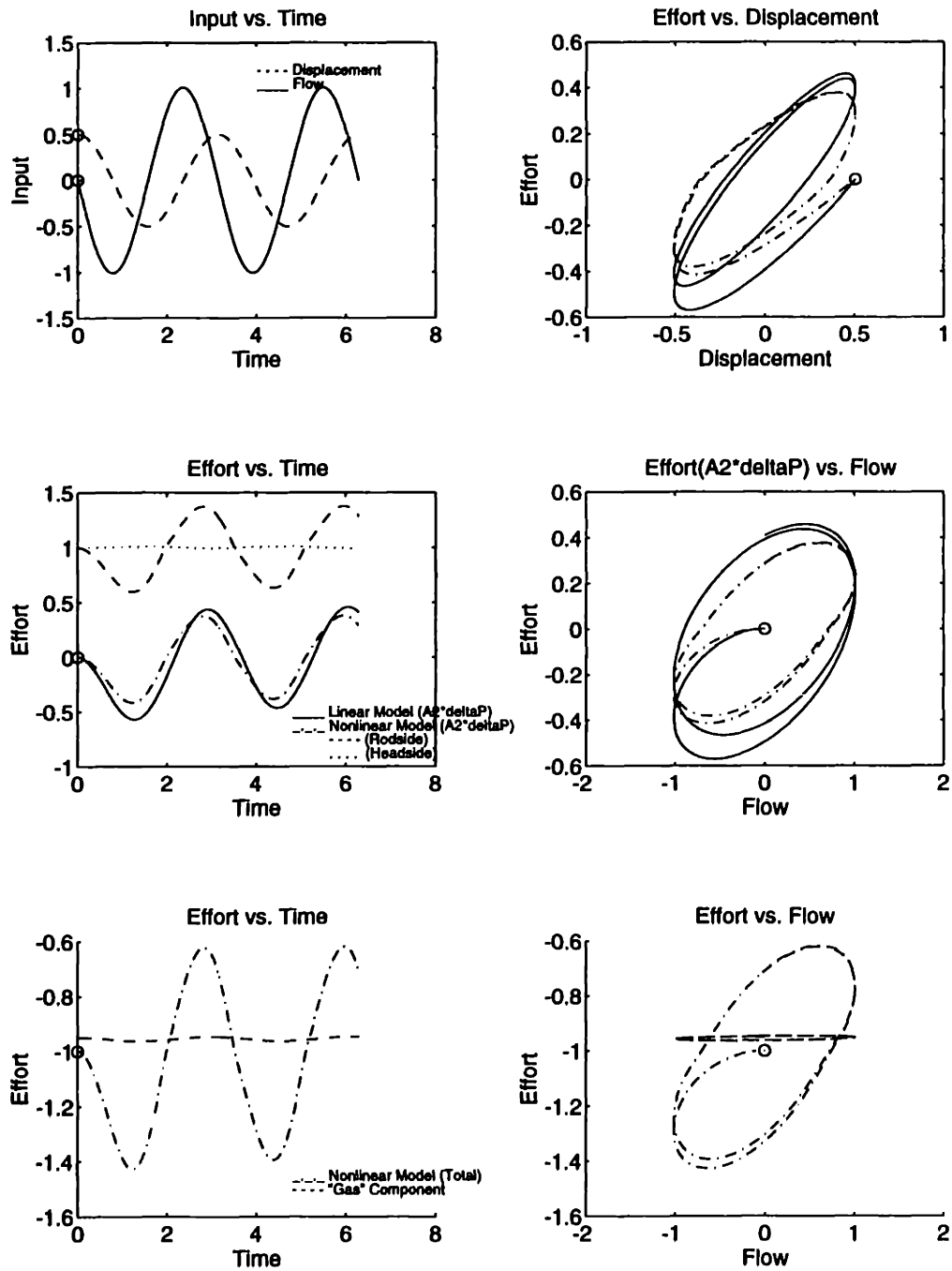

Figure 4.10: Simplified shock absorber model (monotube) at $\frac{1}{RC_{eff}}$ frequency units of dualtube

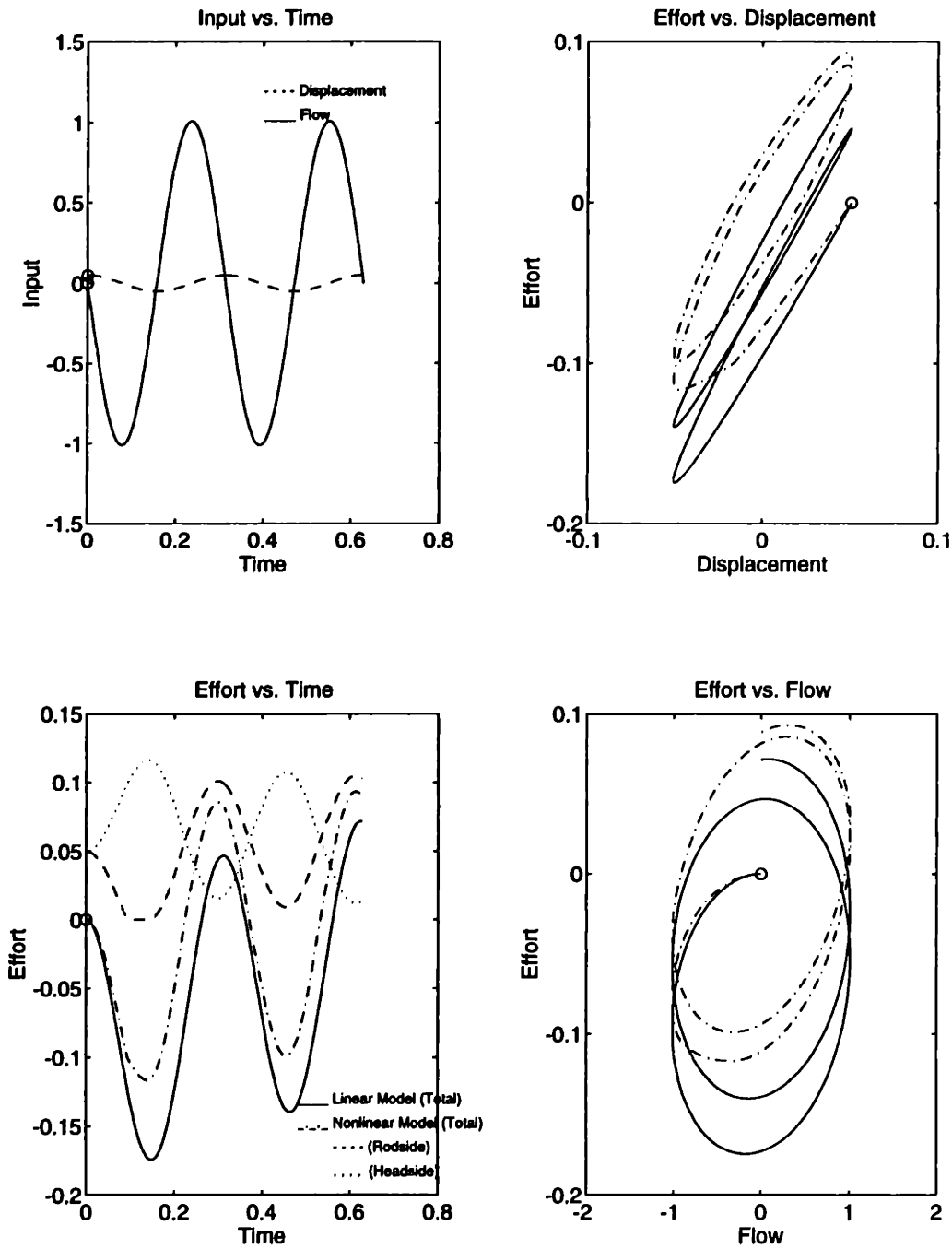

Figure 4.11: Simplified shock absorber model (dualtube) at $\frac{10}{RC_{eff}}$ frequency units

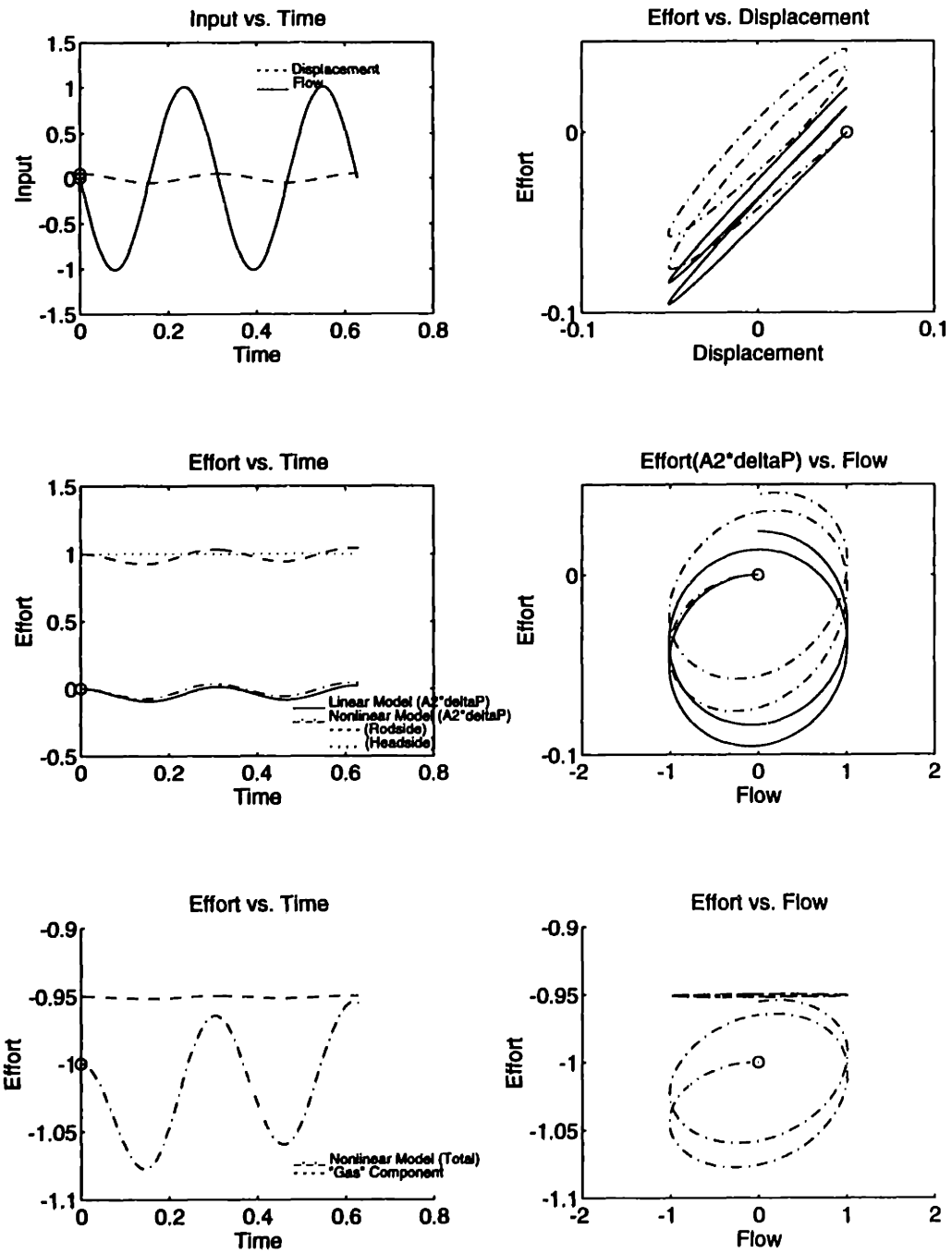

Figure 4.12: Simplified shock absorber model (monotube) at $\frac{10}{RC_{eff}}$ frequency units of dualtube

not held constant as the frequency is increased. The transient in the linear model requires more cycles than are plotted to die out. On the other hand, the nonlinear model settles in fewer cycles due mostly to the nonlinear compliance model which in combination with the resistive element results in a large amount of energy dissipation on the first cycle.

Both linear and nonlinear models exhibit the basic tendency of behaving more like resistors (or dampers) at low frequencies and capacitors (or springs) at high frequencies due to the additional phase loss between the input flow and output effort. The hysteresis increases in the effort-flow plane and decreases in the effort-displacement plane with increasing frequency. The simple model does not require inertia effects to create this frequency dependency. The state equations used to calculate the pressure of the fluid on either side of the piston are inherently "spring" equations. So the compliance effects of the shock absorber behavior cannot be alluded.

4.3 Conclusions of Past Researchers

The conclusions of Segal and Lang [22] and Karadayi and Masada [8] with respect to the general reason for hysteresis in the force-velocity plane are consistent with the results of this thesis. These researchers concluded that fluid compressibility and the formation of a gas phase in the chambers on either side of the piston are the causes of force-velocity hysteresis.

Lang [15] varied the fluid compressibility in his dualtube model by factors of by changing the bulk modulus by factors of $\frac{1}{2}$ and 2 and found larger compressibility exaggerates the hysteresis. In this study, the the amount of entrained air was varied with similar results. The additional effect compressiblity has in a monotube is that the gas pressure results in hysteresis near zero velocity. But the fluid is much less

likely to cavitate and form the type of gas phase which produces part of the hysteresis in dualtube designs.

Karadayi and Masada [8] developed a nonlinear model for a shock absorber by using a describing function approach to derive the force-velocity damping characteristics of a shock absorber. The three fundamental elements of their model were (1) a damper to represent viscous and dry friction damping, (2) a spring to represent the fluid compressibility, and (3) a backlash element. The backlash in a shock absorber as Karadayi and Masada describe it was "due to mechanical backlash which can increase as the shock absorber ages and partly due to the changes of the gas vapor phase present in the shock absorber fluid." It is unclear what was meant by mechanical backlash. However, both the spring and backlash elements together represent nonlinear shock absorber compressibility.

In the context of the bond graph model approach of this study, the spring and backlash element of the Karadayi and Masada model represent nonlinear capacitor constitutive relationships. By estimating the parameters of their simplified model, Karadayi and Masada were able to match actual shock absorber test data with good accuracy (see also Ref. [20] for another parametric model approach). Based on their describing function model approach, Karadayi and Masada concluded the hysteresis was due to fluid compressibility and "backlash" which was due, in part, to a gas phase in the fluid. They described their conclusions as consistent with those of Segal and Lang.

At high frequencies and large amplitudes Karadayi and Masada noted the compressibility effects were more significant. This is consistent with the idea of an increase in the importance of capacitive effects at high frequencies from a linear RC model standpoint. From a nonlinear model standpoint, higher velocities and amplitudes tend toward lower fluid compliances (i.e. larger effective stiffnesses) for the chamber

with higher pressure and are more likely to result in cavitation in the low pressure chamber. They also concluded at low frequencies and amplitudes the hysteresis was due mainly to "backlash". The effect could have been due to Coulomb friction between the piston and tube or high leakge flow around the piston consistent with the idea of dominant resistive effects at low frequencies. The later effect, however, was unlikely due to vaporous cavitation or nonlinear fluid compliance effects because at low velocities and amplitudes these effects are less significant. This result could also have been due to flexible shock mounts which may have been part of what they described as mechanical backlash resulting in a nonlinear constitutive relationship between displacement and force at low amplitudes similar to the spring with backlash model which appears as hysteresis on the effort-flow plane.

Lang attempted to correlate the hysteresis amount to the input frequency. He varied the input frequency while maintaining the same maximum velocity for each run. He found that the amount of hysteresis increased with increasing frequency and that the "increase is most pronounced in the portion of the loop caused by fluid compressibility." He speculated that the inertia of the valve parts could cause frequency dependency but found that these masses would have to be an order of magnitude larger to effect the results. In this thesis, the inertia of the fluid flow was considered and found to play an insignificant role in the hysteresis effects.

In this study, the frequency dependency was found to be a function of the compliance of the fluid and mechanical shock components. The reason the hysteresis increases with frequency while maintaining the same peak velocity is because the phase lag in the pressure difference across the shock is a function of frequency as observed in the simplified shock model. The dependency of hysteresis on frequency was not found to be a result of inertia effects.

The effect of frequency at constant maximum stroke velocity is to increase the

amount of hysteresis at higher frequencies in the areas of the force-velocity plane between zero and the maximum velocity. This results from the interaction of the orifice (resistive) nonlinear constitutive relationships and the effective fluid compliance (capacitive elements). The hysteresis near the region of zero velocity increases at lower frequencies because a monotube has the gas chamber which directly relates the output force to displacement. Also, the hysteresis near zero velocity increases with friction on the floating piston and the check valve preloads.

Chapter 5

Conclusions and Recommendations

5.1 Summary of Conclusions

Several conclusions can be drawn from the simulation results of this study of a monotube shock absorber. These conclusions are summarized below.

5.1.1 Frequency Dependency of Hysteresis

The interaction of resistive and capacitive elements in shock absorbers is responsible for the frequency dependency of hysteresis in the force-velocity characteristic of shock absorbers. The conclusions of Segal and Lang [22] and their higher order dualtube shock absorber model and Karadayi and Masada [8] and their use of describing function techniques to parametrically derive low order models of shock absorber models both support the conclusions of this thesis regarding hysteresis as simulated in monotube shock absorbers. The effects of fluid inertia are negligible.

5.1.2 Bubble/Cavitation Model

Monotubes are typically unsusceptible to cavitation due to the high gas pressurization which reduces the compression lag phenomenon more prevalent in dualtube designs an improves damping effectiveness. Air entrained as bubbles increases hysteresis due to the increase in the effective time constant of a shock absorber. As a result, additional phase loss occurs at the same input frequency. This phase loss manifests itself as hysteresis in the force-velocity characteristic of the shock absorber.

5.1.3 Floating Piston Stiction and Inertia

The inertia of the floating piston on shock absorber dynamics was negligible. The dominant effect of the floating piston was due to the friction acting on the piston which added to the amount of hysteresis near zero velocity. The stiction resulted in an increase in pressure build up near zero velocity.

5.1.4 Nitrogen Gas Pressurization

A monotube effectively has its own source of pressure in the form of the nitrogen gas volume. The nitrogen gas pressurization makes a monotube tolerant to fluid cavitation by design. As a result, hysteresis resulting from cavitation is far less likely in monotube designs as compared to dualtube designs.

5.1.5 Restriction Inertia and Variable Discharge Coefficients

The impact of fluid inertia on the dynamics of the shock absorber were negligible. The flow acceleration rates were typically small in the case of the port restriction or of short duration as for the bleed and blow-off orifices.

The effect of laminar flow through the use of variable discharge coefficients in the bleed and blow-off restrictions were also negligible for the frequency range of this study. Also, the check valve preload in the design of this study produced a build-up in pressure across the restrictions larger than the pressure drop across the bleed restriction required for transition for turbulent flow. The low transitional Reynolds number tended to result in laminar flow for very short durations even for low stroke velocities.

The variable discharge coefficient for the port flow was typically of significant duration during the cycle. However, the pressure drop across the port restrictions used in this study was negligible when compared to the preload due to the larger size

and the quantity of these restrictions.

5.1.6 Check Valve Model Effects

The check valve preloads were responsible for hysteresis near zero velocity in the force-velocity characteristic of the monotube shock absorber of this study. The absence of a fluid path across the piston resulted in a requirement for a minimum differential pressure drop across the piston before any significant flow occurred. This nonlinear compliance effect resulted in hysteresis when combined with the resistance effects of the damper.

5.2 Bond Graph Methodology

The bond graph technique was useful in order to observe the causal relationships between elements of the shock absorber and derive a consistent set of state equations. The method was also useful in identifying the major cause of the frequency dependent hysteresis loops as the interaction between capacitive and resistive elements of the shock absorber. This allows the analyst to understand the system from the principal state equations which characterize the system. In the case of a shock absorber, the state equations which most directly define the system are those of a generalized capacitor (i.e. spring) with dominant nonlinear resistive (i.e. damping) terms.

5.3 Implication of Simulation Results to Shock Absorber Modelling

The simulation results indicate that the major sources of hysteresis in the force-velocity characteristic of a monotube shock absorber are the interaction of nonlinear constitutive relationships derived from (1) the effective compliance of the fluid, tube, and entrained air, (2) the compliance of the nitrogen gas volume, (3) the resistive

fluid damping through the piston orifices, (4) the resistive friction acting on the floating piston, and (5) the compliance due to the check valve preloads. The frequency dependency of the hysteresis is produced by the same interaction which at higher frequencies results in added phase loss due to the capacitive elements. The resistive elements which are responsible for energy dissipation produce hysteresis in the force-displacement characteristic and become less effective as damping elements at higher frequencies for the same maximum velocity.

Not surprisingly, these elements are inherent to the system which behaves more like a generalized capacitior (or spring) at higher frequencies and larger displacements. For example, the floating piston friction force which seals the boundary between the gas and the fluid produces hysteresis near zero velocity. Also, the check valves in the design studied in this thesis produce hysteresis which would be mitigated to some extent in designs with bleed orifice paths without check valves.

5.4 Recommendations

The model developed in this thesis should be correlated to additional dynamic monotube test data in order to assess the model's acceptability as a design tool. Simplification of the model may be possible with acceptable concessions to model accuracy. For example, the laminar flow calculations for the bleed and blow-off restrictions may be unnecessary for a wide range of model classes and various states may be deleted such as those associated with the port flow. The model may then have sufficiently few states that it could be made part of automotive suspension system models. A shock absorber must ultimately be intergrated with the automobile suspension system. The designer needs to understand the subsystem dynamics in order to produce systems with desirable characteristics when the elements are assembled.

Appendix A

Compliance of a Pressurized Cylinder

The diametral and axial deflection for an internally pressurized cylinder with capped ends from Roark [29] are

(1) Inside Diametral Deflection

$$\Delta D_i = \frac{\Delta P D_i}{E}\left[\frac{(1+\nu)D_o^2 + (1-2\nu)D_i^2}{D_o^2 - D_i^2}\right] \tag{A.1}$$

(2) Length Deflection

$$\Delta L = \frac{\Delta P L}{E}\left[\frac{(1-2\nu)D_i^2}{D_o^2 - D_i^2}\right] \tag{A.2}$$

The relative deflection is

$$\frac{\Delta D_i}{\Delta L} = \frac{\Delta D_i}{L}\left[\frac{1+\nu}{1-2\nu}\left(\frac{D_o}{D_i}\right)^2 + 1\right] \tag{A.3}$$

For a typical shock absorber,

$$\begin{aligned} \frac{D_i}{L} &= \frac{1.5}{10} \\ \frac{D_o}{D_i} &= \frac{10}{9} \\ \nu &= 0.3 \end{aligned}$$

then,

$$\frac{\Delta D_i}{\Delta L} \simeq \frac{1}{3}$$

But what is the relative effect on the volume change of the container?

$$V_c = \frac{\pi}{4} D_i^2 L \tag{A.4}$$

Differentiating results in

$$\Delta V_c = \frac{\pi}{4} D_i \left(2L\Delta D_i + D_i \Delta L\right) \tag{A.5}$$

Hence, the ratio of volume change due to the diameter change versus the length change is

$$\frac{\Delta V_{dia}}{\Delta V_L} = \frac{2\frac{\Delta D_i}{\Delta L}}{\frac{D_i}{L}} \tag{A.6}$$

Assuming the relationships above, the effect due to the diameter increase is approximately $4 - 5$ times that of the axial increase.

$$\frac{\Delta V_{dia}}{\Delta V_L} = 4.4$$

Appendix B

Compliance Comparisons

A comparison of the potential complicances can be made to help decide those most significant to te problem. Because the compliances are from the fluid and mechanical domains, the mechanical compliances are reflected into the fluid domain for comparison purposes.

(i) Fluid in the Y-Junction:

The fluid compliance for the volume between the port channel and the bleed and blow-off restrictions is calculated assuming a realistic volume size.

$$\begin{aligned} V_y &= \pi t(r_o^2 - r_i^2) = 9.4 \times 10^{-7} m^3 \\ C_y &= \frac{V_y}{\beta_l} = \frac{9.4 \times 10^{-7}}{1.52 \times 10^9} = 6.2 \times 10^{-16} \frac{m^5}{N} \end{aligned}$$

(ii) Blow-off Valve Assembly :

The mechanical compliance for the disk valve and coil spring assembly as reflected into the fluid domain across the area of the disk valve is

For an open valve:

$$\begin{aligned} C_{bo} &= \frac{1}{\frac{1}{C_{cs}} + \frac{1}{C_{oo}}} = 9.83 \times 10^{-8} \frac{m}{N} \\ C_{bofluid} &= C_{bo} A_d^2 = 9.83 \times 10^{-8} (3.23 \times 10^{-4})^2 = 1.02 \times 10^{-14} \frac{m^5}{N} \end{aligned}$$

For a closed valve:

$$\begin{aligned} C_{bo} &= \frac{1}{\frac{1}{C_{cs}} + \frac{C_{aa}}{C_{aa}C_{oo} - C_{ao}C_{oa}}} = 1.94 \times 10^{-8} \frac{m^5}{N} \\ C_{bofluid} &= C_{bo} A_d^2 = 2.02 \times 10^{-15} \frac{m^5}{N} \end{aligned}$$

(iii) Fluid in Cylinder :

The fluid compliances for the volumes on either side of the piston assuming realistic shock volumes are

$$\begin{aligned} V_r &= 3.24 \times 10^{-4} m^3 \\ C_r &= 2.13 \times 10^{-13} \frac{m^5}{N} \\ V_h &= 3.88 \times 10^{-4} m^3 \\ C_h &= 2.55 \times 10^{-13} \frac{m^5}{N} \end{aligned}$$

(iv) Shock Tube Cylinder:

The effective fluidic compliances for the shock tube (cylinder) are

$$\begin{aligned} \beta_c &= \frac{E}{2}\left[\frac{D_o^2 - D_i^2}{(1+\nu)D_o^2 + (1-2\nu)D_i^2}\right] = 13.3 \times 10^9 Pa \\ C_{cr} &= 2.44 \times 10^{-14} \frac{m^5}{N} \\ C_{ch} &= 2.92 \times 10^{-14} \frac{m^5}{N} \end{aligned}$$

Appendix C

Compliance Model of a Disk Valve

The disk valve compliance is derived from the stiffness of an annular plate as given in Roark [29]. The boundary conditions are a fixed inner edge and free outer edge.

The general constants for this problem are

$$D = \frac{Et^3}{12(1-\nu^2)} \tag{C.1}$$

$$C_8 = \frac{1}{2}\left[1+\nu+(1-\nu)\left(\frac{b}{a}\right)^2\right] \tag{C.2}$$

$$C_9 = \frac{b}{a}\left[\frac{1+\nu}{2}\ln\frac{a}{b}+\frac{1-\nu}{4}\left(1-\left(\frac{b}{a}\right)^2\right)\right] \tag{C.3}$$

$$F_2 = \frac{1}{4}\left[1-\left(\frac{b}{r}\right)^2\left(1+2\ln\frac{r}{b}\right)\right] \tag{C.4}$$

$$F_3 = \frac{b}{4r}\left[\left(1+\left(\frac{b}{r}\right)^2\right)\ln\frac{r}{b}+\left(\frac{b}{r}\right)^2-1\right] \tag{C.5}$$

$$G_3 = \frac{r_j}{4r}\left[\left(1+\left(\frac{r_j}{r}\right)^2\right)\ln\frac{r}{r_j}+\left(\frac{r_j}{r}\right)^2-1\right] < r-r_j >^0 \tag{C.6}$$

The constants resulting from the boundary conditions are

$$L_9 = \frac{r_j}{a}\left[\ln\frac{r}{b}\left(\frac{1+\nu}{2}\right)\right] \tag{C.7}$$

$$Q_{rb} = \frac{wr_j}{b} \tag{C.8}$$

$$M_{rb} = -\frac{wa}{C_8}\left(\frac{r_jC_9}{b}-L_9\right) \tag{C.9}$$

The general elastic deformation equation at radius, r, is

$$y_i = -M_{rb}F_2\frac{r^2}{D}-Q_{rb}F_3\frac{r^3}{D}+w_jG_3\frac{r^3}{D} \tag{C.10}$$

The load w is load per unit of circumferential length. The compliance in terms of displacement per unit force per unit of circumferential length is then

$$C_{ij} = \frac{y_i}{w_j} = \frac{1}{w_j}\frac{r_i}{D}\left[-\frac{M_{rb}}{F_2} - Q_{rb}r_iF_3 + G_3r_iw_j\right] \tag{C.11}$$

Substitution of the above constants results in the following expression for compliance and converting this into units of displacement per unit load where the subscripts denote the compliance at i for a load applied at j.

$$C_{ij} = \frac{r_i^2}{2\pi r_j D}\left[\frac{a}{C_8}\left(\frac{r_jC_9}{b} - L_9\right)F_2 + r_iG_3 - \frac{r_j}{b}r_iF_3\right] \tag{C.12}$$

This is the compliance for a single disk valve. Multiple disk valves (stacks) are springs in parallel. Hence, the stiffnesses are additive. For a stack of N disks with the same dimensions and made of the same material, the equivalent compliance is

$$C_{ij}^{eff} = \frac{C_{ij}}{N} \tag{C.13}$$

Bibliography

[1] Bender, E., "Druckverlust bei Laminarer Stromung im Rohreinlauf," *Chemie-Ingenieur-Technik*, Vol. 11, 1969, pp. 682-686.

[2] Blackburn, J.F., Reethof, G., and Shearer J.L., *Fluid Power Control*, Technology Press of M.I.T. and John Wiley and Sons, New York, NY 1960.

[3] Blevins, R.D., *Applied Fluid Dynamics Handbook*, Van Nostrand Reinhold, New York, NY 1984.

[4] Bowden, F.P., and Tabor, D., *The Friction and Lubrication of Solids*, Clarendon Press, Oxford, England 1950.

[5] Chen, R.Y., "Flow in the Entrance Region at Low Reynolds Numbers," *Journal of Fluids Engineering*, Vol. 95, Mar. 1973, pp. 153-158.

[6] Dransfield, P., *Hydraulic Systems - Design and Analysis of Their Dynamics*, Springer-Verlag, New York, 1981.

[7] Fox, R.W. and McDonald, A.T, *Introduction to Fluid Mechanics*, John Wiley and Sons, Berlin, 1978.

[8] Karadayi, R. and Masada, G.Y., "A Nonlinear Shock Absorber Model," *Proceedings of Symposium on Simulation and Control of Ground Vehicles and Transportation Systems*, Anahiem, CA 1986, pp. 149-165.

[9] Karnopp, D.C., "Bond Graph Models for Fluid Dynamic Systems," *Journal of Dynamic Systems, Mearsurement, and Control*, Vol. 94, No. 3, 1972, pp. 222-229.

[10] Karnopp, D.C., "Computer Models of Hysteresis in Mechanical and Magnetic Components," *Journal of the Franklin Institute*, Vol. 316, No. 5, 1983, pp. 405-415.

[11] Karnopp, D.C., Margolis, D.L., and Rosenberg, R.C., *System Dynamics*, Wiley & Sons, New York, NY, 1990.

[12] Kays, W.M., "Loss Coefficients for Abrupt Changes in Flow Cross Section with Low Reynolds Number Flow in Single and Multiple-Tube Systems," *Transactions of the ASME 72*, Nov. 1950, pp. 1067-1074.

[13] Kragelsky, I.V., Dobychin, M.N., and Kombalov, V.S., *Friction and Wear Calculation Methods*, Pergamon Press, Oxford, 1982.

[14] Lamb, W.S., *Cavitation and Aeration in Hydraulic Systems*, BHRA The Fluid Engineering Centre, Bedford, England, 1987.

[15] Lang, H.H., "A Study of the Characteristics of Automotive Hydraulic Dampers at High Stroking Frequencies," Ph.D. Dissertation, The University of Michigan, 1977.

[16] Leroy, W.W. and Leslie, R.L., "Hydraulic Fluid Properties and System Performance," 18th National Conference on Industrial Hydraulics, Vol. 16, 1962.

[17] Merritt, H.E., *Hydraulic Control Systems*, Wiley & Sons, New York, NY, 1967.

[18] Nusselt, W., "The Pressure in the Annulus of Pipes with Sudden Increase in Cross Section for High Velocity Air Flow," *Forschung auf dem Gebietes des Ingenieurwesens*, Vol. 11, No. 5, September-October, 1940, pp. 250-255.

[19] Plesset, M.S., Prosperetti, A., "Bubble Dynamics and Cavitation," *Annual Review of Fluid Mechanics*, Vol. 9, 1977, pp. 145-185.

[20] Reybrouck, K., "A Nonlinear Parameteric Model of an Automotive Shock Absorber," *Vehicle Suspension System Advancements*, SAE paper 940869, 1994, pp. 79-86.

[21] Rouse, H. and Howe, J.W., *Basic Mechanics of Fluids*, Wiley & Sons, New York, NY, 1953.

[22] Segal, L. and Lang, H.H., "The Mechanics of Automotive Hydraulic Dampers at High Stroking Frequencies," *Vehicle System Dynamics*, No. 10, 1981, pp. 79-83.

[23] Shah, R.K., "A Correlation for Laminar Hydrodynamic Entry Length Solutions for Circular and Noncircular Ducts," *Journal of Fluids Engineering*, Vol. 100, June 1978, pp. 177-179.

[24] Shapiro, A.H., Siegel, R., and Kline, S.J., "Friction Factor in the Laminar Entry Region of a Smooth Tube," *Proceedings of the Second U.S. National Congress of Applied Mechanics*, 1954, pp. 733-741.

[25] Shapiro, A.H., and Smith, R.D., "Friction Coefficients in the Inlet Length of Smooth Round Tubes," *NACA T.N. No. 1785*, Nov. 1948.

[26] Streeter, V.L., and Wylie, B.E., *Fluid Mechanics*, McGraw-Hill, New York, NY, 1985.

[27] Trevena, D.H., *Cavitation and Tension in Liquids*, Adam Hilger, Bristol, England, 1987.

[28] Weast, R.C., and Astle, M.J., *CRC Handbook of Chemistry and Physics*, 62nd Edition, CRC Press, Boca Raton, FL, 1982.

[29] Young, W.C., *Roark's Formulas for Stress and Strain*, McGraw-Hill, New York, NY, 1989.

[30] Yu Jinghong, Chen Zhaoneng, and Lu Yuanzhang, "The Variation of Oil Effective Bulk Modulus with Pressure in Hydraulic Systems," *Journal of Dynamic Systems, Measurement, and Control*, Vol. 116, Mar. 1994, pp. 146-150.